

# Detailed SZ study with AMI of 19 LoCuSS galaxy clusters: masses and temperatures out to the virial radius <sup>★</sup>

AMI Consortium: Carmen Rodríguez-Gonzálvez<sup>1,2</sup>, Timothy W. Shimwell<sup>1,5</sup>, Matthew L. Davies<sup>1</sup>, Farhan Feroz<sup>1</sup>, Thomas M. O. Franzen<sup>1,3</sup>, Keith J. B. Grainge<sup>1,4</sup>, Michael P. Hobson<sup>1</sup>, Natasha Hurley-Walker<sup>1,5</sup>, Anthony N. Lasenby<sup>1,4</sup>, Malak Olamaie<sup>1</sup>, Guy Pooley<sup>1</sup>, Richard D. E. Saunders<sup>1,4</sup>, Anna M. M. Scaife<sup>7</sup>, Michel P. Schammel<sup>1</sup>, Paul F. Scott<sup>1</sup>, David J. Titterton<sup>1</sup>, Elizabeth M. Waldram<sup>1</sup>

<sup>1</sup> *Astrophysics Group, Cavendish Laboratory, JJ Thomson Avenue, Cambridge CB3 0HE*

<sup>2</sup> *Spitzer Science Center, MS 220-6, California Institute of Technology, Pasadena, CA 91125, USA*

<sup>3</sup> *CSIRO Astronomy & Space Science, Australia Telescope National Facility, PO Box 76, Epping, NSW 1710, Australia*

<sup>4</sup> *Kavli Institute for Cosmology Cambridge, Madingley Road, Cambridge, CB3 0HA*

<sup>5</sup> *International Centre for Radio Astronomy Research, Curtin Institute of Radio Astronomy, 1 Turner Avenue, Technology Park, Bentley, WA 6845, Australia*

<sup>7</sup> *School of Physics & Astronomy, University of Southampton, Highfield, Southampton, SO17 1BJ*

Accepted —; received —; in original form 18 July 2018

## ABSTRACT

We present detailed 16-GHz interferometric observations using the Arcminute Microkelvin Imager (AMI) of 19 clusters with  $L_X > 7 \times 10^{37}$  W ( $h_{50} = 1$ ) selected from the Local Cluster Substructure Survey (LoCuSS;  $0.142 \leq z \leq 0.295$ ) and of Abell 1758b, which is in the field of view of Abell 1758a. We detect and resolve Sunyaev-Zel’dovich (SZ) signals towards 17 clusters, with peak surface brightnesses between 5 and  $23\sigma$ . We use a fast, Bayesian cluster analysis to obtain cluster parameter estimates in the presence of radio point sources, receiver noise and primordial CMB anisotropy. We fit isothermal  $\beta$ -models to our data and assume the clusters are virialized (with all the kinetic energy in gas internal energy). Our gas temperature,  $T_{\text{AMI}}$ , is derived from AMI SZ data and *not* from X-ray spectroscopy. Cluster parameters internal to  $r_{500}$  are derived under the assumption of hydrostatic equilibrium. We find the following. (i) Different gNFW parameterizations yield significantly different parameter degeneracies. (ii) For  $h_{70} = 1$ , we find the classical virial radius,  $r_{200}$ , to be typically  $1.6 \pm 0.1$  Mpc and the total mass  $M_{\text{T}}(r_{200})$  typically to be  $2.0\text{--}2.5 \times M_{\text{T}}(r_{500})$ . (iii) Where we have found  $M_{\text{T}}(r_{500})$  and  $M_{\text{T}}(r_{200})$  X-ray and weak-lensing values in the literature, there is good agreement between weak-lensing and AMI estimates (with  $M_{\text{T,AMI}}/M_{\text{T,WL}} = 1.2_{-0.3}^{+0.2}$  and  $= 1.0 \pm 0.1$  for  $r_{500}$  and  $r_{200}$ , respectively). In comparison, most SUZAKU/CHANDRA estimates are *higher* than for AMI (with  $M_{\text{T,X}}/M_{\text{T,AMI}} = 1.7 \pm 0.2$  within  $r_{500}$ ), particularly for the stronger mergers. (iv) Comparison of  $T_{\text{AMI}}$  to  $T_{\text{X}}$  sheds light on high X-ray masses: even at large radius,  $T_{\text{X}}$  can substantially exceed  $T_{\text{AMI}}$  in mergers. The use of these higher  $T_{\text{X}}$  values will give higher X-ray masses. We stress that large-radius  $T_{\text{AMI}}$  and  $T_{\text{X}}$  data are scarce and must be increased. (v) Despite the paucity of data, there is an indication of a relation between merger activity and SZ ellipticity. (vi) At small radius (but away from any cooling flow) the SZ signal (and  $T_{\text{AMI}}$ ) is less sensitive to ICM disturbance than the X-ray signal (and  $T_{\text{X}}$ ) and, even at high radius, mergers affect  $n^2$ -weighted X-ray data more than  $n$ -weighted SZ, implying that significant shocking or clumping or both occur in even the outer parts of mergers.

**Key words:** cosmology: observations – cosmic microwave background – galaxies: clusters – Sunyaev–Zel’dovich X-ray – galaxies: clusters: individual (Abell 586, Abell 611, Abell 621, Abell 773, Abell 781, Abell 990, Abell 1413, Abell 1423, Abell 1704, Abell 1758a, Abell 1758b, Abell 2009, Abell 2111, Abell 2146, Abell 2218, Abell 2409, RXJ0142+2131, RXJ1720.1+2638, Zw0857.9+2107, Zw1454.8+2233)

arXiv:1205.7067v1 [astro-ph.CO] 31 May 2012

## 1 INTRODUCTION

The virtues of galaxy clusters are often extolled as, for example, being the largest gravitationally bound systems in the Universe, or being excellent samplers of the matter field on large scales, or simply as being of fundamental importance to astrophysics and cosmology (see e.g., White et al. 1993, Eke, Cole, & Frenk 1996 and Joy et al. 2001). To make full use of these virtues one needs observations that, amongst others things, reach large distances away from cluster centres. It would often be very useful to reach the classical virial radius  $\approx r_{200}$  of a cluster, internal to which the average density is 200 times the closure density. Studying clusters on these scales is important for many reasons. First, these measurements are needed to characterize the entire cluster volume. Second, they can be key for any attempt at precision cosmology, including calibrating scaling relations (Kaiser 1986), as they are believed to be less susceptible to the complicated physics of the core region from e.g., star formation, energy feedback from active galactic nuclei and gas cooling. Third, the virial radius marks the transition between the accreting matter and the gravitationally-bound, virialized gas of clusters and thus contains information on the current processes responsible for large-scale structure formation. However, there are few such observations due to the difficulties of obtaining a signal far away from the cluster centre. We now comment on four methods of estimating cluster masses (see Allen, Evrard, & Mantz 2011 for a recent, overall review):

- Spectroscopic measurements of the velocity dispersion of cluster members require very high sensitivity at moderate to high redshift, and confusion becomes worse as redshift increases and as distance on the sky from the cluster centre increases. Cluster masses have recently been obtained this way in e.g., Rines et al. (2010) and Sifon et al. (2012).

- X-ray observations of the Bremsstrahlung (free-free radiation) from the intracluster plasma (by convention referred to as ‘gas’) have delivered a great deal of information on cluster physics on a large number of clusters (see e.g., Ebeling et al. 1998, Bonamente et al. 2006 and Kotov & Vikhlinin 2005). Observations are, of course, difficult at high redshift due to cosmic dimming, and because the X-ray signal is  $\propto \int n^2 f(T) dl$ , where  $n$  is the electron density,  $T$  is electron temperature,  $f(T)$  is a weak function of  $T$ , and  $l$  is the line of sight through the cluster, there is significant bias to gas concentration, which makes reaching a high radius difficult – however, at low to intermediate redshift there is a small but growing number of observations that approach or reach  $r_{200}$  mainly with the SUZAKU satellite, though the sky background subtraction is challenging (e.g., George et al. 2009, Hoshino et al. 2010).

- Gravitational lensing of background galaxies gives the distribution of all the matter in the cluster directly, without relying on assumptions about the dynamical state of the cluster. Any mass concentrations along the line-of-sight not associated with the cluster will lead to an overestimate of the weak lensing cluster mass. But the ‘shear’ signal is proportional to the rate of change with radius of the gravitational potential, which changes increasingly slowly with radius at large radius, so reaching large radius is difficult. Confusion also bears strongly on this difficulty, and measurement is of course harder as redshift increases. Example weak-lensing cluster studies include Okabe & Umetsu (2008) and Corless, King, & Clowe (2009), for analyses of individual high-mass clusters, and Mandelbaum & Seljak (2007) and Rozo, Wu, & Schmidt (2011) for analyses of stacked lensing profiles for many low-mass clusters.

- The Sunyaev Zel’dovich (SZ; Sunyaev & Zel’dovich 1970;

see e.g. Birkinshaw 1999 and Carlstrom, Holder & Reese 2002 for reviews) signal from inverse Compton scattering of the CMB by the cluster gas has relatively little bias to gas concentration since it is  $\propto \int nT dl$ , and has remarkably little sensitivity to redshift over moderate to high redshift; both of these properties make the SZ effect extremely attractive. The problem with SZ is that it is intrinsically very faint. The first generation of SZ telescopes, including the OVRO 40-m (see e.g., Birkinshaw et al. 1984), the OVRO 5-m (see e.g., Herbig et al. 1995), the OVRO/BIMA arrays (e.g., Carlstrom et al. 1992) and the Ryle Telescope (see e.g., Grainge et al. 1993) had to integrate for a very long time to get a significant SZ detection of a single known cluster. The new generation, including ACT (see e.g., Hincks et al. 2010 and Marriage et al. 2011), AMI (see e.g., AMI Consortium: Zwart et al. 2008 and AMI Consortium: Shimwell et al. 2010), AMiBA (see e.g., Lo, Martin, & Chiueh 2001 and Wu et al. 2008), MUSTANG (see e.g., Korngut et al. 2011 and Mroczkowski et al. 2011), OCRA (see e.g., Browne et al. 2000 and Lancaster et al. 2011), Planck (see e.g. Tauber et al. 2010 and Planck Collaboration et al. 2011), SPT (see e.g Carlstrom et al. 2011 and Williamson et al. 2011) and SZA (see e.g., Carlstrom et al. 1992 and Muchovej et al. 2011) are all much more sensitive.

The new generation of SZ facilities include two types of instrument: ACT, Planck and SPT are instruments with wide fields of view (FoV) optimized for detecting CMB imprints in large sky areas in a short amount of time – this is a very important ability but, for the imaging of a particular cluster, a wide FoV is of no benefit; in contrast, AMI, AMiBA, MUSTANG, OCRA and SZA are designed to go deep and to measure the masses of the majority of clusters.

In AMI Consortium: Zwart et al. (2010), we reported initial SZ observations of seven X-ray clusters (selected to have low radio flux-densities to limit confusion) that approach or reach  $r_{200}$ . In this paper we report on resolved, interferometric SZ observations with arcminute resolution that approach or reach  $r_{200}$  in a substantial sample of X-ray clusters selected above an X-ray flux-density limit (plus a radio flux-density limit) and over a limited redshift-range (which limits the effects of cosmic evolution); as far as we are aware, this is the first time such SZ observations of a large cluster sample have been undertaken. These measurements are timely since complementary large- $r$  X-ray data have recently been obtained with SUZAKU (e.g., Bautz et al. 2009, Hoshino et al. 2010 and Kawaharada et al. 2010). These early SUZAKU measurements, despite the large model uncertainties, are already showing that ICM profiles on these scales appear to disagree with predictions from hydrodynamical cluster simulations (e.g., George et al. 2009) and have drawn attention to possible causes such as ICM clumping (Nagai & Lau 2011) and the breakdown of assumptions such as hydrostatic equilibrium (e.g., Evrard 1997), which can bias the X-ray masses (e.g., Rasia, Tormen, & Moscardini 2004, Meneghetti et al. 2010 and Fabjan et al. 2011). We stress that SZ observations, like those in the optical/IR and X-ray, also have their contaminants and systematics, and *all* four methods are also hampered by projection effects.

Studying large samples of clusters using multiple techniques is important for building a thorough understanding of cluster physics. Well-calibrated mass-observable relations are crucial for current and future cosmological studies – see e.g., Allen, Evrard, & Mantz (2011). To our knowledge, this is the largest cluster-by-cluster study for which masses have been derived from SZ targeted observations out to the virial radius. The results

from this work will be very valuable for detailed comparisons of cluster mass estimates. This paper is organized as follows. In Sec. 2 we describe the sample selection. The data and instrument are introduced in Sec. 3, while Sec. 4 focuses on the methods applied for mapping the data, identifying radio source foregrounds and removing them from the maps. The analysis of the cluster + radio sources environment is outlined in Sec. 5. Given the difficulty of comparing cluster mass measurements from different data, we provide considerable detail in our results section, Sec. 6. In particular, we present: maps; details on the radio source environment towards the clusters; full cluster parameter posterior distributions internal to two overdensities,  $r_{500}$  and  $r_{200}$ ; an investigation of contaminating radio sources (our main source of systematic error); and we compare our  $\beta$ -model parameterization with several generalized Navarro-Frenk-White (gNFW) parameterizations. In Sec. 7 we illustrate the ability of our methodology to recover the cluster mass even for a cluster with a challenging source environment. In Sec. 7 we discuss our results, in particular, the morphology and dynamical state of the clusters and the comparison of SZ-, weak lensing- and X-ray-derived cluster masses and large  $r$  X-ray and SZ temperatures. The conclusions of our study are summarized in Sec. 9.

Throughout, we assume a concordance  $\Lambda$ CDM cosmology with  $\Omega_{m,0} = 0.3$ ,  $\Omega_{\Lambda,0} = 0.7$ ,  $\Omega_k = 0$ ,  $\Omega_{b,0} = 0.041$ ,  $w_0 = -1$ ,  $w_a = 0$  and  $\sigma_8 = 0.8$ . For the probability distribution plots and the tables, we take  $h = H_0/100 \text{ km s}^{-1} \text{ Mpc}^{-1}$ ; elsewhere we take  $H_0 = 70 \text{ km s}^{-1} \text{ Mpc}^{-1}$  as the default value and also refer when necessary to  $h_X = H_0/X \text{ km s}^{-1} \text{ Mpc}^{-1}$ . All coordinates are at epoch J2000.

## 2 THE LOCUSS CATALOGUE AND OUR SUB-SAMPLE

LoCuSS (Smith et al. 2003, 2004) is a multi-wavelength survey of 164 X-ray luminous ( $L_X \geq 2 \times 10^{37} \text{ W}$  over the 0.1-2.4 keV band in the cluster rest frame (Ebeling et al. 1998 and Ebeling et al. 2000,  $h_{50} = 1$ ) galaxy clusters. The narrow range of redshifts  $z$  ( $0.142 \leq z \leq 0.295$ ) minimises cosmic evolution. The clusters have been selected from the *ROSAT* All-Sky Survey (Ebeling et al. 1998, 2000; Böhringer et al. 2004) without taking into account their structures or dynamical states. Relevant LoCuSS papers include Marrone et al. (2009) and Zhang et al. (2010).

In this work, we study a sub-sample of 19 clusters from the LoCuSS catalogue and Abell 1758b<sup>1</sup> (Tab. 1) using 16-GHz interferometric AMI data with arcminute resolution. Our sub-sample includes only those clusters with  $\delta > 20^\circ$ . AMI can observe down to lower declinations but suffers from poorer  $uv$ -coverage and satellite interference at  $\delta < 20^\circ$ . We also applied an X-ray luminosity cut,  $L_X > 7 \times 10^{37} \text{ W}$  (0.1-2.4 keV restframe,  $h_{50} = 1$ ), lower-luminosity clusters tend to be fainter in SZ. Contamination from radio sources at 16 GHz can significantly affect our SZ detections. For this reason, we have chosen to exclude clusters with sources brighter than  $10 \text{ mJy beam}^{-1}$  within  $10'$  of the cluster X-ray centre.

Several studies of the LoCuSS sample of clusters are ongoing. These include both ground-based (Gemini, Keck, MMT, NOAO, Palomar, Subaru, SZA, UKIRT and VLT) as well as space-based (CHANDRA, HST, GALEX, XMM-NEWTON and Spitzer) facilities. Our AMI SZ data are complementary to other data taken towards

these clusters as they probe the large-scale gas structure, are sensitive to gas from destroyed density peaks and are particularly beneficial for obtaining robust cluster masses since the SZ signal has long been recognised as a good mass proxy (see e.g., Motl et al. 2005).

## 3 INSTRUMENT AND OBSERVATIONS

AMI consists of two aperture-synthesis interferometric arrays located near Cambridge. The Small Array (SA) is optimized for SZ imaging while the Large Array (LA) is used to observe radio sources that contaminate the SZ effect in the SA observations. AMI's  $uv$ -coverage is well-filled all the way down to  $\approx 180\lambda$ , corresponding to a maximum angular scale of  $\approx 10'$ . AMI is described in detail in AMI Consortium: Zwart et al. (2008)<sup>2</sup>.

SA pointed observations of all the clusters were taken between 2007 and 2010 while LA raster observations, which were mostly 61+19 pt hexagonal rasters<sup>3</sup> centred on the cluster X-ray position, were made between 2008 and 2010. Typically, each cluster was observed for 20-80 hours with the SA and for 10-25 hours with the LA. The thermal noise levels for the SA ( $\sigma_{SA}$ ) and for the LA ( $\sigma_{LA}$ ) were obtained by applying the AIPS<sup>4</sup> task IMEAN on a section of the map far down the primary beam and free from any significant contamination. In Tab. 2 we provide central thermal noise estimates for the SA and LA observations; they reflect the amounts of data remaining after flagging. A series of algorithms has been developed to remove (or 'flag-out') bad data points arising from interference, shadowing, hardware and other errors. This is a stringent process that typically results in  $\approx 30$ -50% of data being discarded before the analysis. A primary-beam correction factor has been applied, as the thermal noise level is dependant on the distance from the pointing centre.

The raw visibility files were put through our local data reduction pipeline, REDUCE, described in detail in AMI Consortium: Davies et al. (2010), and exported in FITS format. Bi-daily observations of 3C286 and 3C84 were used for flux calibration while interleaved calibrators selected from the Jodrell Bank VLA Survey (Patnaik et al. 1992; Browne et al. 1998; Wilkinson et al. 1998) were observed every hour for phase calibration.

## 4 MAPPING AND SOURCE DETECTION AND SUBTRACTION

Our LA map-making and source-finding procedures follow AMI Consortium: Shimwell et al. (2010). We applied standard AIPS tasks to image the continuum and individual-channel UVFITS data output from REDUCE.

At 16 GHz, the dominant contaminants to the SZ decrements are radio sources. In order to recover the SZ signal, the contribution of these radio sources to the data need to be removed; this is done as follows.

<sup>2</sup> The observing frequency range given in AMI Consortium: Zwart et al. has been altered slightly, as described in AMI Consortium: Franzen et al. 2010.

<sup>3</sup> A 61+19 point raster observation consists of 61 pointings with separations of  $4'$ , of which the central 19 pointings have lower noise levels, see e.g., AMI Consortium: Hurley-Walker et al. (2011) for example LA maps.

<sup>4</sup> <http://www.aips.nrao.edu>

<sup>1</sup> Abell 1758b was serendipitously observed in the field of view of Abell 1758a, a LoCuSS cluster.

**Table 1.** Cluster details. It should be noted that Abell 1758b is not part of LoCuSS.

Cluster	Right ascension (J2000)	Declination (J2000)	Redshift	X-ray luminosity /10 <sup>37</sup> W ( $h_{50} = 1$ ; see text)	Alternative cluster names
Abell 586	07 32 12	+31 37 30	0.171	11.1	
Abell 611	08 00 56	+36 03 40	0.288	13.6	
Abell 621	08 11 09	+70 02 45	0.223	7.8	
Abell 773	09 17 54	+51 42 58	0.217	13.1	RXJ0917.8+5143
Abell 781	09 20 25	+30 31 32	0.298	17.2	
Abell 990	10 23 39	+49 08 13	0.144	7.7	
Abell 1413	11 55 18	+23 24 29	0.143	13.3	
Abell 1423	11 57 18	+33 36 47	0.213	10.0	RXJ1157.3+3336
Abell 1704	13 14 18	+64 33 27	0.216	7.8	
Abell 1758a	13 32 45	+50 32 31	0.280	11.7	
Abell 1758b	13 32 29	+50 24 42	0.280	7.3	
Abell 2009	15 00 21	+21 22 04	0.153	9.1	
Abell 2111	15 39 40	+34 26 00	0.229	10.9	
Abell 2146	15 55 58	+66 21 09	0.234	9.0	
Abell 2218	16 35 45	+66 13 07	0.171	9.3	
Abell 2409	22 00 57	+20 57 50	0.147	8.1	
RXJ0142+2131	01 42 03	+21 31 40	0.280	9.9	
RXJ1720.1+2638	17 20 10	+26 37 31	0.164	16.1	
Zw0857.9+2107	09 00 39	+20 55 17	0.235	10.8	Z2089
Zw1454.8+2233	14 57 15	+22 20 34	0.258	13.2	Z7160

• First, the CLEANED LA continuum maps<sup>5</sup> were put through the AMI-developed source-extraction software SOURCEFIND (AMI Consortium: Franzen et al. 2010) to identify and characterize radio sources on the LA maps above a certain signal-to-noise. SOURCEFIND provides estimates for the right ascension  $x_s$ , declination  $y_s$ , flux density<sup>6</sup>,  $S_0$ , and spectral index  $\alpha$ <sup>7</sup> at the central frequency  $\nu_0$  for identified radio sources. We impose a detection threshold such that we select only those radio sources with a flux density  $\geq 4\sigma_{LA_p}$  on the CLEANED LA continuum maps, where  $\sigma_{LA_p}$  refers to pixel values on the LA noise maps. The number of  $\geq 4\sigma_{LA_p}$  sources detected in our LA observations of each cluster is given in Tab. 2.

• Second, *prior to any source subtraction*, we run our cluster-analysis software, which fits for the position, flux and spectral index of the SOURCEFIND-detected radio sources using the source parameters obtained by SOURCEFIND as priors. For some of the less contaminating radio sources, our cluster-analysis software uses delta-priors for the source parameters centred at the LA estimates (see Sec. 5 for further details).

• Third, the source parameters given by the cluster analysis were used to perform source subtraction on the SA maps. This was done using in-house software, MUESLI, which is an adaptation of the standard AIPS task UVSUB optimized for processing AMI data. The flux-density contributions from detected radio sources were subtracted from each SA channel UVFITS file using either the mean values for their position, spectral index and flux density derived from our Bayesian analysis, when these parameters are not given delta-function priors, or, otherwise, using the LA estimates for these source parameters. Details of the priors assigned to each of the

sources labelled on the SA maps can be found in Sec. 5.2.2 and Tab. 4.

• Fourth, after source subtraction, the SA maps were CLEANED with a tight box around the SZ signal. In contrast, the LA maps and SA maps before source subtraction were CLEANED with a single box comprising the entire map. Both the SA and the LA maps were CLEANED down to  $3\sigma$ .

## 5 ANALYSIS

We use our own Bayesian analysis package, McADAM, to estimate cluster parameters internal to  $r_{500}$  and  $r_{200}$  from AMI data in the presence of radio point sources, receiver noise and primordial CMB anisotropy. The cluster and radio sources are parameterized in our analysis (see below) while the remaining components are included in a generalized noise covariance matrix; we note that these are the only significant noise contributions because large-scale emission from e.g., foreground galactic emission is resolved out by our interferometric observations.

McADAM was originally developed by Marshall et al. (2003) and Feroz et al. (2009) adapted it to work on AMI data. The latest McADAM uses MULTINEST (Feroz & Hobson 2008, Feroz, Hobson & Bridges 2009) as its inference engine to allow Bayesian evidence and posterior distributions to be calculated efficiently, even for posterior distributions with large (curved) degeneracies and/or multiple peaks. This addition has been key to our analysis since the posteriors of AMI data often have challenging dimensionalities,  $> 30$ , primarily as a result of the presence of a large number of radio sources in the AMI observations.

<sup>5</sup> The LA continuum maps were CLEANED down to  $3\sigma_{LA}$  with no boxes.

<sup>6</sup> We catalogue the peak flux of the source, unless the source is extended, in which case we integrate the source surface brightness over its projected solid angle to give its integrated flux density (see e.g., AMI Consortium: Franzen et al. 2010).

<sup>7</sup> We adopt the convention  $S \propto \nu^{-\alpha}$ .



**Table 2.** Observational details. SA and LA noise levels,  $\sigma_{SA}$  and  $\sigma_{LA} \geq 4\sigma$  and the number of sources detected above  $4\sigma_{LA}$  on the LA rasters for each cluster. Abell 1758b is not part of LoCuSS.

Cluster	$\sigma_{SA}$ (mJy)	$\sigma_{LA}$ (mJy)	Number of LA $4\sigma_{LA}$ sources
Abell 586	0.17	0.09	23
Abell 611	0.11	0.07	23
Abell 621	0.11	0.09	13
Abell 773	0.13	0.09	9
Abell 781	0.12	0.07	24
Abell 990	0.10	0.08	20
Abell 1413	0.13	0.09	17
Abell 1423	0.08	0.07	31
Abell 1704	0.09	0.06	13
Abell 1758a	0.12	0.08	14
Abell 1758b	0.13	0.08	14
Abell 2009	0.11	0.14	18
Abell 2111	0.09	0.07	22
Abell 2146	0.15	0.06	15
Abell 2218	0.07	0.10	15
Abell 2409	0.14	0.05	15
RXJ0142+2131	0.11	0.06	22
RXJ1720.1+2638	0.08	0.10	17
Zw0857.9+2107	0.13	0.12	13
Zw1454.8+2233	0.10	0.10	16

## 5.1 Model

We have modelled the cluster density profile assuming spherical symmetry using a  $\beta$ -model (Cavaliere & Fusco-Fermiano 1978):

$$\rho_g(r) = \frac{\rho_g(0)}{\left[1 + \left(\frac{r}{r_c}\right)^2\right]^{\frac{3\beta}{2}}}, \quad (1)$$

where gas mass density  $\rho_g(r) = \mu n(r)$ ,  $\mu = 1.14m_p$  is the gas mass per electron and  $m_p$  is the proton mass. The core radius  $r_c$  gives the density profile a flat top at low  $\frac{r}{r_c}$  and  $\rho_g$  has a logarithmic slope of  $3\beta$  at large  $\frac{r}{r_c}$ .

We choose to model the gas as isothermal, using the virial mass-temperature relation and assuming that all kinetic energy is in gas internal energy:

$$k_B T(r_{200}) = \frac{G\mu M_T(r_{200})}{2r_{200}} \quad (2)$$

$$= \frac{G\mu}{2\left(\frac{3}{4\pi(200\rho_{crit})}\right)^{1/3}} M_T^{2/3}(r_{200}) \quad (3)$$

$$= 8.2\text{keV} \left(\frac{M_T(r_{200})}{10^{15}h^{-1}M_\odot}\right)^{2/3} \left(\frac{H(z)}{H_0}\right)^{2/3}. \quad (4)$$

$M_T(r_{200})$  and  $T(r_{200})$  refer to the total mass and gas temperature within  $r_{200}$  (see e.g., Voit 2005). This relation allows cluster parameters within  $r_{200}$  to be inferred without assuming hydrostatic equilibrium; note that, in our methodology, parameters describing the cluster at smaller  $r$  (e.g.,  $r_{500}$ ) do, however, assume hydrostatic equilibrium. Further details of the cluster analysis can be found in AMI Consortium: Rodríguez-González et al. (2010) and AMI Consortium: Olamaie et al. (2011). The good agreement between mass estimates from weak-lensing and AMI data on 6 clusters in AMI Consortium: Hurley-Walker et al. (2011) supports the use of this  $M - T$  relation in our analysis.

## 5.2 Priors

### 5.2.1 Cluster priors

The cluster model parameters  $\Theta_c = (x_c, y_c, M_T(r_{200}), f_g(r_{200}), \beta, r_c, z)$  have priors that are assumed to be separable.  $x_c, y_c$  are the cluster position (RA and Dec, respectively) and  $f_g$  is the gas fraction, which is defined as

$$f_g = \frac{M_g}{M_T}. \quad (5)$$

Further details on these priors are given in Tab. 3.

This set of sampling parameters has proved sufficient for our cluster detection algorithm (AMI Consortium: Shimwell et al. 2010) and to describe the physical cluster parameters. We emphasize that this way of analysing the data is *different* from the way used traditionally, in which an X-ray spectroscopic temperature is used as an input parameter. The difficulty with this use of an X-ray temperature is that, in practice, the temperature measurement usually applies to gas relatively close to the cluster centre (but any cooling flow is excised). By sampling from  $M_T$  and using the  $M - T$  relation (Eq. 4), the *temperature of each cluster is derived from SZ data only* and is averaged over the angular scale of the SZ observation, which is typically larger than the angular scale of the X-ray temperature measurement. This way, although our analysis does not yield  $T(r)$ , it gives and uses a temperature which is representative of the cluster volume we are investigating.

### 5.2.2 Source priors

Radio sources detected on the LA maps using SOURCEFIND are modelled by four source parameters,  $\Theta_S = (x_s, y_s, S_0, \alpha)$ . Priors on these parameters are based on LA measurements, discussed in Sec. 4.

Sources on the source-subtracted SA maps are labelled according to Tab. 4. Delta-function priors on all the source parameters tend to be given to those sources whose flux density is  $< 4\sigma_{SA}$  and to those outside the 10% radius of the SA power primary beam. The remaining sources are usually assigned a delta-function prior on position and Gaussian priors on  $\alpha$  and  $S_0$ . However, in a few cases we

**Table 3.** Summary of the priors for the sampling parameters in each model. The value for the redshift and position priors have not been included in this table since they are cluster specific. Instead, they are given in Tab. 1 for each cluster.

Parameter	Prior Type	Values	Origin
$x_c, y_c''$	Gaussian at $\mathbf{x}_{X\text{-ray}}, \sigma = 60''$	cluster position	Ebeling et al. (2000)
$\beta$	uniform	0.3 – 2.5	Marshall et al. (2003)
$M_T(r_{200})/h^{-1}M_\odot$	uniform in log	$1 \times 10^{13.5} - 5 \times 10^{15}$	physically reasonable, e.g., Vikhlinin et al. 2006
$r_c/h^{-1}\text{kpc}$	uniform	10 – 1000	physically reasonable e.g., Vikhlinin et al. 2006
$z$	delta	cluster redshift	Ebeling et al. (2000)
$f_g(r_{200})/h^{-1}$	Gaussian, $\sigma = 0.0216$	0.0864	Larson et al. (2011); Zhang et al. (2010)

**Table 4.** Priors on position, spectral index and flux density given to detected sources. The symbols correspond to the labels in the SA source-subtracted maps. The Gaussian priors are centred on the LA measurements.  $\sigma$  values for the Gaussian priors are assigned as follows: for the Gaussian prior on the flux-density of each radio source,  $\sigma$  is set to 40% of the source flux density; for the spectral index  $\alpha$ ,  $\sigma$  is set to the LA error on  $\alpha$  and for the source position,  $\sigma$  is set to  $60''$ .

Symbol	$\Pi(S_0)$	$\Pi(\alpha)$	$\Pi(x_s, y_s)$
+	delta	delta	delta
×	Gaussian	Gaussian	delta
$\Delta$	Gaussian	Gaussian	Gaussian

replace delta-function priors on the source parameters with Gaussian priors as this can increase the accuracy of the source subtraction. These wider priors can be necessary to account for discrepancies between the LA and SA measurements. Reasons for these differences include: a poor fit of our Gaussian model for the power primary beam far from the pointing centre, correlator artifacts, source variability and source extension.

## 6 RESULTS AND COMMENTARY

Out of the 20 clusters listed in Tab. 1, we detect SZ decrements towards 17. For these clusters we present SA maps before and after source subtraction as well as marginalized posterior distributions for some cluster and source parameters and mean values of selected cluster parameters (Tab. 6), with the exception of Abell 2409, which was found to have a local environment which renders it unsuitable for robust parameter estimation (see Sec. 6.16). For the posterior distributions all ordinates and abscissae in these plots are linear, the y-axis for the 1-d marginals is the probability density and  $h$  is short for  $h_{100}$ . It is important to note that, while the posterior probability distributions for large-scale cluster parameters reflect the uncertainty in the McADAM-derived flux-density estimates, the radio source-subtracted maps do not, as they simply use a single value (the mean) for each source parameter. The effect of our priors on the results has been thoroughly tested in a previous study by AMI Consortium: Olamaie et al. (2011), which found that the priors used in this parameterization do not to lead to any strong biases in the cluster parameter estimates.

The SA maps have labels indicating the position of detected radio sources and their priors (Tab. 4); the square box in these plots indicates the best-fit cluster position determined by McADAM. No primary-beam correction has been applied to the SA maps presented in this paper, unless stated otherwise. The contour levels on the SA maps, unless otherwise stated, start at  $2\sigma_{SA}$  and increase linearly from 2 to  $10\sigma_{SA}$ . On radio-only images, positive contours are shown as solid lines and negative contours as dashed lines, but on radio+X-ray images, negative radio contours are shown as solid lines and X-ray shown as greyscale. The bottom-left ellipses on the

SA maps are the FWHMs of the synthesized beams. A  $0.6\text{-k}\lambda$  taper was applied to the SA source-subtracted maps to downweight long-baseline visibilities with the purpose of increasing the signal-to-noise of the large-scale structure; this typically leads to a  $\approx 20\%$  increase in the noise. The X-ray images are obtained from archive *ROSAT* and *CHANDRA* data.

We remind readers that when looking at a radio map – necessarily with a particular  $uv$ -weighting – a near-circular image does not mean that the SA failed to resolve the SZ signal. Investigating angular structure / size requires assessment in  $uv$ -space, which can be done with a selection of maps made over different  $uv$  ranges but is optimally done here in  $uv$ -space with McADAM. In fact, all the SZ decrements in this paper *are* resolved.

Table 5: Source properties for detected sources within 5' of the SZ mean central position. The number next to each cluster name denotes the source number; this label is used in the plots showing the marginalized posterior distributions for the source fluxes.  $S_0$ McA is the McADAM-derived best-fit source flux at 16 GHz.  $\alpha$  is the source spectral index estimated by McADAM and centred at the McADAM-derived mean frequency and the last column contains the distance between the cluster SZ centroid (as determined by McADAM) and the source.

Name	Right ascension (hh:mm:ss , J2000)	Declination (°:':", J2000)	$S_0$ McA mJy	$\alpha$	Distance from SZ centroid "
A586_0	07:32:20.5	+31:38:02.8	0.26	1.20	28
A586_1	07:32:19.1	+31:40:25.6	0.86	0.28	171
A586_2	07:32:11.0	+31:39:47.6	0.86	1.20	178
A586_3	07:32:04.5	+31:39:09.6	0.41	1.53	222
A586_4	07:32:35.4	+31:35:35.5	1.03	-0.47	227
A586_5	07:32:21.2	+31:41:26.3	7.44	0.46	232
A586_6	07:32:42.7	+31:38:37.1	0.53	0.16	293
A611_0	08:01:07.0	+36:02:18.9	0.32	-0.27	108
A611_1	08:00:52.6	+36:06:14.2	0.44	2.18	199
A611_2	08:01:17.0	+36:04:27.8	0.5	-0.71	229
A621_3	08:11:12.8	+70:02:27.2	7.18	1.34	25
A621_4	08:11:19.3	+70:00:48.4	0.6	-1.31	127
A621_5	08:11:35.2	+70:04:25.6	0.16	0.13	166
A621_6	08:10:38.0	+70:04:09.3	0.09	0.01	181
A781_0	09:20:24.7	+30:31:49.9	0.24	-0.04	4
A781_1	09:20:23.3	+30:29:49.3	8.97	0.97	126
A781_2	09:20:08.4	+30:32:15.8	1.49	-0.18	213
A781_3	09:20:14.0	+30:28:60.0	2.12	0.63	223
A990_0	10:23:47.3	+49:11:25.5	0.44	-0.21	208
A990_1	10:24:02.1	+49:06:51.8	2.78	2.18	239
A1413_0	11:55:15.4	+23:23:59.4	0.47	1.04	59
A1413_1	11:55:08.8	+23:26:16.6	3.1	0.98	222
A1423_2	11:57:17.1	+33:36:30.6	0.54	-0.19	63
A1423_3	11:57:28.5	+33:35:31.0	0.26	2.16	134
A1423_4	11:57:19.7	+33:39:58.3	0.39	0.73	171
A1423_5	11:57:35.2	+33:37:21.8	0.19	0.58	176
A1423_6	11:57:40.5	+33:35:10.1	0.18	-0.40	270
A1423_7	11:57:20.5	+33:41:57.8	0.73	-0.22	290
A1423_8	11:57:39.0	+33:34:03.3	0.24	1.47	290
A1704_0	13:14:02.3	+64:38:29.5	0.2	-0.03	273
A1704_1	13:14:52.6	+64:37:59.9	0.81	0.86	287
A1758a_0	13:32:53.3	+50:31:40.6	7.08	0.5	54
A1758a_1	13:32:38.6	+50:33:37.7	0.77	0.36	150
A1758a_2	13:33:02.2	+50:29:26.4	1.43	0.28	190
A1758a_3	13:32:39.6	+50:34:31.1	0.3	1.45	192
A1758a_4	13:32:41.5	+50:26:47.7	0.46	-0.76	294
A1758b_0	13:32:33.1	+50:22:35.1	0.23	0.11	90
A1758b_1	13:32:41.5	+50:26:47.7	0.51	-0.68	196
A2009_0	15:00:19.7	+21:22:12.6	1.85	3.14	58
A2009_1	15:00:28.6	+21:22:45.8	0.18	0.66	133
A2009_2	15:00:19.6	+21:22:11.3	1.97	2.64	77
A2009_3	15:00:28.6	+21:22:45.7	0.18	0.66	135

Table 5: Source properties for detected sources within 5' of the SZ mean central position. The number next to each cluster name denotes the source number; this label is used in the plots showing the marginalized posterior distributions for the source fluxes.  $S_0\text{McA}$  is the McADAM-derived best-fit source flux at 16 GHz.  $\alpha$  is the source spectral index estimated by McADAM and centred at the McADAM-derived mean frequency and the last column contains the distance between the cluster SZ centroid (as determined by McADAM) and the source.

Name	Right ascension (hh:mm:ss, J2000)	Declination (°:':", J2000)	$S_0\text{McA}$ mJy	$\alpha$	Distance from SZ centroid "
A2111_0	15:39:30.1	+34:29:05.5	0.5	0.68	222
A2111_1	15:39:56.7	+34:29:31.8	0.81	-1.47	297
A2146_0	15:56:04.2	+66:22:13.0	5.94	0.55	43
A2146_1	15:56:14.0	+66:20:53.5	1.82	1.03	59
A2146_2	15:56:15.4	+66:22:44.5	0.15	0.34	89
A2146_3	15:55:57.4	+66:20:03.1	1.67	-0.22	106
A2146_4	15:56:27.1	+66:19:43.8	0.1	0.64	164
A2146_5	15:55:25.7	+66:22:04.0	0.48	-0.22	249
A2218_0	16:35:47.4	+66:14:46.1	2.86	0.07	100
A2218_1	16:35:21.8	+66:13:20.6	5.99	0.23	141
A2218_2	16:36:15.6	+66:14:24.0	1.77	0.72	200
A2409_0	22:00:39.7	+20:58:55.0	0.75	1.9	241
A2409_1	22:01:11.2	+20:54:56.8	3.12	0.1	275
RXJ0142+2131_0	01:42:09.2	+21:33:23.4	1.09	0.7	117
RXJ0142+2131_1	01:42:11.0	+21:29:45.3	1.16	1.52	156
RXJ0142+2131_2	01:42:23.3	+21:30:46.7	0.3	0.03	273
RXJ1720+2638_0	17:20:10.0	+26:37:29.7	6.92	1.24	46
RXJ1720+2638_1	17:20:01.2	+26:36:32.3	2.05	0.57	105
RXJ1720+2638_2	17:19:58.4	+26:34:19.6	1.22	1.46	203
RXJ1720+2638_3	17:20:25.5	+26:37:57.2	0.88	0.89	234
Zw0857.9+2107_0	09:00:36.9	+20:53:41.4	1.22	0.31	102
Zw0857.9+2107_1	09:00:55.5	+20:57:21.2	0.96	1.37	259
Zw0857.9+2107_2	09:00:52.8	+20:58:36.5	5.57	0.09	274
Zw1454.8+2233_0	14:57:14.8	+22:20:34.2	1.64	0.28	14
Zw1454.8+2233_1	14:57:08.2	+22:20:08.6	1.55	1.89	108
Zw1454.8+2233_2	14:57:10.6	+22:18:45.6	1.49	0.94	137
Zw1454.8+2233_3	14:56:58.9	+22:18:49.6	8.36	0.17	258
Zw1454.8+2233_4	14:57:04.3	+22:24:11.9	0.83	-0.63	260
Zw1454.8+2233_5	14:57:24.8	+22:24:52.6	0.13	-0.25	281
Zw1454.8+2233_6	14:57:35.7	+22:19:46.8	1.04	1.67	285

**Table 6.** Mean and 68%-confidence uncertainties for some McADAM-derived large-scale cluster parameters.

Cluster name	$M_T(r_{200})$ $\times 10^{14} h_{100}^{-1} M_\odot$	$M_T(r_{500})$ $\times 10^{14} h_{100}^{-1} M_\odot$	$M_g(r_{200})$ $\times 10^{13} h_{100}^{-2} M_\odot$	$M_g(r_{500})$ $\times 10^{13} h_{100}^{-2} M_\odot$	$r_{200}$ $h_{100}^{-1}$ Mpc	$r_{500}$ $\times 10^{-1} h_{100}^{-1}$ Mpc	$T_{\text{AMI}}$ keV	$Y(r_{200})$ $\times 10^{-5}$ arcmin <sup>2</sup>	$Y(r_{500})$ $\times 10^{-5}$ arcmin <sup>2</sup>
A586	$5.1 \pm 2.1$	$2.1 \pm 0.9$	$4.3 \pm 1.7$	$2.6 \pm 0.7$	$1.2 \pm 0.2$	$6.6 \pm 1.0$	$5.2 \pm 1.4$	$3.6^{+2.0}_{-2.1}$	$2.7 \pm 1.4$
A611	$4.0^{+0.7}_{-0.8}$	$2.0 \pm 0.5$	$3.5 \pm 0.6$	$2.8 \pm 0.3$	$1.1 \pm 0.1$	$6.3 \pm 0.5$	$4.5 \pm 0.6$	$2.2 \pm 0.5$	$2.1 \pm 0.4$
A621	$4.8^{+1.7}_{-1.8}$	$1.4 \pm 0.9$	$4.1 \pm 1.0$	$1.5 \pm 0.8$	$1.2^{+0.2}_{-0.1}$	$5.3^{+0.2}_{-0.1}$	$5.0 \pm 1.2$	$3.1^{+1.5}_{-1.6}$	$1.9 \pm 1.0$
A773	$3.6 \pm 1.2$	$1.7 \pm 0.6$	$3.1^{+1.0}_{-0.9}$	$2.1 \pm 0.4$	$1.1 \pm 0.1$	$6.0 \pm 0.7$	$4.1^{+0.9}_{-1.0}$	$1.9 \pm 0.9$	$1.6^{+0.6}_{-0.7}$
A781	$4.1 \pm 0.8$	$2.0 \pm 0.5$	$3.6 \pm 0.6$	$2.9 \pm 0.4$	$1.1 \pm 0.1$	$6.3 \pm 0.5$	$4.5 \pm 0.6$	$2.3 \pm 0.6$	$2.2 \pm 0.5$
A990	$2.0^{+0.4}_{-0.1}$	$1.1 \pm 0.2$	$1.8 \pm 0.3$	$1.6 \pm 0.2$	$0.9 \pm 0.1$	$5.5 \pm 0.3$	$2.8 \pm 0.3$	$0.7 \pm 0.2$	$0.7 \pm 0.15$
A1413	$4.0 \pm 1.0$	$1.9 \pm 0.6$	$3.5 \pm 0.8$	$2.7 \pm 0.4$	$1.1 \pm 0.1$	$6.6 \pm 0.6$	$4.4 \pm 0.7$	$2.2^{+0.7}_{-0.8}$	$2.1 \pm 0.6$
A1423	$2.2 \pm 0.8$	$1.1 \pm 0.4$	$1.9 \pm 0.7$	$1.5 \pm 0.4$	$0.9 \pm 0.1$	$5.3 \pm 0.6$	$3.0^{+0.8}_{-0.7}$	$0.9 \pm 0.5$	$0.8 \pm 0.4$
A1758a	$4.1^{+0.7}_{-0.8}$	$2.5 \pm 0.4$	$3.6 \pm 0.5$	$3.4 \pm 0.4$	$1.1 \pm 0.1$	$6.8 \pm 0.4$	$4.5 \pm 0.5$	$2.3 \pm 0.5$	$2.3 \pm 0.4$
A1758b	$4.4 \pm 1.9$	$2.2 \pm 1.0$	$3.7^{+1.6}_{-1.5}$	$2.2 \pm 0.5$	$1.1 \pm 0.2$	$6.4^{+1.1}_{-1.0}$	$4.6 \pm 1.4$	$2.7 \pm 1.7$	$1.6 \pm 0.6$
A2009	$4.6 \pm 1.5$	$2.0^{+0.2}_{-0.6}$	$3.9 \pm 0.7$	$2.4^{+0.2}_{-0.3}$	$1.2 \pm 0.1$	$6.5^{+0.4}_{-0.6}$	$4.8^{+0.4}_{-0.6}$	$2.8^{+1.3}_{-1.4}$	$2.2 \pm 0.9$
A2111	$4.2 \pm 0.9$	$1.8 \pm 0.5$	$3.6 \pm 0.7$	$2.5 \pm 0.3$	$1.1 \pm 0.1$	$6.2 \pm 0.6$	$4.6 \pm 0.6$	$2.4^{+0.6}_{-0.7}$	$2.2 \pm 0.5$
A2146	$5.0 \pm 0.7$	$2.7 \pm 0.5$	$4.4 \pm 0.5$	$3.7 \pm 0.4$	$1.2 \pm 0.1$	$7.1 \pm 0.5$	$5.2 \pm 0.5$	$3.2 \pm 0.5$	$3.1 \pm 0.4$
A2218	$6.1 \pm 0.9$	$2.7 \pm 0.6$	$5.4^{+0.6}_{-0.7}$	$4.3 \pm 0.4$	$1.3 \pm 0.1$	$7.3 \pm 0.5$	$5.9 \pm 0.6$	$4.5 \pm 0.7$	$4.4 \pm 0.7$
RXJ0142+2131	$3.7^{+1.1}_{-1.2}$	$1.7 \pm 0.6$	$3.1^{+0.9}_{-1.0}$	$2.1 \pm 0.4$	$1.0 \pm 0.1$	$5.9^{+0.8}_{-0.7}$	$4.2 \pm 0.9$	$2.0^{+0.8}_{-0.9}$	$1.5^{+0.6}_{-0.5}$
RXJ1720+2638	$2.0 \pm 0.4$	$1.2 \pm 0.2$	$1.7 \pm 0.3$	$1.6 \pm 0.3$	$0.9 \pm 0.1$	$5.6 \pm 0.4$	$2.8 \pm 0.4$	$0.7 \pm 0.2$	$0.7 \pm 0.2$

### 6.1 Comparison with gNFW parameterizations

The adequacy of different profiles, such as the  $\beta$ , Navarro Frenk and White (NFW), generalized NFW (gNFW, Navarro, Frenk, & White 1996) and other hybrid profiles (e.g., Mroczkowski 2011, Allison et al. 2011, Olamaie, Hobson, & Grainge 2011) is still very much under debate. We attempt to illustrate the impact that the choice of some of these profiles may have on the parameter estimates by comparing the results obtained from five gNFW parameterizations and from our  $\beta$  parameterization (see Sec. 5) for two clusters: Abell 611 (see Sec. 6.3) and Abell 2111 (see Sec. 6.13).

For this analysis we sample from the cluster position parameters ( $x_c, y_c$ ),  $\theta_S = r_S/D_A$ , and  $Y_\theta = Y_{\text{tot}}/D_A^2$ ,  $r_s$  is the scale radius,  $D_A$  the angular diameter distance and  $Y_{\text{tot}} = Y_{\text{sph}}(5r_{500})$ , where  $Y_{\text{sph}}$  is the integrated Compton  $y$  parameter within  $5r_{500}$  (Arnaud et al. (2010) take  $5r_{500}$  as the radius where the pressure profile flattens). Assuming a spherical geometry,  $Y_{\text{sph}}$  is calculated by integrating the plasma pressure within a spherical volume of radius  $r$ :

$$Y_{\text{sph}}(r) = \frac{\sigma_T}{m_e c^2} \int_0^r P_e(r') 4\pi r'^2 dr', \quad (6)$$

where  $\sigma_T$  is the Thomson scattering cross-section,  $m_e$  is the electron mass,  $c$  is the speed of light and  $P_e(r)$  is the electron pressure at radius  $r$ . The following priors were given for the sampling parameters: an exponential prior between  $1.3'$  and  $45'$  for  $\theta_S$  and a power law prior between 0.0005 and 0.2 arcmin<sup>2</sup> for  $Y_{\text{sph}}/D_A^2$ , with a power law index of 1.6. We note that for the purposes of this exercise – to show the different degeneracies for different, plausible sets of gNFW-profile parameters – such wide priors are acceptable; naturally, where appropriate, the prior ranges can be refined. We choose to use a pressure profile for this parameterization since self-similarity has been shown to hold best for this quantity and pressure profiles have low cluster-to-cluster scatter (e.g., Nagai et al. 2007). The gNFW profile is given by

$$P_e(r) = \frac{P_{e,i}}{(r/r_s)^c [1 + (r/r_s)^a]^{\frac{b-c}{a}}}. \quad (7)$$

$P_{e,i}$ , the overall normalisation coefficient of the pressure profile, is calculated by computing Eq. (6) for  $5r_{500}$ ; once  $P_{e,i}$  has been found,  $y$  can be obtained. The shape of the gNFW profile is governed by  $c$  in the inner cluster regions ( $r \ll r_s$ ), by  $a$  at intermediate radii ( $r \approx r_s$ ), and by  $b$  on the cluster outskirts ( $r > r_s$ ). These parameters, together with the concentration parameter,  $c_{500}$ , are fixed in most analyses to some best-fit values (e.g., Mroczkowski 2011). With  $c_{500}$ ,  $r_s$  can be expressed in terms of  $r_{500}$ :  $r_s = r_{500}/c_{500}$ , which is a common reparameterization (see e.g., Arnaud et al. 2010 and Nagai et al. 2007).

We ran our analysis using a gNFW profile with parameters defined by Nagai et al. as gNFW<sub>N</sub>, another defined by Arnaud et al. as the ‘universal’ profile gNFW<sub>A</sub>, and three other combinations for the slope parameters and  $c_{500}$  that were found to provide the best fit for some clusters in Arnaud et al.; gNFW<sub>1</sub>, gNFW<sub>2</sub> and gNFW<sub>3</sub><sup>8</sup>. The gNFW parameters for our five choices are given in Tab. 7.

The 2D-marginalized posterior distributions of  $Y_{\text{sph}}(r_{500})$  against  $r_{500}$  obtained for each of the five parameterizations, as well as the  $\beta$  parameterization from Sec. 5, for Abell 611 and Abell 2111 are shown in Fig. 1. We test for possible biases in our results from the choice of priors by running the analysis without data; the results

<sup>8</sup> The parameters for the three other gNFW profiles all lie within  $3\sigma$  of the average value of each parameter obtained using the cluster sample in Arnaud et al. .

**Table 7.** Parameters for the gNFW pressure profile. The parameters for gNFW<sub>A</sub> and gNFW<sub>N</sub> have been taken from Arnaud et al. 2010 and Mroczkowski et al. 2009, respectively. The values in Mroczkowski et al. 2009 are the corrected values for the results published by Nagai et al. 2007.

Profile Label	$a$	$b$	$c$	$c_{500}$
gNFW <sub>1</sub>	1.37	5.49	0.035	2.16
gNFW <sub>2</sub>	0.33	5.49	0.065	0.17
gNFW <sub>3</sub>	2.01	5.49	0.860	1.37
gNFW <sub>A</sub>	1.0620	5.4807	0.3292	1.156
gNFW <sub>N</sub>	0.9	5.0	0.4	1.3

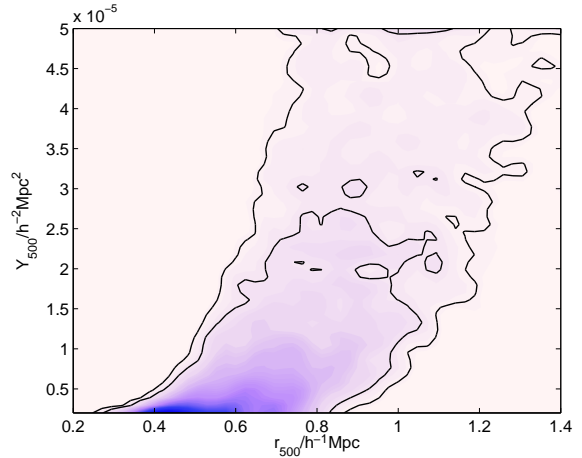


**Figure 2.** 2-D marginalized distribution for  $Y_{\text{sph}}(r_{500})$  against  $r_{500}$  obtained using the  $\beta$ -based cluster parameterization without any data.

indicate the constraints imposed by our priors. We find no evidence for significant biases, as shown in Fig. 2.

When the shape parameters of the  $\beta$  profile are fitted to the SZ data instead of being set to the X-ray value (typically derived for data sensitive to smaller scales than AMI data) we find the mean values for  $Y_{\text{sph}}(r_{500})$  and  $r_{500}$  derived from the  $\beta$  analysis to be consistent (within  $1-2\sigma$ ) with those from gNFW<sub>A</sub> and gNFW<sub>N</sub> – the averaged gNFW profiles. For these two clusters we find all gNFW parameterizations yield lower values for  $Y_{\text{sph}}(r_{500})$  than for the  $\beta$  analysis; this is not the case for  $r_{500}$ , for which no systematic difference is seen. The constraints on  $Y_{\text{sph}}(r_{500})$  are similar for most of the gNFW models (with the exception of gNFW<sub>2</sub>) and the  $\beta$  model, while those for  $r_{500}$  appear to be tighter for the  $\beta$  model. One striking difference between the two types of parameterizations is the shape and orientation of the  $Y_{\text{sph}} - r_{500}$  degeneracy.

The resolution and limited spatial dynamic range of the AMI data do not allow profile selection to be made robustly, as indicated by the small difference in evidence values between the different parameterizations (Tab. 8). Hence, our  $\beta$  parameterization provides a comparable fit to that of the commonly used, averaged gNFW profiles, gNFW<sub>A</sub>, and gNFW<sub>N</sub>. It is clear from Fig. 1 that the distribution for the  $Y_{\text{sph}}(r_{500}) - r_{500}$  degeneracies is very sensitive to the choice for the slope parameters (and  $c_{500}$  for gNFW). Cluster parameters for a cluster with a profile described by e.g., a gNFW<sub>2</sub> recovered using a gNFW<sub>A</sub> parameterization will be biased.

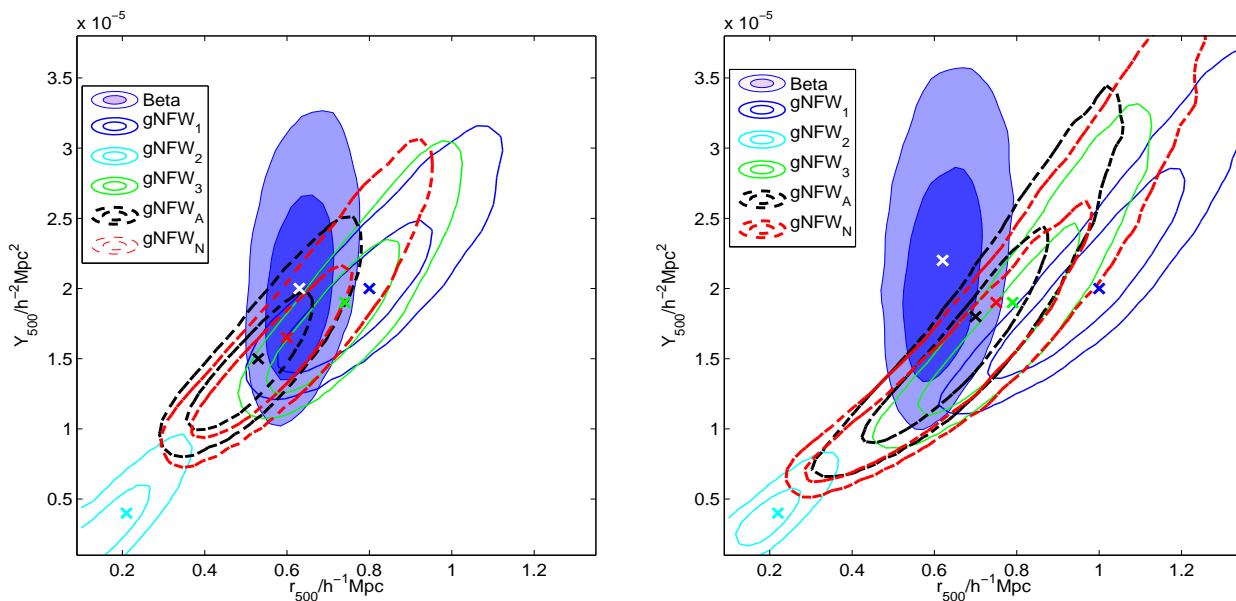


**Figure 1.** 2-D marginalized distributions for  $Y_{\text{sph}}(r_{500})$  against  $r_{500}$  obtained using the  $\beta$ -based cluster parameterization and five gNFW-based cluster parameterizations with slope parameters and  $c_{500}$  given in Tab. 7. The crosses denote the McADAM-derived mean values. The results are for Abell 611 (left) and Abell 2111 (right). The blue filled ellipses show the results of the  $\beta$  parameterization.

**Table 8.** Log<sub>e</sub> evidences for five cluster parameterizations applied to Abell 2111 and Abell 611

	Abell 2111	Abell 611
Profile Label		
gNFW <sub>1</sub>	23198.88	21114.08
gNFW <sub>2</sub>	23199.51	21114.40
gNFW <sub>3</sub>	23198.64	21114.74
gNFW <sub>A</sub>	23198.94	21114.50
gNFW <sub>N</sub>	23198.76	21114.65
$\beta$	23194.92	21112.05

## 6.2 Abell 586

Results for Abell 586 are given in Figs. 3 and 4. This cluster has a complex source environment, with 7 sources within  $5'$  from the cluster SZ centroid, which include two radio sources of  $\approx 260$  and  $744 \mu\text{Jy}$  at  $0.5'$  and  $4'$  from the pointing centre. After source-subtraction there are only  $\approx 1\sigma$  residuals left on the map. Uncertainties in the source fluxes are carried through into the posterior distributions for the cluster parameters. From Fig. 4, it can be seen that there is no strong degeneracy between the source flux densities and the cluster mass.

Abell 586 has been studied extensively in the X-ray band (e.g., Allen 2000 and White 2000). A recent analysis of the temperature profile (Cypriano 2005) shows how the temperature falls from  $\approx 9$  keV at the cluster centre to  $\approx 5.5$  keV at a radius  $\approx 280''$ . Cypriano et al. have used the Gemini Multi-Object Spectrograph together with X-ray data taken from the CHANDRA archive to measure the properties of Abell 586. They compare mass estimates derived from the velocity distribution and from the X-ray temperature profile and find that both give very similar results,  $M_g \approx 0.48 \times 10^{14} M_\odot$  (for  $h_{70} = 1$ ) within  $1.3h_{70}^{-1}$  Mpc. They suggest that the cluster is spherical and relaxed with no recent mergers. It is less clear whether this cluster has a cool core or not, with Allen & Fabian (1998) reporting

its existence and Marrone et al. (2011) saying otherwise. The peak X-ray and SZ emissions are consistent with each other and the AMI SZ decrement shows some signs of being extended towards the SW (Fig. 3 B and C); there are no contaminating sources in the vicinity of this SZ-‘tail’.

The SZ effect from Abell 586 has previously been observed with OVRO/BIMA by LaRoque et al. (2006) and Bonamente et al. (2006). LaRoque et al. apply an isothermal  $\beta$ -model to SZ and CHANDRA X-ray observations and find  $M_g(r_{2500}) = 2.49 \pm 0.32 \times 10^{13} M_\odot$  and  $M_g(r_{2500}) = 2.26^{+0.13}_{-0.11} \times 10^{13} M_\odot$ , respectively (using  $h_{70} = 1$  and excising the inner 100 kpc from the X-ray data). In addition, they determine an X-ray spectroscopic temperature of the cluster gas of  $\approx 6.35$  keV between a radius of 100 kpc and  $r_{2500}$ . In comparison, Okabe et al. (2010) use *Subaru* to calculate the cluster mass from weak lensing by applying a Navarro, Frenk & White (NFW; Navarro, Frenk, & White 1996) profile. They find  $M_T(r_{2500}) = 2.41^{+0.45}_{-0.41} \times 10^{14} M_\odot$  and  $M_T(r_{500}) = 4.74^{+1.40}_{-1.14} \times 10^{14} M_\odot$  (using  $h_{72} = 1$ ). In this work, we find  $M_T(r_{500}) = 3.0 \pm 1.3 \times 10^{14} M_\odot$ , where  $r_{500} = 0.94 \pm 0.14$  Mpc and  $h_{70} = 1$ . Note that the fluxes of the radio sources  $S_1$  and  $S_5$  are degenerate in our analysis of Abell 586 (see Fig. 4); this is because these sources are separated by only  $66''$  and their individual fluxes cannot be disentangled in the analysis of the AMI SA data.

## 6.3 Abell 611

Results for Abell 621 are presented in Fig. 5. Our methodology is able to model the radio sources + cluster environment well, as demonstrated by the good constraints on the mass and other parameters and the lack of degeneracies between the sources closest to the cluster and the cluster mass (Fig. 5 D, E and F). We do not expect any significant contamination from radio sources nor from extended emission since GMRT observations by Venturi et al. (2008) found no evidence for a radio halo associ-

## Abell 586

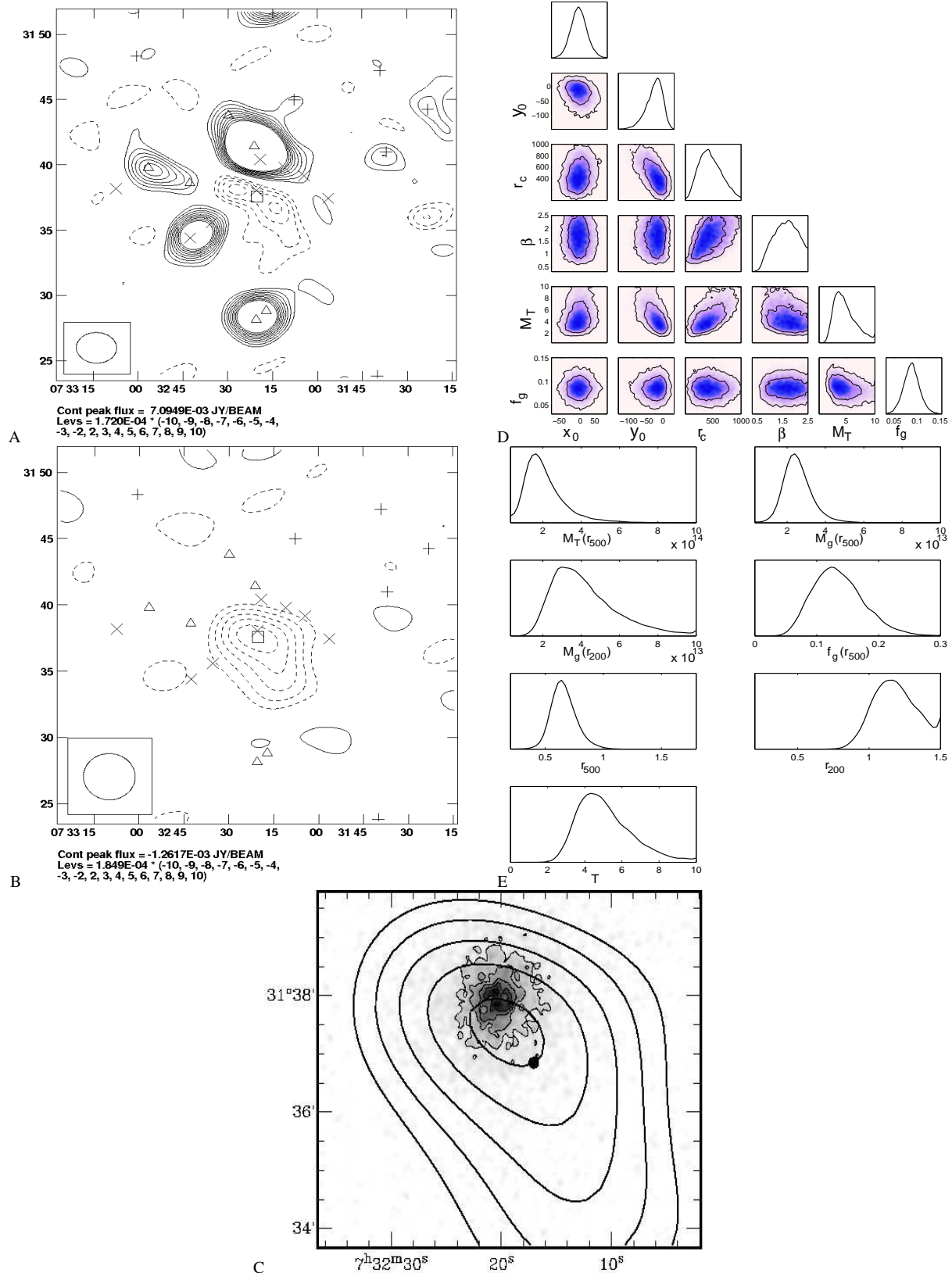


**Figure 3.** Results for Abell 586. Panels A and B show the SA map before and after source subtraction, respectively; a  $0.6\text{ k}\lambda$  taper has been applied in B. The box in panels A and B indicates the cluster SZ centroid, for the other symbols see Tab. 4. Panel C shows the smoothed CHANDRA X-ray map overlaid with contours from B. D and E show the marginalized posterior distributions for the cluster sampling and derived parameters, respectively. The y-axis for the 1-d marginals is the probability density and for all the posterior distributions plots in this paper  $h$  refers to  $h_{100}$ . In D  $M_T$  is given in units of  $h_{100}^{-1} \times 10^{14} M_{\odot}$  and  $f_g$  in  $h_{100}^{-1}$ ; both parameters are estimated within  $r_{200}$ . In E  $M_g$  is in units of  $h_{100}^{-2} M_{\odot}$ ,  $r$  in  $h_{100}^{-1}$  Mpc and  $T$  in KeV. The slight rise in the distribution for  $r_{200}$  at large  $r$  is a result of a binning artifact and, in fact, this distribution does tail off smoothly, as expected.



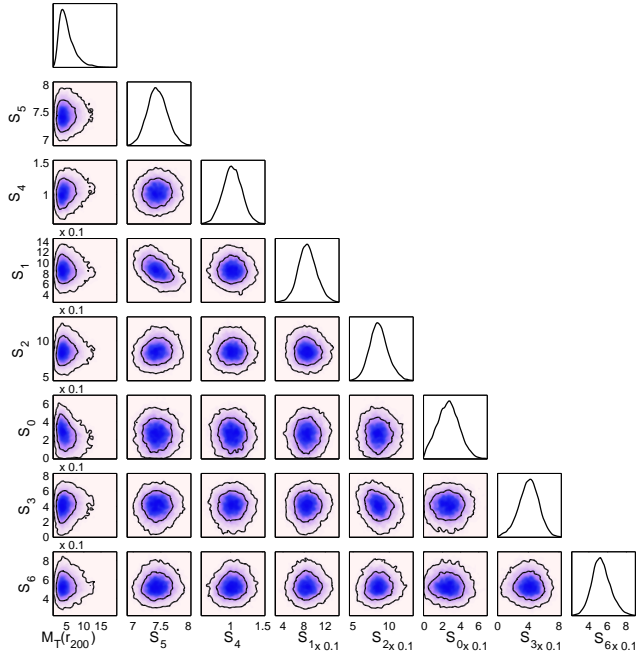


**Figure 4.** 1 and 2-D marginalized posterior distributions for the flux densities, in Jys, of sources detected within  $5'$  of the SZ centroid of Abell 586 (see Tab. 5) and  $M_T(r_{200})$ , in units of  $h_{100}^{-1} M_\odot \times 10^{14}$ .

ated with Abell 611 at 610 MHz. The decrement on the source-subtracted maps appears to be circular, in agreement with the X-ray surface brightness from the CHANDRA archive data shown in Fig. 5 C, which also appears to be smooth and whose peak is close to the position of the brightest cluster galaxy and the SZ peak. These facts might be taken to imply the cluster is relaxed but, it does not seem to have a cool core (Marrone et al. 2011). Abell 611 has also previously been observed in the SZ at 15 GHz by Grainger et al. (2002), AMI Consortium: Zwart et al. (2010) and AMI Consortium: Hurley-Walker et al. (2011), and at 30 GHz by Bonamente et al. (2004), Bonamente et al. (2006) and LaRoque et al. (2006).

From the analysis in Donnarumma et al. (2010) the cluster mass was estimated to be  $9.32\text{--}11.11 \times 10^{14} M_\odot$  (within a radius of  $1.8 \pm 0.5$  Mpc) by fitting different cluster models to X-ray data and between  $4.01\text{--}6.32 \times 10^{14} M_\odot$  (within a radius of  $1.5 \pm 0.2$  Mpc) when fitting different models to the lensing data; all estimates use  $h_{70} = 1$ . Several other analyses of CHANDRA data produce comparable mass estimates (e.g., Schmidt & Allen 2007, Morandi, Ettori & Moscardini 2007, Morandi & Ettori 2007 and Sanderson et al. 2009). Romano et al. (2010) perform a weak-lensing analysis of Abell 611 using data from the Large Binocular Telescope; with an NFW profile they estimate  $M_T(r_{200}) = 4\text{--}7 \times 10^{14} M_\odot$  for  $h_{70} = 1$ .

These are in agreement with the values obtained from *Subaru* weak lensing observations by Okabe et al.. AMI Consortium: Hurley-Walker et al. estimate the total mass for this system within  $r_{200}$ . Using lensing data they find it is  $4.7 \pm 1.2 \times 10^{14} h_{70}^{-1} M_\odot$  and using AMI SZ data they find it is  $6.0 \pm 1.9 \times 10^{14} h_{70}^{-1} M_\odot$ . We find  $M_T(r_{200}) = 5.7 \pm 1.1 \times 10^{14} M_\odot$ , where  $r_{200} = 1.6 \pm 0.1$  and  $h_{70} = 1$ ; this value is significantly smaller than the result given in AMI Consortium: Zwart et al. (2010); this is due to their mass measurements being biased high, as they said, and is further discussed in AMI Consortium: Olamaie et al. (2011).

#### 6.4 Abell 621

Fig. 6 contains our results for Abell 621. Out of the 13 radio sources detected on the LA raster for Abell 621, three lie near the edge of the cluster decrement in the source-subtracted map and one, which has a flux density  $\approx 7$  mJy, is coincident with the best-fit cluster position, as indicated by the box in Fig. 6 A. However, whatever reasonable source subtraction we try makes almost no difference to the inferred cluster mass. The *ROSAT HRI* X-ray image presented in Fig. 6 C appears to be quite uniform and circular and the offset between the X-ray and SZ cluster centroids is small. We find the cluster mass to be  $M_T(r_{200}) = 4.8_{-1.8}^{+1.7} \times 10^{14} h_{100}^{-1} M_\odot$  from our analysis; at  $6\sigma$ , this is one of our less significant detections.

The data for the probability distributions in Fig. 6 E have been binned relatively finely to avoid misleading features, in particular towards the lower limits of our plots. As a result, the noise in these bins is higher, which makes the distributions appear less smooth. For some combinations of cluster parameters, there is nowhere in the cluster density estimation that the density of the gas reaches  $500\rho_{\text{crit}}$ . In these cases, where there is no physical solution for  $r_{500}$ , we set  $r_{500} = 0$ . This leads to sharp, meaningless peaks at small radius in the distributions for some cluster parameters at  $r_{500}$  (Fig. 6 E). These features have also been discussed in AMI Consortium: Zwart et al. (2010).

#### 6.5 Abell 773

Results for Abell 773 are shown in Fig. 7. Abell 773 has few associated radio sources, all of which are  $\geq 10'$  away from the pointing centre, weak ( $\lesssim 3$  mJy), and are subtracted well from our data (Fig. 7 B). We do not find any evidence for extended positive emission in our maps. Observations by Giovannini, Tordi, & Feretti (1999) revealed the presence of a radio halo with a luminosity of  $2.8 \times 10^{24}$  WHz $^{-1}$  at 1.4 GHz; this result has been confirmed with the VLA by Govoni et al. (2001). Given the typical steep spectral index of radio halos, we do not expect our SZ signal to be affected at 16 GHz.

Our observations clearly show the SZ image is extended along the NW-SE direction, contrary to the X-ray image from CHANDRA observations, which appears to be elongated in an approximately perpendicular direction. As might be expected from a disturbed system, Abell 773 appears to not have a cool core (Allen & Fabian 1998).

Barrena et al. (2007) present a comprehensive study of Abell 773 from the Telescopio Nazionale Galileo (TNG) telescope and X-ray data from the CHANDRA data archive. They find two peaks in the velocity distribution of the cluster members which are separated by  $2'$  along the E-W direction. Two peaks can also be seen in the X-ray, although these are along the NE-SW direction. Barrena et al. estimate the virial mass of the main cluster to be  $M_T(r_{\text{vir}}) = 1.0\text{--}2.5 \times 10^{15} h_{70}^{-1} M_\odot$  and  $M_T = 1.2\text{--}2.7 \times 10^{15} h_{70}^{-1} M_\odot$  for the entire system, using the virial theorem, dispersion velocity measurements and a galaxy King-like distribution. Assuming an NFW profile they estimate the mass for the system to be  $M_T(< r = 1h_{70}^{-1} \text{Mpc}) = 5.9\text{--}11.1 \times 10^{14} h_{70}^{-1} M_\odot$ . A further analysis of CHANDRA data by Govoni et al. (2004) yielded a mean temperature of  $7.5 \pm 0.8$  keV within a radius of 800 kpc ( $h_{70} = 1$ ). Another X-ray study of this cluster by Zhang et al. (2008) using XMM-NEWTON found  $M_T(r_{500}) = 8.3 \pm 2.5 \times 10^{14} M_\odot$  assuming isothermality, spherical symmetry and  $h_{70} = 1$ .

The SZ effect associated with Abell 773 has been observed several times (Grainge et al. 1993, Carlstrom et al. 1992,

## A611

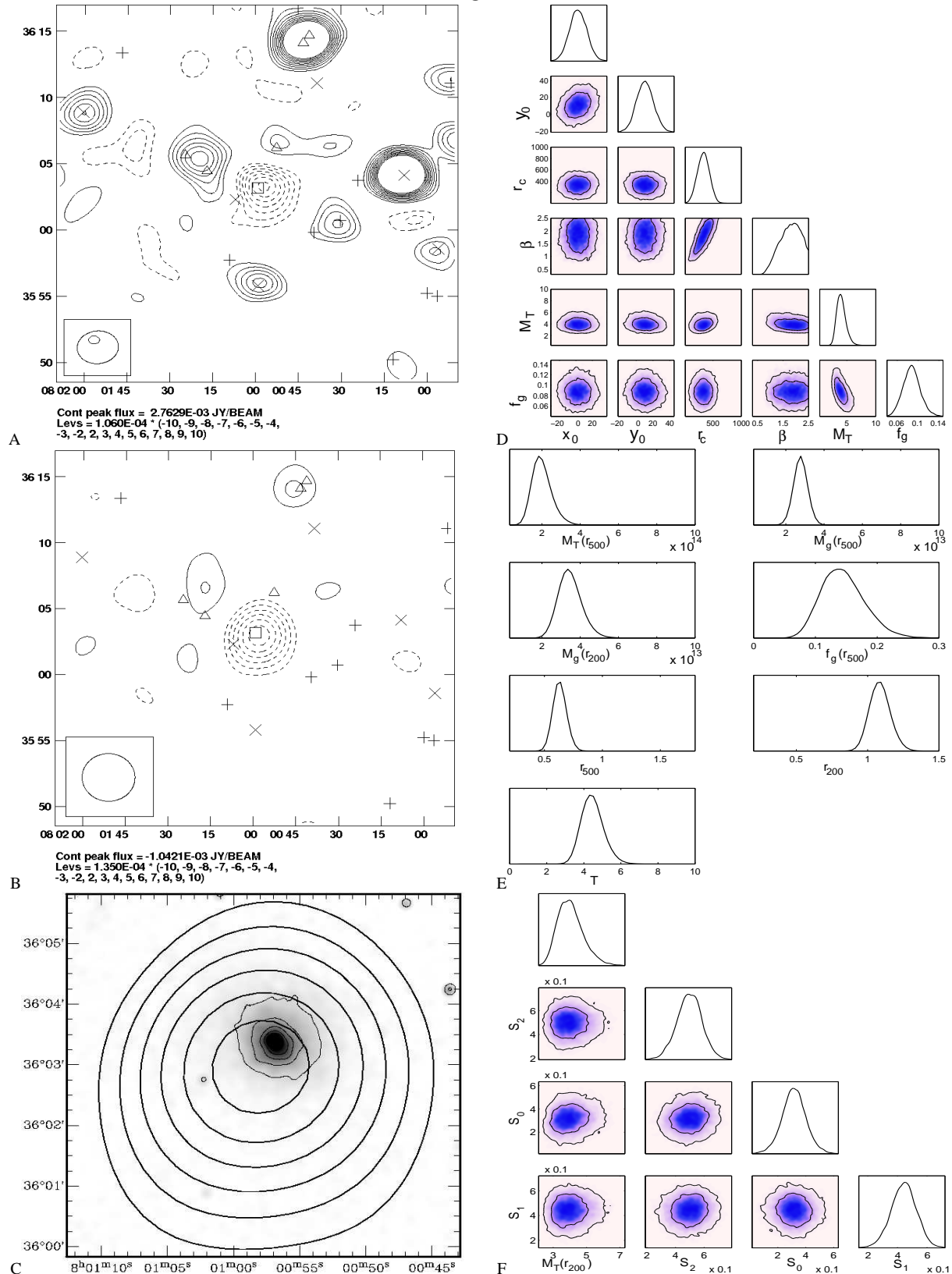


**Figure 5.** Results for Abell 611. Panels A and B show the SA map before and after source subtraction, respectively; a  $0.6\text{ k}\lambda$  taper has been applied to B. The box in panels A and B indicates the cluster SZ centroid, for the other symbols see Tab. 4. C shows the smoothed CHANDRA X-ray map overlaid with contours from B. Panels D and E show the marginalized posterior distributions for the cluster sampling and derived parameters, respectively. F shows the 1 and 2-D marginalized posterior distributions for source flux densities, in Jys, (within  $5'$  of the cluster SZ centroid, see Tab. 5) and  $M_T(r_{200})$ , in  $h_{100}^{-1} \times 10^{14} M_\odot$ . In panel D  $M_T$  is given in units of  $h_{100}^{-1} \times 10^{14} M_\odot$  and  $f_g$  in  $h_{100}^{-1}$ ; both parameters are estimated within  $r_{200}$ . In E  $M_g$  is in units of  $h_{100}^{-2} M_\odot$ ,  $r$  in  $h_{100}^{-1} \text{ Mpc}$  and  $T$  in KeV.

## Abell 621

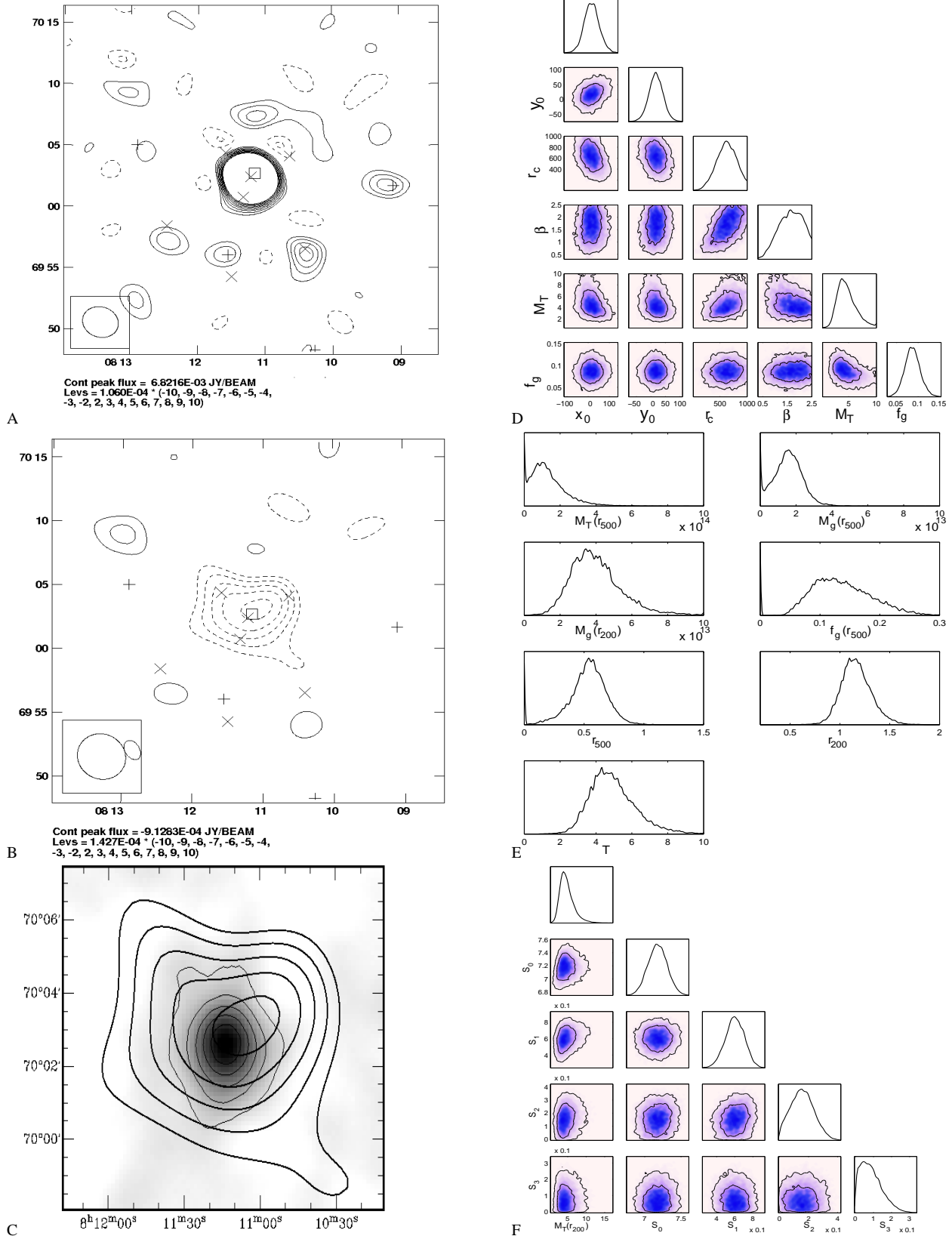


**Figure 6.** Results for Abell 621. Panels A and B show the SA map before and after source-subtraction, respectively; a  $0.6\text{ kJ}$  taper has been applied to B. The box in panels A and B indicates the cluster SZ centroid, the other symbols are in Tab. 4. The smoothed *ROSAT HRI* X-ray map overlaid with contours from B is given in panel C. Panels D and E show the marginalized posterior distributions for the cluster sampling and derived parameters, respectively. F shows the 1 and 2-D marginalized posterior distributions for source flux densities (in Jys) within  $5'$  of the cluster SZ centroid (see Tab. 5) and  $M_T(r_{200})$  in  $h_{100}^{-1} \times 10^{14} M_\odot$ . In D  $M_T$  is given in units of  $h_{100}^{-1} \times 10^{14} M_\odot$  and  $f_g$  in  $h_{100}^{-1}$ ; both parameters are estimated within  $r_{200}$ . In E  $M_g$  is in units of  $h_{100}^{-2} M_\odot$ ,  $r$  in  $h_{100}^{-1} \text{ Mpc}$  and  $T$  in KeV.

Saunders et al. 2003, Bonamente et al. 2006, LaRoque et al. 2006). Most recently, AMI Consortium: Zwart et al. (2010) observed the cluster and found a cluster mass of  $M_T(r_{200}) = 1.9^{+0.3}_{-0.4} \times 10^{15} M_\odot$  using  $h_{100} = 1$ ; however, their  $M_T$  estimates are biased high, as they say, and we find  $M_T(r_{200}) = 3.6 \pm 1.2 \times 10^{14} h_{100} M_\odot$ .

### 6.6 Abell 781

Fig. 8 contains our results for Abell 781. It is evident from inspection of Figs. 8 A and F and Tab. 5 that there is strong emission from radio sources lying on the decrement. One of the sources with a flux density of 9 mJy lies on top of the McADAM best-fit cluster position. The difficulty of accurately disentangling the signal contributions from this source and the cluster is translated into a degeneracy between the source's flux density and the cluster mass: Fig. 8 F. No extended emission was detected on the LA maps and, after source subtraction, the residuals on the maps are  $\leq 2\sigma$  (Fig. 8 B). Rudnick & Lemmerman (2009) have found evidence in WENSS data at 327 MHz of diffuse emission from a radio galaxy and some other unknown source with a flux within a radius of 500 kpc of 40 mJy, while Venturi et al. (2008) estimate diffuse emission at the centre to be  $\approx 15 - 20$  mJy using 325-MHz GMRT data. Assuming a typical steep spectral index for radio halos, in the range of 1.2 – 1.4 (e.g., Hanisch 1980), even as far as 16 GHz, we would expect to find an  $\approx 170 \mu\text{Jy}$  signal around the cluster and  $\leq 85 \mu\text{Jy}$  at the centre. The GMRT contour map in Venturi et al. identifies the relic at a similar location to that of some unsubtracted positive emission in our maps at  $\approx$  RA 09:30:00, Dec 30:28:00.

X-ray observations with CHANDRA and XMM-NEWTON (Sehgal et al. 2008) imply that Abell 781 is a complex cluster merger: the main cluster is surrounded by three smaller clusters, two to the East of the main cluster and one to the West. Sehgal et al. estimate the mass of Abell 781 within  $r_{500}$  assuming a NFW matter density profile to be  $5.2^{+0.3}_{-0.7} \times 10^{14} M_\odot$  from X-ray data and  $2.7^{+1.0}_{-0.9} \times 10^{14} M_\odot$  from the Kitt Peak Mayall 4-m telescope lensing observations, using  $h_{71} = 1$ . Further results from XMM-NEWTON by Zhang et al. yield  $M_T(r_{500}) = 4.5 \pm 1.3 \times 10^{14} M_\odot$  assuming isothermality, spherical symmetry and  $h_{70} = 1$ . We obtain  $M_T(r_{500}) = 2.9 \pm 0.6 \times 10^{14} M_\odot$  and  $M_T(r_{200}) = 5.9 \pm 1.1 \times 10^{14} M_\odot$  for  $h_{70} = 1$ .

### 6.7 Abell 990

Results for Abell 990 are given in Fig. 9. We detected 20 sources towards Abell 990. Those detected above  $4\sigma_{\text{LA}}$  within  $10'$  from the pointing centre were found to have flux densities  $< 2.8$  mJy, not to be extended with respect to the LA synthesized beam (Tab. 5), and none to lie on the SZ decrement, as seen in the source-subtracted map (Fig. 9 B). The subtraction has worked well and there are only low-level ( $\approx 1 - 2\sigma$ ) residuals. Rudnick & Lemmerman (2009) do not detect any significant amount of diffuse emission within a radius of 500 kpc in 327 MHz WENSS data; given the steep falling spectrum associated with this emission, we do not expect it to contaminate our SZ signal. The imaged decrement is fairly circular but extended along the NE-SW direction coincident with the distribution of the X-ray signal. Our spherical cluster model provides a good fit and the parameter distributions are tightly constrained. The low resolution X-ray map shown in Fig. 9 C provides tentative evidence that the X-ray emitting cluster gas has a clumpy distribution.

### 6.8 Abell 1413

In Fig. 10 we present results for Abell 1413. It can be seen from Figs. 10 A and B that there are two of sources on the decrement with flux densities of 0.47 and 3.1 mJy (in Tab. 5). The brightest source in our LA maps has a flux density of 14 mJy but, since it is  $700''$  from the cluster X-ray centre, it does not contaminate our SZ signal. Some residual flux is seen on the source-subtracted SA maps; the strongest residuals are not associated with sources in the LA data, suggesting they could be extended emission resolved out from the LA maps. Govoni et al. (2009) find tentative ( $\approx 3\sigma$ ) evidence in FIRST data at 1.4 GHz for a weak mini halo with a luminosity of  $1.0 \times 10^{23} \text{ W Hz}^{-1}$ . The peak signal from this mini halo is offset to the East with respect to the central cD galaxy, similarly to our SZ peak, which is slightly offset to the SE of the X-ray centroid. Abell 1413 does seem to be a relaxed cluster; this is supported by the smooth X-ray distribution, the good agreement between the X-ray and SZ centroids, the circular appearance of the projected SZ signal and the presence of a cool core (Allen & Fabian 1998). We therefore expect our model to provide a good fit to the AMI data towards this cluster.

Abell 1413 has been observed in the X-ray by XMM-NEWTON (e.g., Pratt & Arnaud 2005), CHANDRA (e.g., Vikhlinin et al. 2005 and Bonamente et al. 2006) and most recently by the SUZAKU satellite (Hoshino et al. 2010); SZ images have been made with the Ryle Telescope at 15 GHz (Grainge et al. 1996) and with OVRO/BIMA at 30 GHz (LaRoque et al. and Bonamente et al. 2006). These analyses indicate that Abell 1413 seems indeed to be a relaxed cluster with no evidence of recent merging. Different temperature and density profiles obtained from X-ray data are in good agreement out to half the virial radius. Hoshino et al. measure the variation of temperature with radius, finding a temperature of 7.5 keV near the centre and of 3.5 keV at  $r_{200}$ ; they assume spherical symmetry, an NFW density profile and hydrostatic equilibrium to calculate  $M_T(r_{200}) = 6.6 \pm 2.3 \times 10^{14} h_{70}^{-1} M_\odot$ . Zhang et al. use XMM-NEWTON and find  $M_T(r_{500}) = 5.4 \pm 1.6 \times 10^{14} M_\odot$ ; they assume isothermality, spherical symmetry and  $h_{70} = 1$ . We determine  $M_T(r_{200})$  to be  $5.7 \pm 1.4 \times 10^{14} M_\odot$  for  $h_{70} = 1$ .

### 6.9 Abell 1423

Results for Abell 1423 are shown in Fig. 11. The source environment for Abell 1423 is challenging (see Fig. 11 A) – 23 sources have been detected within  $10'$  of the X-ray cluster centroid, of which 4 lie on the decrement, as seen from the source-subtracted map. We find no evidence for extended emission, in agreement with the lack of diffuse emission towards this cluster at 327 MHz reported by Rudnick & Lemmerman (2009) and the results in Rossetti et al. (2011). The sources closest to the cluster all have flux densities  $< 1.3$  mJy (Tab. 5) and only small positive residuals remain after source subtraction. As shown in Fig. 11 F, the flux densities for some of the sources close to the cluster centroid manifest degeneracies with the cluster mass.

The details on the dynamics of Abell 1423 are largely unknown. The lack of strong radio halo emission is indicative of a system without very significant dynamical activity (Buote 2001), as is the good agreement between the X-ray and SZ emission peak positions. On the other hand, the X-ray data in Fig. 11 C shows signs of substructure and our SZ image is be elongated along the SE–NW direction. Sanderson et al. (2009) find that the logarithmic gradient for the gas density profile of Abell 1423 at  $0.04 r_{500}$  is  $\alpha \approx -0.98$  – a key signature of cooling core clusters (Vikhlinin et al. (2006) sug-

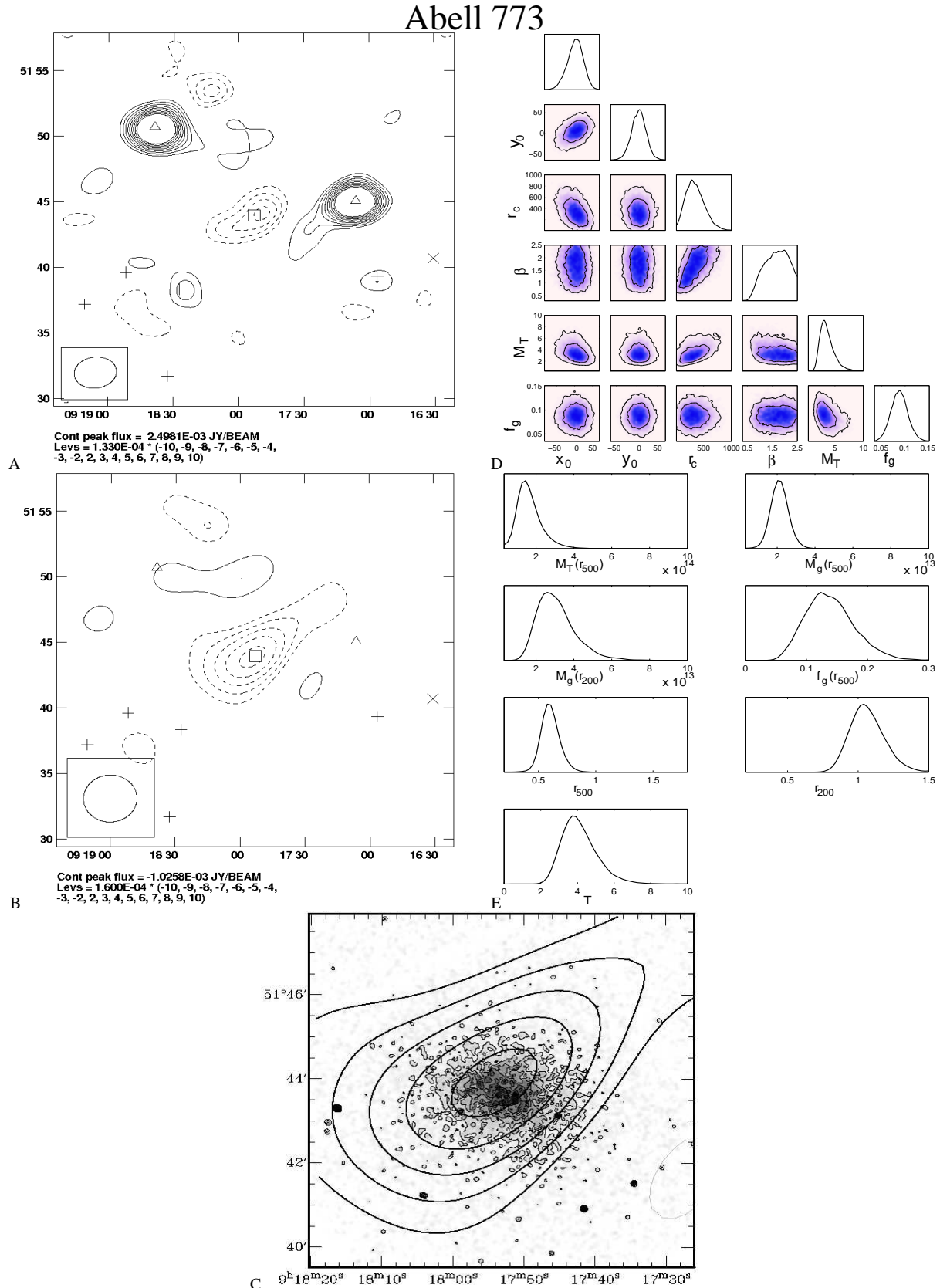


**Figure 7.** Results for Abell 773. Panels A and B show the SA map before and after source subtraction, respectively; a  $0.6\text{ k}\lambda$  taper has been applied to B. The box in panels A and B indicates the cluster SZ centroid, for the other symbols see Tab. 4. The smoothed CHANDRA X-ray map overlaid with contours from B is given in image C. Panels D and E show the marginalized posterior distributions for the cluster sampling and derived parameters, respectively. In panel D  $M_T$  is given in units of  $h_{100}^{-1} \times 10^{14} M_{\odot}$  and  $f_g$  in  $h_{100}^{-1}$ ; both parameters are estimated within  $r_{200}$ . In E  $M_g$  is in units of  $h_{100}^{-2} M_{\odot}$ ,  $r$  in  $h_{100}^{-1} \text{Mpc}$  and  $T$  in KeV. No plots of the degeneracy between cluster mass and source flux densities are shown since all detected sources are  $> 5'$  from the cluster SZ centroid and thus should not have a strong impact on the marginalized distribution for the cluster mass.



A781

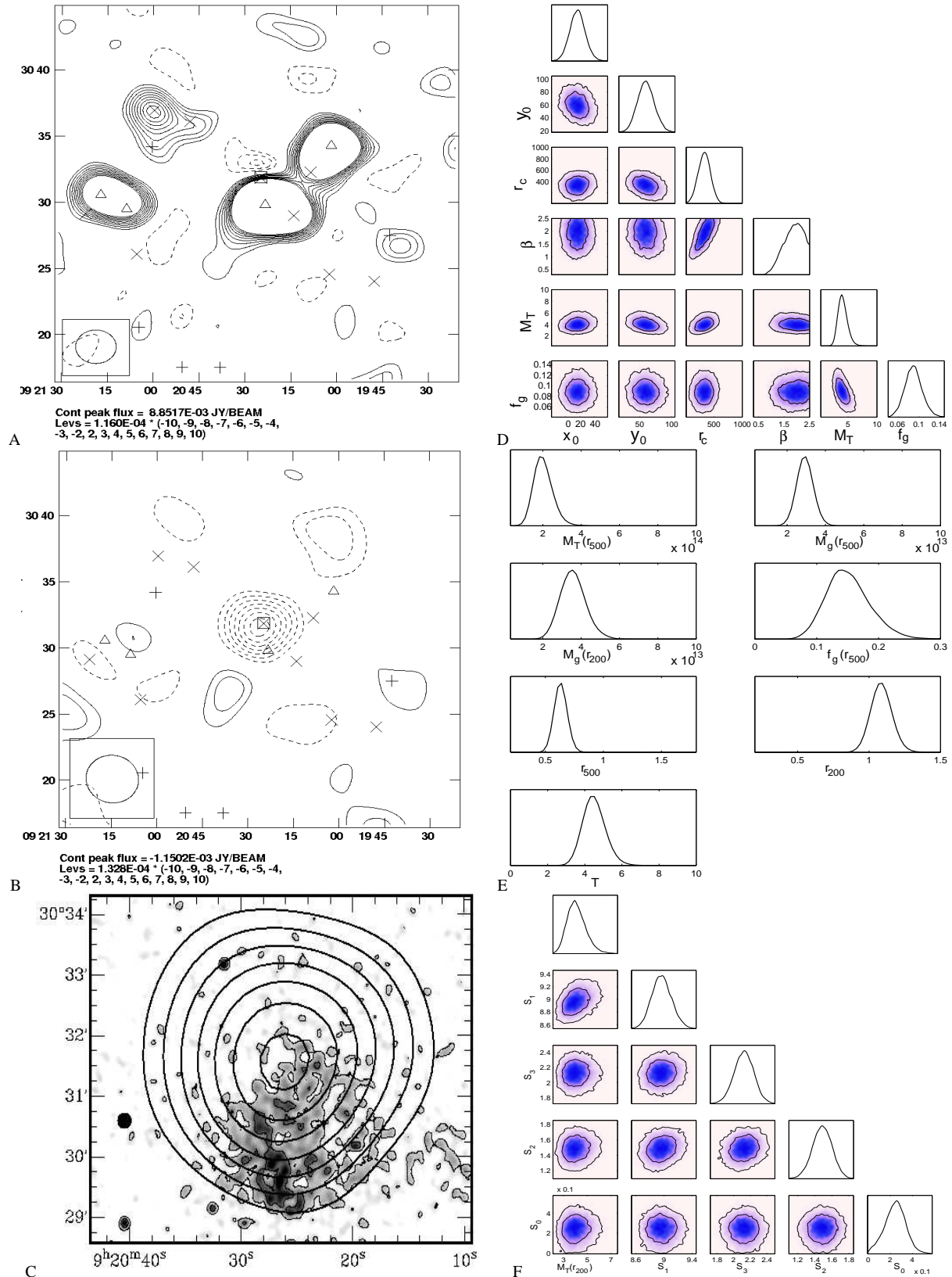


**Figure 8.** Results for Abell 781. Panels A and B show the SA map before and after source-subtraction, respectively; a  $0.6\text{ k}\text{\AA}$  taper has been applied to B. The box in panels A and B indicates the cluster SZ centroid, other symbols are in Tab. 4. The smoothed CHANDRA X-ray map overlaid with contours from B is given in image C. Panels D and E show the marginalized posterior distributions for the cluster sampling and derived parameters, respectively. F shows the 1 and 2-D marginalized posterior distributions for source flux densities (in Jys) within  $5'$  of the cluster SZ centroid (see Tab. 5) and  $M_T(r_{200})$  (in  $h_{100}^{-1} \times 10^{14} M_\odot$ ). In D  $M_T$  is given in units of  $h_{100}^{-1} \times 10^{14} M_\odot$  and  $f_g$  in  $h_{100}^{-1}$ ; both parameters are estimated within  $r_{200}$ . In E  $M_g$  is in units of  $h_{100}^{-2} M_\odot$ ,  $r$  in  $h_{100}^{-1} \text{ Mpc}$  and  $T$  in KeV.

## Abell 990

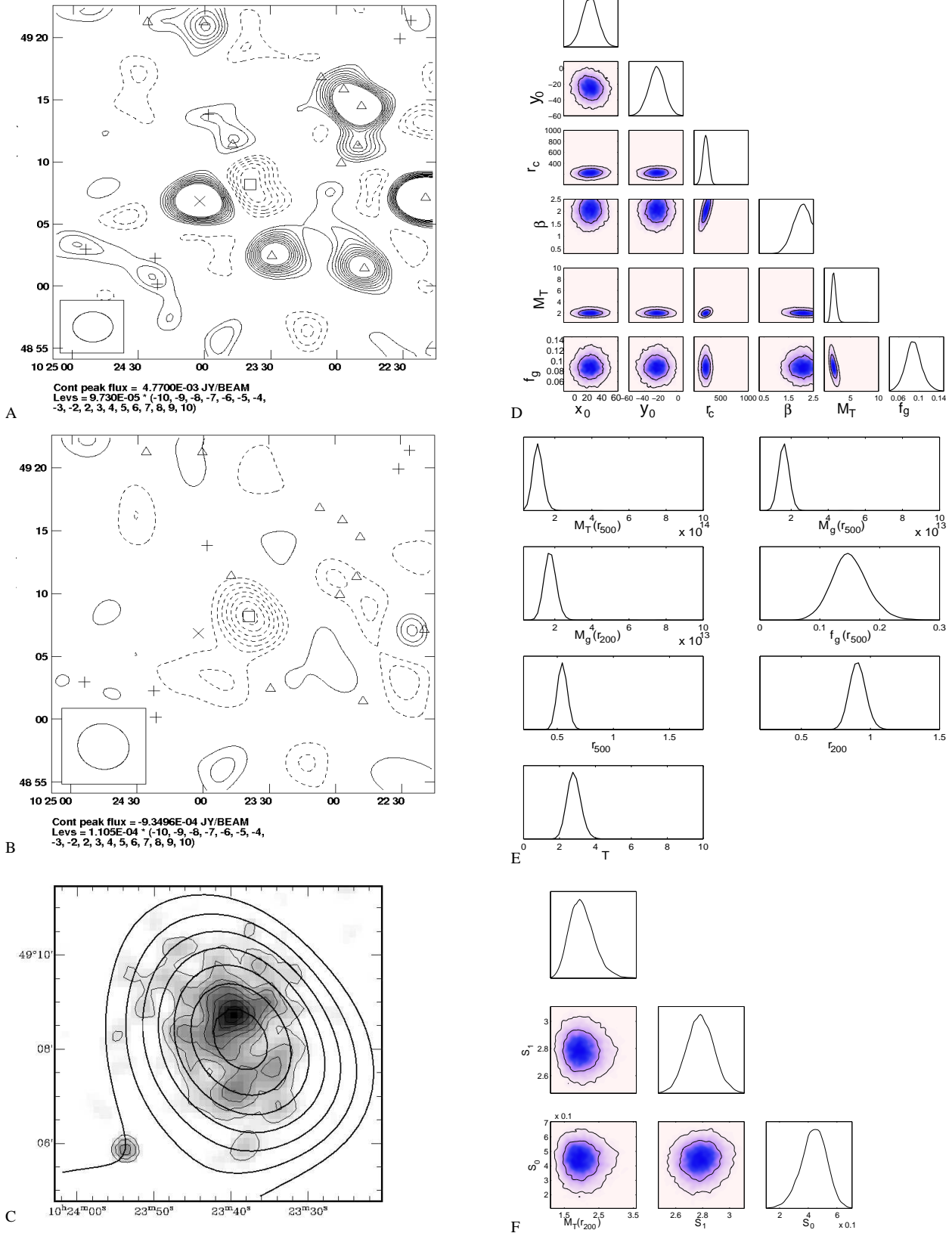


**Figure 9.** Results for Abell 990. Panels A and B show the SA map before and after source-subtraction, respectively; a 0.6 k $\lambda$  taper has been applied to B. The box in panels A and B indicates the cluster SZ centroid, for the other symbols see Tab. 4. The smoothed *ROSAT HRI* X-ray map overlaid with contours from B is shown in image C. Panels D and E show the marginalized posterior distributions for the cluster sampling and derived parameters, respectively. F shows the 1 and 2-D marginalized posterior distributions for source flux densities in Jy (see Tab. 5) and  $M_T(r_{200})$  (in  $\times 10^{14} M_\odot$ ). In panel D  $M_T$  is given in units of  $h_{100}^{-1} \times 10^{14} M_\odot$  and  $f_g$  in  $h_{100}^{-1}$ ; both parameters are estimated within  $r_{200}$ . In E  $M_g$  is in units of  $h_{100}^{-2} M_\odot$ ,  $r$  in  $h_{100}^{-1}$  Mpc and  $T$  in KeV.

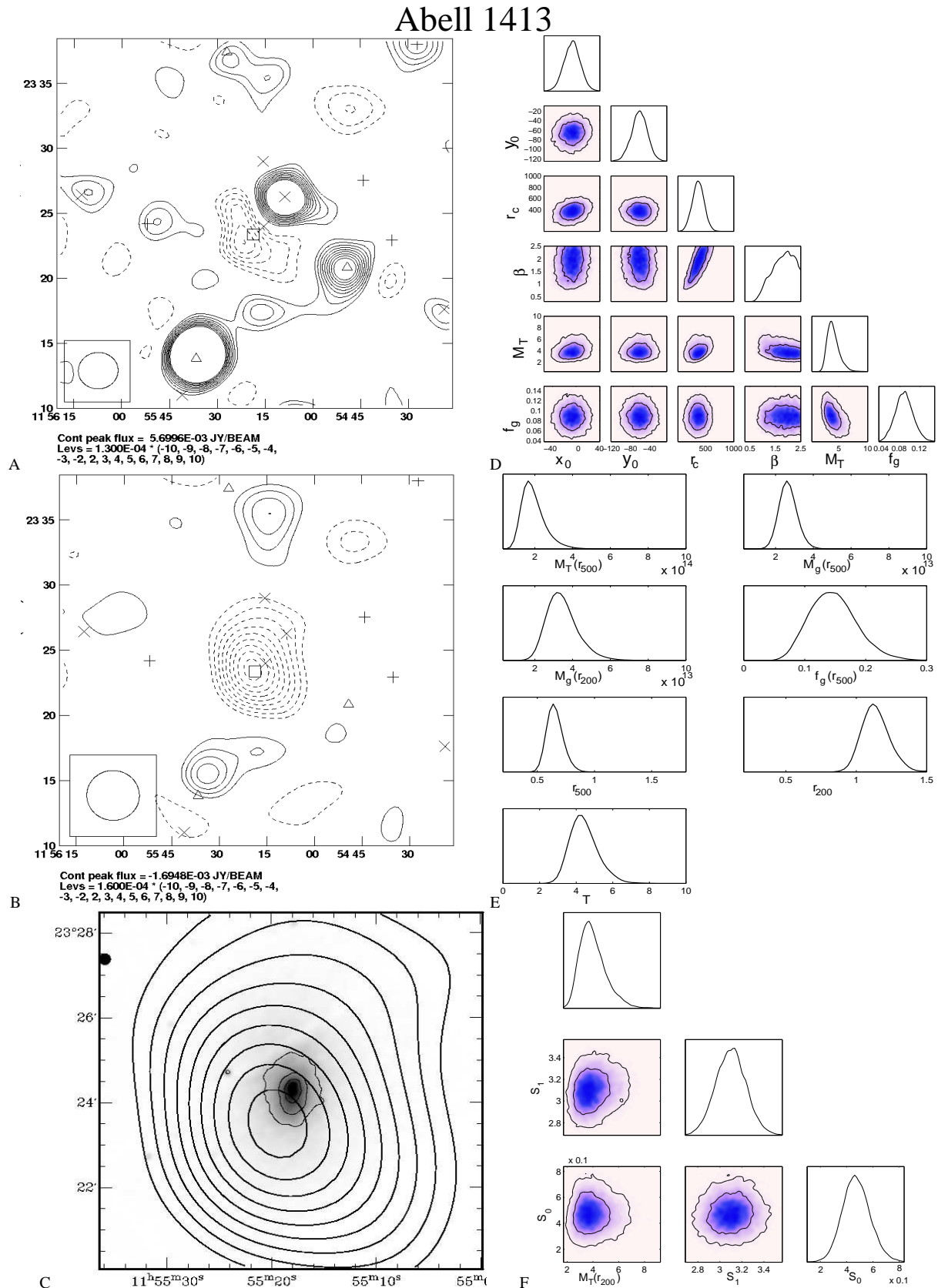


**Figure 10.** Results for Abell 1413. Panels A and B show the SA map before and after source-subtraction, respectively; a  $0.6k\lambda$  taper has been applied to B. The box in panels A and B indicates the cluster SZ centroid, for the other symbols see Tab. 4. The smoothed CHANDRA X-ray map overlaid with contours from B in presented in image C. Panels D and E show the marginalized posterior distributions for the cluster sampling and derived parameters, respectively. F shows the 1 and 2-D marginalized posterior distributions for source flux densities (in Jys) within  $5'$  of the cluster SZ centroid (see Tab. 5) and  $M_T(r_{200})$  (in  $h_{100}^{-1} \times 10^{14} M_\odot$ ). In panel D  $M_T$  is given in units of  $h_{100}^{-1} \times 10^{14} M_\odot$  and  $f_g$  in  $h_{100}^{-1}$ ; both parameters are estimated within  $r_{200}$ . In E  $M_g$  is in units of  $h_{100}^{-2} M_\odot$ ,  $r$  in  $h_{100}^{-1} \text{Mpc}$  and  $T$  in KeV.



gest  $\alpha < -0.7$  for strong cooling flows). In their study clusters with small offsets at  $r_{500}$  between the X-ray and the Brightest Cluster Galaxy (BCG) are tightly correlated with large, negative spectral indices, an indication that the strength of cooling cores tends to drop in more disturbed systems, but Abell 1423 is an unusual outlier in this trend with a small offset and a steep  $\alpha$ .

### 6.10 Abell 1704

Abell 1704 has been observed with *ROSAT HRI* and *PSPC* (Rizza et al. 1998). These observations show a shift in position between the peak emission and the cluster centroid and distinct signs of elongations in the gas distribution. Further analysis of X-ray observations suggest the presence of a cooling flow (Allen & Fabian 1998). Carlstrom et al. (1992) attempted to detect an SZ effect using the OVRO array at 30 GHz towards this cluster but found no convincing SZ signal.

The NVSS map at 1.4 GHz shows complex, extended emission (Fig. 12). These features are detected on our SA maps but a significant portion of the emission is resolved out on our LA maps (see Tab. 5 for more details on these sources). Our model is not sophisticated enough to deal properly with extended structure and significant residual emission can be seen in the source-subtracted SA map, Fig. 12. Consequently, we are not able to convincingly detect an SZ effect towards Abell 1704.

### 6.11 Abell 1758

Results for Abell1758a and b are given in Fig. 13-Fig 15. It is clear from Fig. 13 A, B and C that Abell 1758 is a complex system comprising two gravitationally-bound main clusters, Abell 1758a and Abell 1758b, separated by 8' (Rizza et al. 1998 and David & Kempner 2004). David & Kempner find no conclusive evidence for interaction between these two main clusters, yet each of them is undergoing major mergers – Abell 1758a between two 7-keV clusters and Abell 1758b between two 5-keV clusters; since both sets of mergers are between clusters of approximately equal mass, provided each of the primary clusters was virialized pre-merger, we might expect the average temperature to be higher by some 25% when all the gas mass of the subcluster has merged with that of the primary cluster.

To map the full extent of this system we took raster observations with the SA, which are presented in Fig. 13 B and C. From 13 Cii it can be seen that the SZ signal follows the X-ray emission but there seems to be a hint of an SZ signal connecting these two clusters; note that the clusters have identical redshifts. No connecting X-ray signal would be expected and indeed none is seen. A recent analysis of Spitzer/MIPS 24 $\mu$ m data by Haines et al. (2009) classifies Abell 1758 as the most active system they have observed at that wavelength. They also identify numerous smaller mass peaks and filamentary structures, which are likely to indicate the presence of infalling galaxy groups, in support of the David & Kempner observations.

For Abell 1758a we obtain  $M_T(r_{500}) = 2.5 \pm 0.4 \times 10^{14} h_{100} M_\odot$  and  $M_T(r_{200}) = 4.1_{0.8}^{0.7} \times 10^{14} h_{100} M_\odot$ . Zhang et al. studied Abell 1758a using XMM-Newton and found  $M_T(r_{500}) = 1.1 \pm 0.3 \times 10^{15} M_\odot$ ; they assumed isothermality, spherical symmetry and  $h_{70} = 1$ .

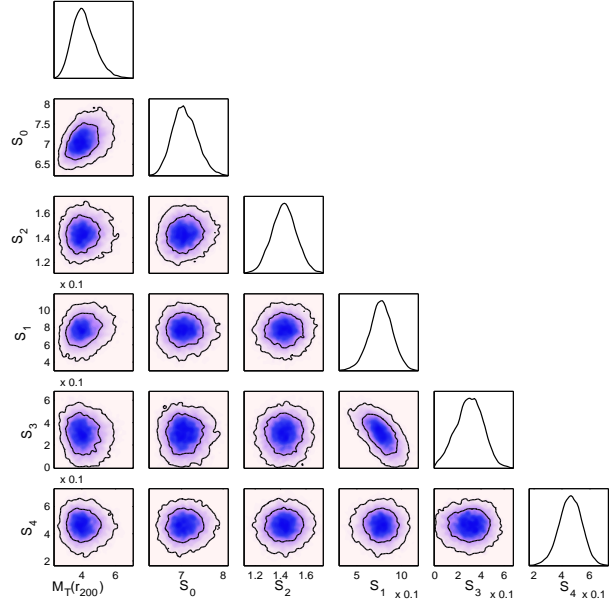


**Figure 15.** 1 and 2-D marginalized posterior distributions for  $M_T(r_{200})$  and sources within 5' from the cluster X-ray centroid for Abell 1758a. Source flux densities are given in units of Jys and  $M_T(r_{200})$  in units of  $h_{100}^{-1} M_\odot \times 10^{14}$ .

### 6.12 Abell 2009

Results for Abell 2009 are given in Fig. 16. Eighteen sources were detected above  $4\sigma_{LA}$  in our LA maps. Given that all of the sources, except one, are further away than one arcminute from the pointing centre and have flux densities  $< 2$  mJy, the source environment should not significantly contaminate the SZ signal on the SA maps. The source-subtraction has worked well and there are only  $2\sigma$  residuals (Fig. 16, B); the most prominent residual is likely to be associated with some extended emission seen in the SA map before source subtraction.

We find the SZ image is extended in an approximately NS direction. Okabe et al. (2010) fit an NFW profile to weak lensing data from the *Subaru/Suprime-Cam* and find  $M_T(r_{110}) = 3.86_{-0.93}^{+1.20} \times 10^{14} h_{72}^{-1} M_\odot$  (with  $h_{72} = 1.0$ ). We find  $M_T(r_{200}) = 4.6 \pm 1.5 \times 10^{14} h_{100}^{-1} M_\odot$ .

The misleading sharp peaks at small radius in the distributions for cluster parameters at  $r_{500}$  (Fig. 16 F) are discussed in Sec. 6.4.

### 6.13 Abell 2111

Results for Abell 2111 are presented in Fig. 17. The source environment in the vicinity of Abell 2111 does not present a problem in our analysis: all the sources are located on the edge of the decrement or beyond and have flux densities  $\lesssim 3$  mJy (Fig. 17 A and Tab. 5). Some residual flux with a peak surface brightness  $\approx 700 \mu\text{Jy beam}^{-1}$  remains in our source-subtracted map but is sufficiently far ( $\approx 45''$ ) that it has a negligible effect on our SZ detection (Fig. 17 B).

X-ray studies of *ROSAT PSPC* and *HRI* data by Wang et al. (1997) reveal Abell 2111 has substructure on small scales but appears to be reasonably relaxed on larger scales away from the core. Wang et al. identify a main X-ray emitting component and a hotter subcomponent and conclude that Abell 2111 is most likely to be a head-on merger between two subclusters; this is supported by Henriksen et al. (1999) using ASCA data. A disturbed nature of

## Abell 1423

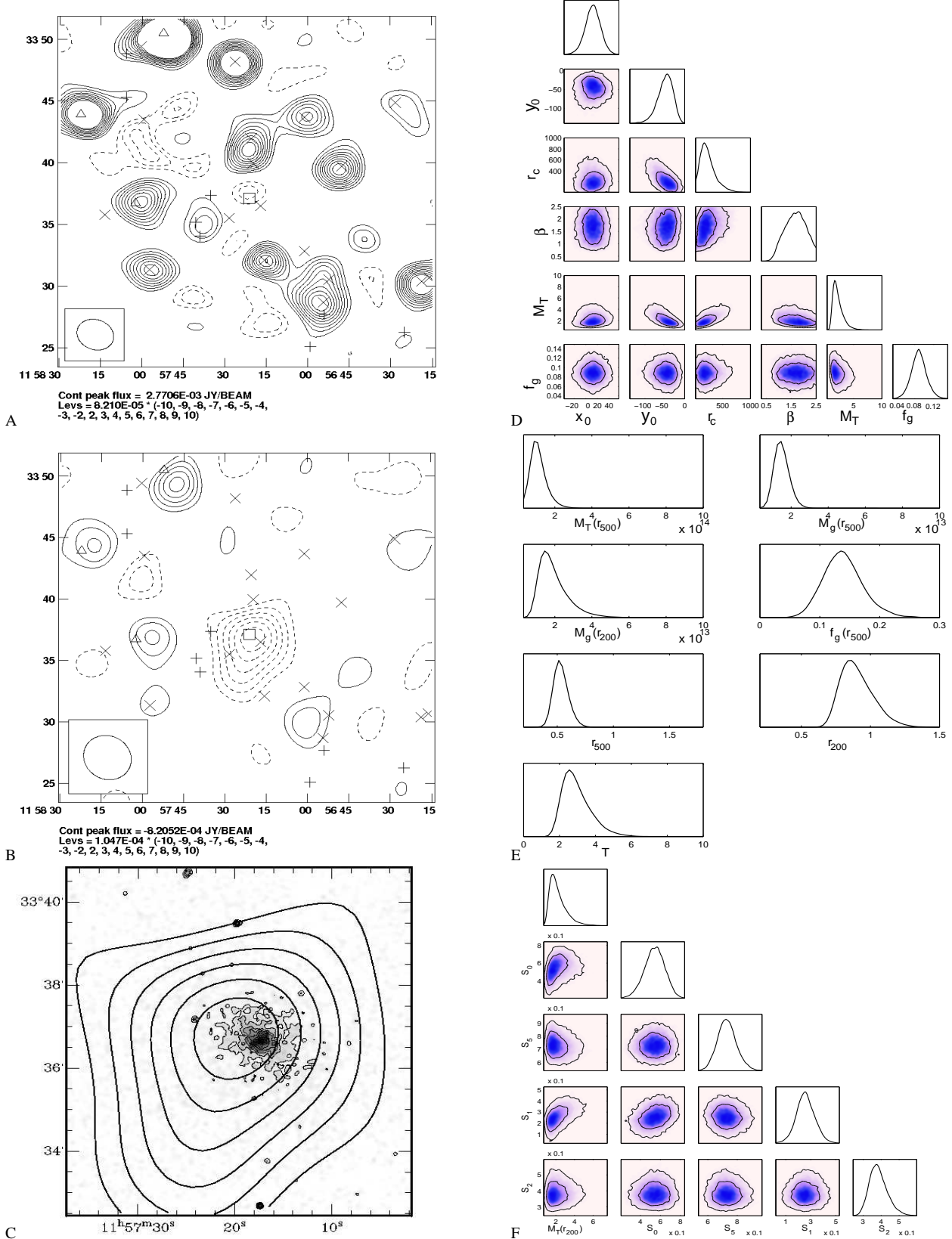


**Figure 11.** Results for Abell 1423. Panels A and B show the SA map before and after source-subtraction, respectively; a 0.6k1 taper has been applied to B. The box in panels A and B indicates the cluster SZ centroid, for the other symbols see Tab. 4. The smoothed CHANDRA X-ray map overlaid with contours from B is presented in image C. Panels D and E show the marginalized posterior distributions for the cluster sampling and derived parameters, respectively. F shows the 1 and 2-D marginalized posterior distributions for source flux densities (in Jys) within  $5'$  of the cluster SZ centroid (see Tab. 5) and  $M_T(r_{200})$  (in  $h_{100}^{-1} \times 10^{14} M_{\odot}$ ). In panel D  $M_T$  is given in units of  $h_{100}^{-1} \times 10^{14} M_{\odot}$  and  $f_g$  in  $h_{100}^{-1}$ ; both parameters are estimated within  $r_{200}$ . In E  $M_g$  is in units of  $h_{100}^{-2} M_{\odot}$ ,  $r$  in  $h_{100}^{-1} \text{Mpc}$  and  $T$  in KeV.

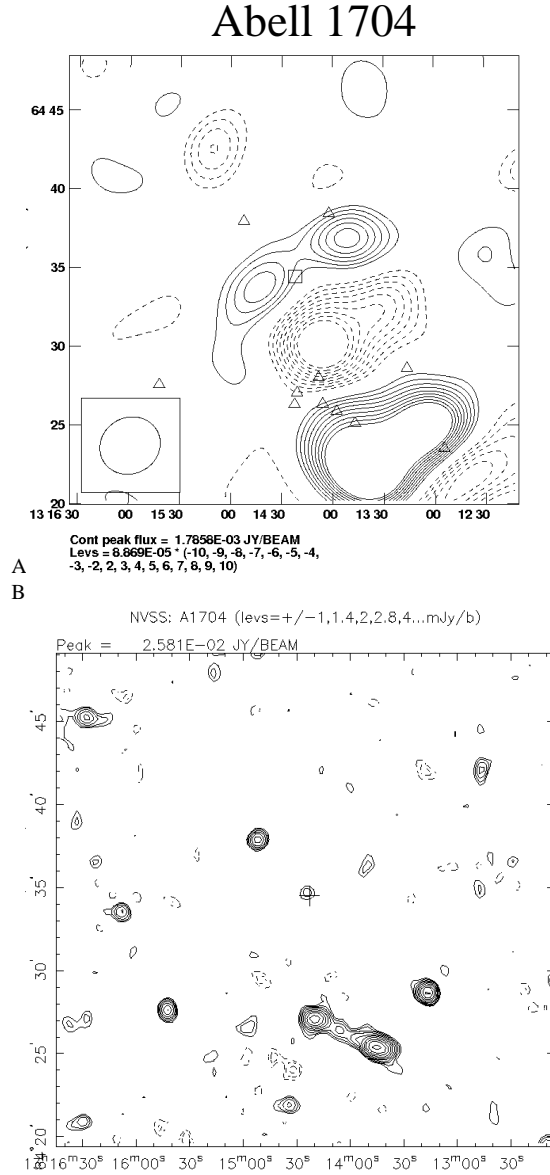


**Figure 12.** A: source-subtracted SA map produced using a 0.6-k $\lambda$  taper. The contours increase linearly in units of  $\sigma_{SA}$ . B: 1.4-GHz NVSS map towards Abell 1704.

Abell 2111 might also be indicated by the apparently clumpy X-ray emission and X-ray-SZ offset seen in Fig. 17 C.

Recent investigations by Rines et al. (2010) find the virial mass for Abell 2111 to be  $M_T(r_{100}) = 4.01 \pm 0.41 \times 10^{14} M_\odot$  using  $h_{70} = 1.0$  from an average of 90 member redshifts within  $r_{100}$ . Maughan et al. (2008) fit a modified version of the standard 1D isothermal  $\beta$ -model to CHANDRA data with  $h_{70} = 1.0$  to compute  $M_g(r_{500}) = 7.44^{+0.10}_{-0.05} \times 10^{13} M_\odot$ . We obtain a value of  $M_g(r_{500}) = 2.5 \pm 0.3 \times 10^{13} h_{70}^{-2} M_\odot$ . Previously, LaRoque et al. (2006) fitted an isothermal  $\beta$ -model to CHANDRA data (excising the  $r < 100$  kpc from the core) and OVRO/BIMA data and found a gas mass  $M_g(r_{2500}) = 2.15 \pm 0.42 \times 10^{13} M_\odot$  (for  $h_{70} = 1.0$ ); they also found an X-ray spectroscopic temperature of  $\approx 8.2$  keV. On larger scales, at  $r_{200}$ , we obtain a lower temperature,  $4.6 \pm 0.6$  keV, which suggests the average cluster temperature falls with radius. Moreover, Henriksen et al. report a radially decreasing temperature structure for Abell 2111 and parameterize it by a polytropic index

$\gamma \approx 1.45$ . On larger scales AMI Consortium: Hurley-Walker et al. (2011) estimate  $M_T(r_{200}) = 6.9 \pm 1.1 \times 10^{14} h_{70}^{-1} M_\odot$  from lensing data and  $M_T(r_{200}) = 6.3 \pm 2.1 \times 10^{14} h_{70}^{-1} M_\odot$  from AMI SZ data; they also find that a circular geometry is a slightly better fit to the data than an elliptical geometry. Our results,  $M_T(r_{200}) = 4.2 \pm 0.9 \times 10^{14} h_{100}^{-1} M_\odot$  are in very good agreement.

#### 6.14 Abell 2146

We have re-analysed the AMI data used in AMI Consortium: Rodríguez-González et al. (2010) with the cluster parameterization described in Sec. 5.1, which is slightly different to theirs; our results are presented in Fig. 6.14. They obtain  $M_g(r_{200}) = 4.9 \pm 0.5 \times 10^{13} h_{100}^{-2} M_\odot$  and  $T = 4.5 \pm 0.5$  keV while our results give  $M_g(r_{200}) = 4.4 \pm 0.6 \times 10^{13} h_{100}^{-2} M_\odot$  and  $T = 5.2 \pm 0.5$  keV. Given the similarities between the two analyses and the fact the same data were used for both, we would indeed

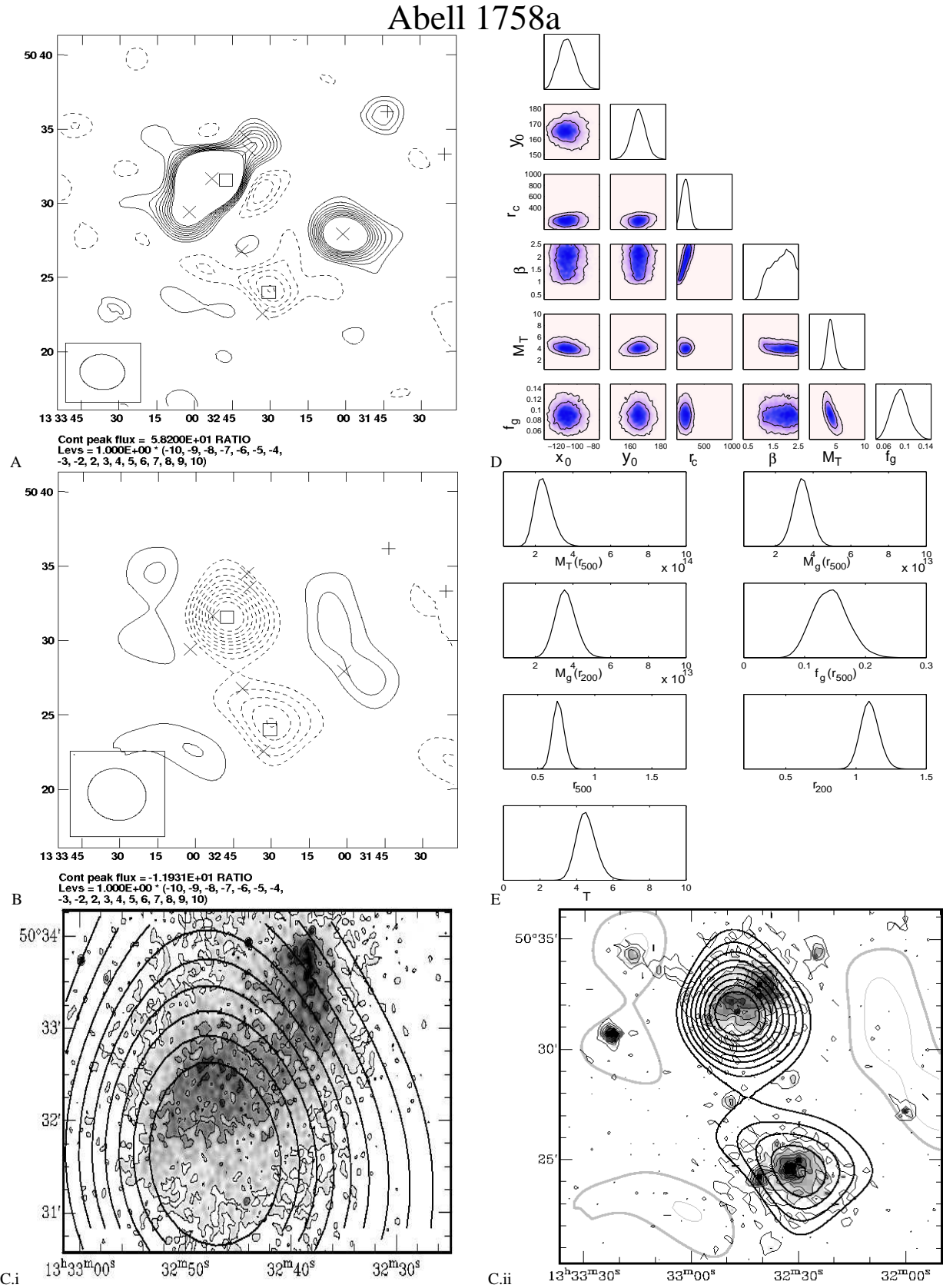


**Figure 13.** Panels A. and B. show the SA map before and after source subtraction (the latter map has had 0.6-k $\lambda$  taper applied to it). The boxes in panels A and B indicates SZ centroid for each cluster, for the other symbols see Tab. 4. The maps shown here are primary beam corrected signal-to-noise maps cut off at 0.3 of the primary beam. The noise level is  $\approx 115\mu\text{Jy}$  towards the upper cluster (Abell 1758a) and  $\approx 130\mu\text{Jy}$  towards the lower cluster (Abell 1758b). The source-subtracted SA maps from B are overlaid with the CHANDRA map in C.i and with ROSAT PSPC X-ray map in C.ii. D and E show the marginalized posterior distributions for sampling and derived parameters, respectively. In panel D,  $M_T$  is given in units of  $h_{100}^{-2} \times 10^{14} M_\odot$  and  $f_g$  in  $h_{100}^{-1} M_\odot$ ; both parameters are estimated within  $r_{200}$ . In E  $M_g$  is in units of  $h_{100}^{-2} M_\odot$ ,  $r$  in  $h_{100}^{-1} \text{Mpc}$  and  $T$  in KeV.

## Abell 1758b

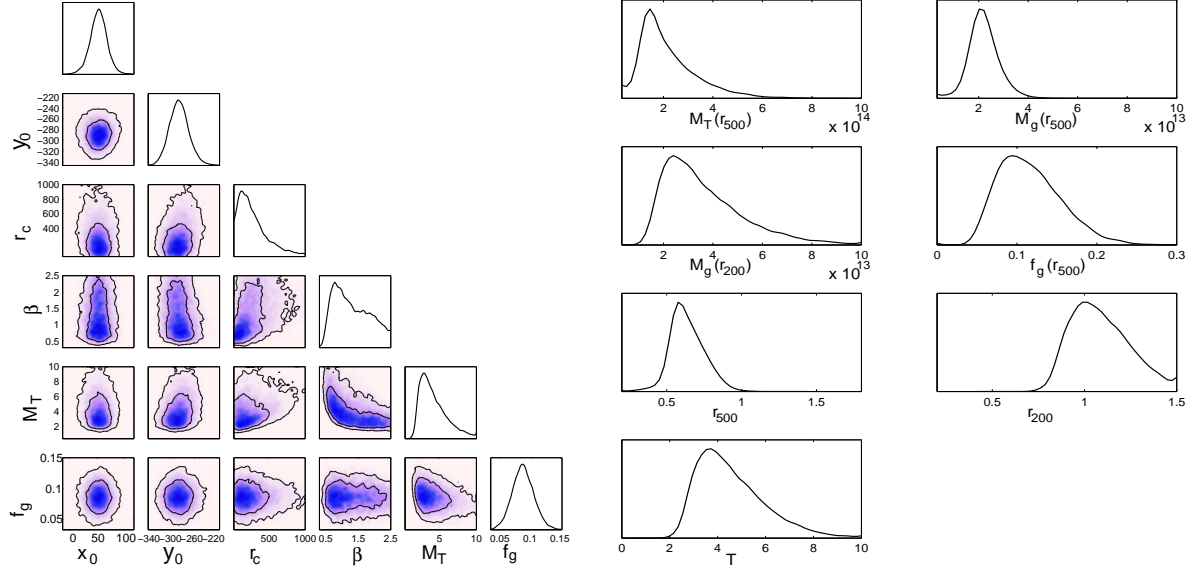


**Figure 14.** Abell 1758b. Left panel: 1 and 2-D marginalized posterior distributions for the cluster sampling parameters.  $M_T$  is given in units of  $h_{100}^{-1} \times 10^{14} M_\odot$  and  $f_g$  in  $h_{100}^{-1}$ ; both parameters are estimated within  $r_{200}$ . Right panel: 1-D marginalized posterior distributions for the cluster derived parameters.  $M_g$  is in units of  $h_{100}^{-2} M_\odot$ ,  $r$  in  $h_{100}^{-1}$  Mpc and  $T$  in KeV.

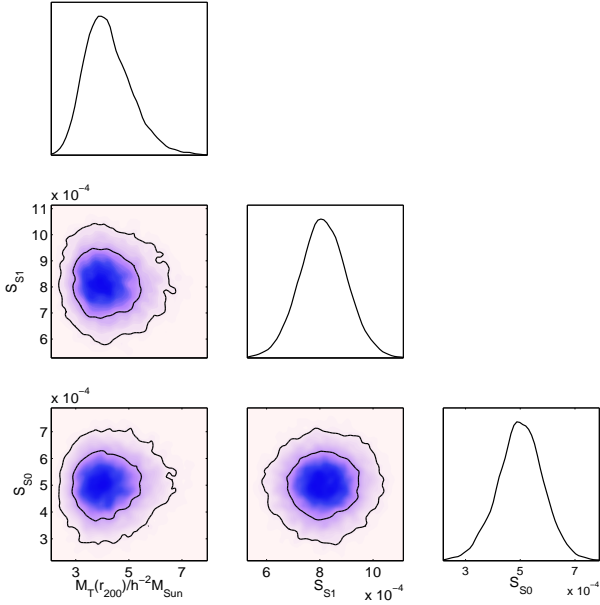


**Figure 18.** 2-D and 1-D marginalized posterior distributions for  $M_T(r_{200})$  (in  $h_{100}^{-1} M_\odot \times 10^{14}$ ) and source flux densities (in Jys) within  $5'$  from the cluster X-ray centroid for Abell 2111.

expect this good agreement between these sets of results. We have further investigated the effect of sources in this cluster and have found a slight degeneracy between the cluster mass and the flux density of the source lying closest to the cluster centre – see Fig. 20 F – which had not been seen for the brighter,  $\approx 6 \text{ mJy beam}^{-1}$  source lying a few arcseconds away from the cluster centroid.

CHANDRA data analysed by Russell et al. (2010) have revealed that Abell 2146 is undergoing a rare merger event similar to that of “Bullet-cluster” (Markevitch et al. 2002), with two shock fronts with Mach numbers  $M \approx 2$ , and strong non-uniformities in the

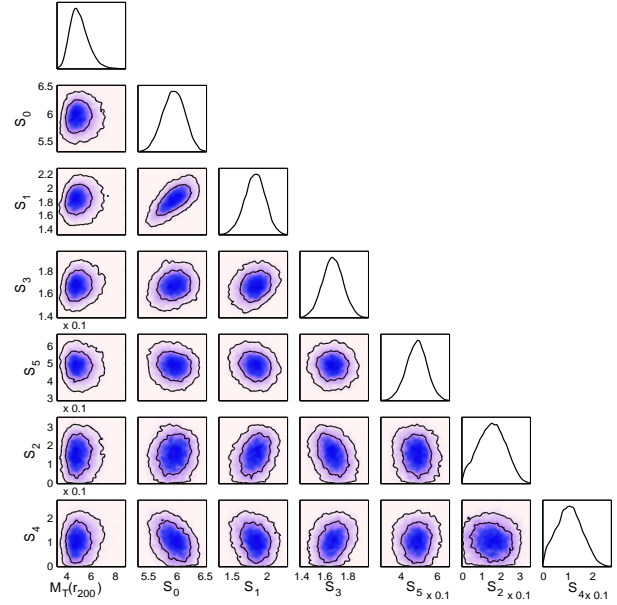


**Figure 20.** 2-D and 1-D marginalized posterior distributions for  $M_T(r_{200})$  (in  $h_{100}^{-1} \times 10^{14} M_\odot$ ) and source flux densities (in Jys; see Tab. 5) within  $5'$  from the cluster X-ray centroid for Abell 2146.

temperature profile. Note the different – essentially  $90^\circ$  – orientations between the X-ray and the SZ extensions. To understand this we have to consider collision geometry, mass ratio and, especially, time of snapshot since the merger start – see Sec. 8.

### 6.15 Abell 2218

Results for Abell 2218 are shown in Fig. 21. There is substantial radio emission towards Abell 2218, most of which is subtracted from our maps to leave a  $470 \mu\text{Jy beam}^{-1}$  positive feature to the



## Abell 2009

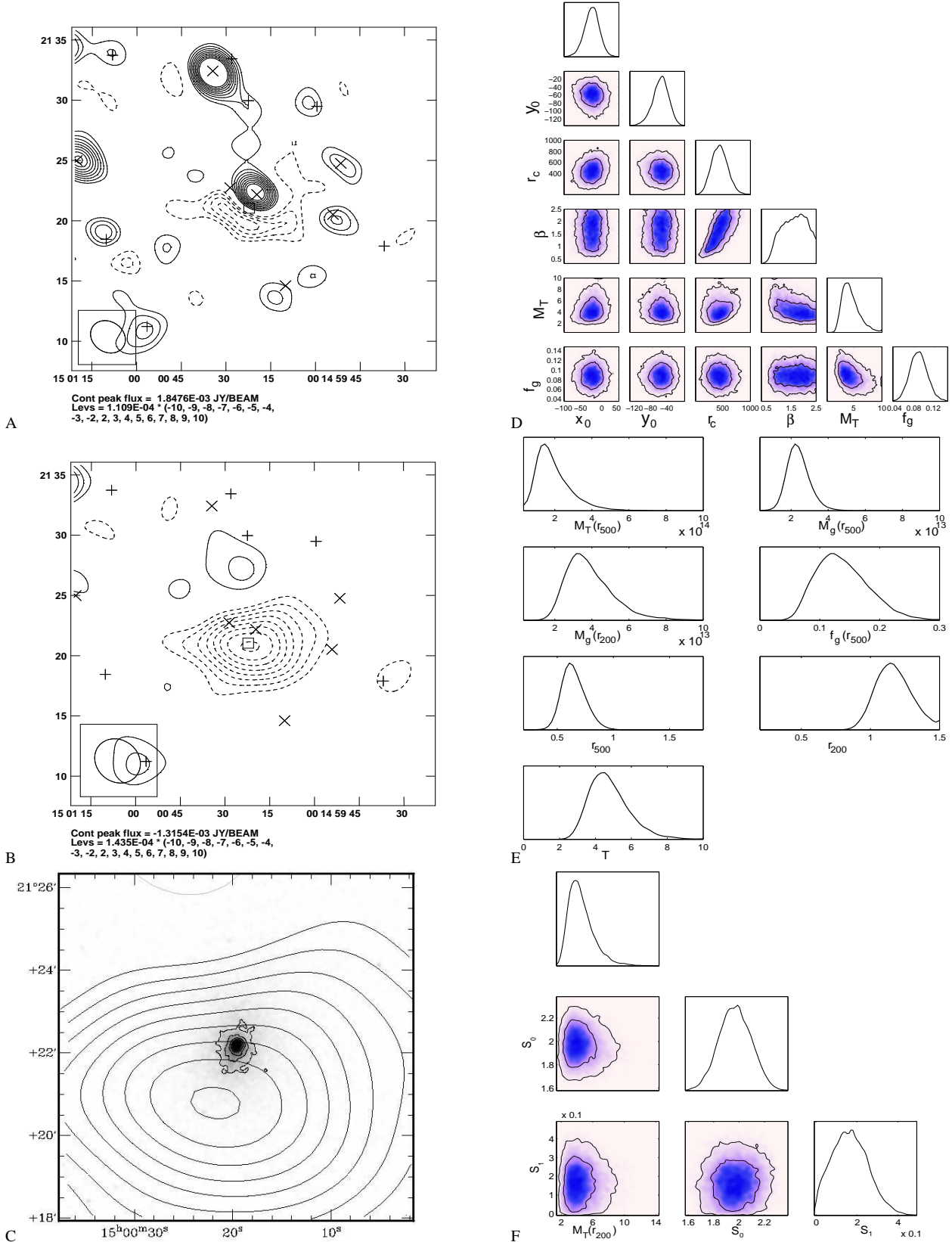


**Figure 16.** Results for Abell 2009. Panels A and B show the SA map before and after source-subtraction, respectively; a  $0.6\text{ k}\lambda$  taper has been applied to B. The box in panels A and B indicates the cluster SZ centroid, for the other symbols see Tab. 4. The smoothed CHANDRA X-ray map overlaid with contours from B is presented in image C. Panels D and E show the marginalized posterior distributions for the cluster sampling and derived parameters, respectively. F shows the 1 and 2-D marginalized posterior distributions for source flux densities (in Jys) given in Tab. 5 and  $M_T(r_{200})$  (in  $h_{100}^{-1} \times 10^{14} M_\odot$ ). In panel D  $M_T$  is given in units of  $h_{100}^{-1} \times 10^{14} M_\odot$  and  $f_g$  in  $h_{100}^{-1}$ ; both parameters are estimated within  $r_{200}$ . In E  $M_g$  is in units of  $h_{100}^{-2} M_\odot$ ,  $r$  in  $h_{100}^{-1}$  Mpc and  $T$  in KeV

## Abell 2111

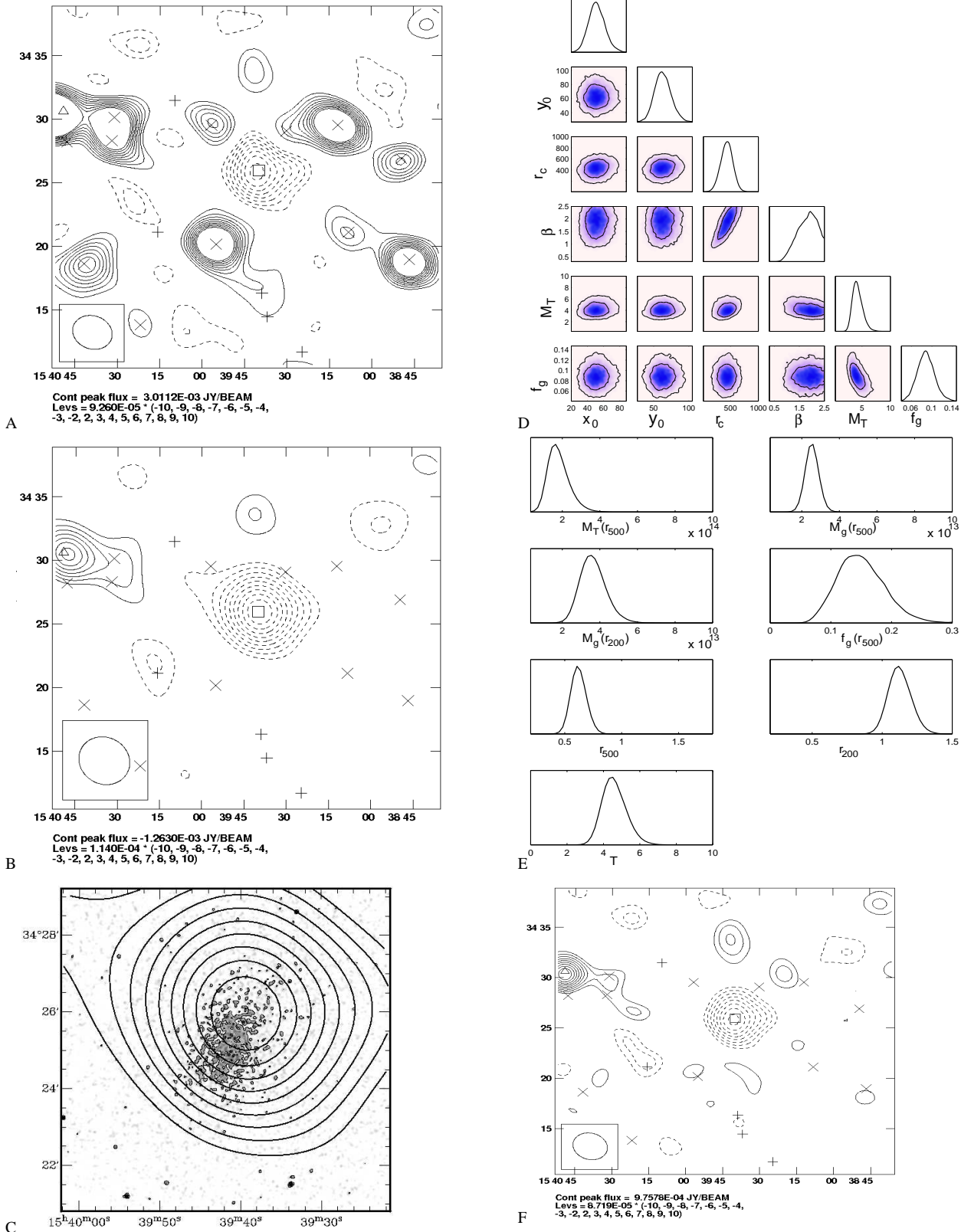


**Figure 17.** Results for Abell 2111. Panels A and B show the SA map before and after source-subtraction, respectively; a  $0.6\text{ k}\lambda$  taper has been applied to B. The box in panels A and B indicates the cluster SZ centroid, for the other symbols see Tab. 4. The smoothed CHANDRA X-ray map overlaid with contours from B is presented in image C. Panels D and E show the marginalized posterior distributions for the cluster sampling and derived parameters, respectively. F shows the higher-resolution source-subtracted map (no taper). In panel D  $M_T$  is given in units of  $h_{100}^{-1} \times 10^{14}$  and  $f_g$  in  $h_{100}^{-1}$ ; both parameters are estimated within  $r_{200}$ . In E  $M_g$  is in units of  $h_{100}^{-2} M_\odot$ ,  $r$  in  $h_{100}^{-1} \text{ Mpc}$  and  $T$  in KeV

## Abell 2146

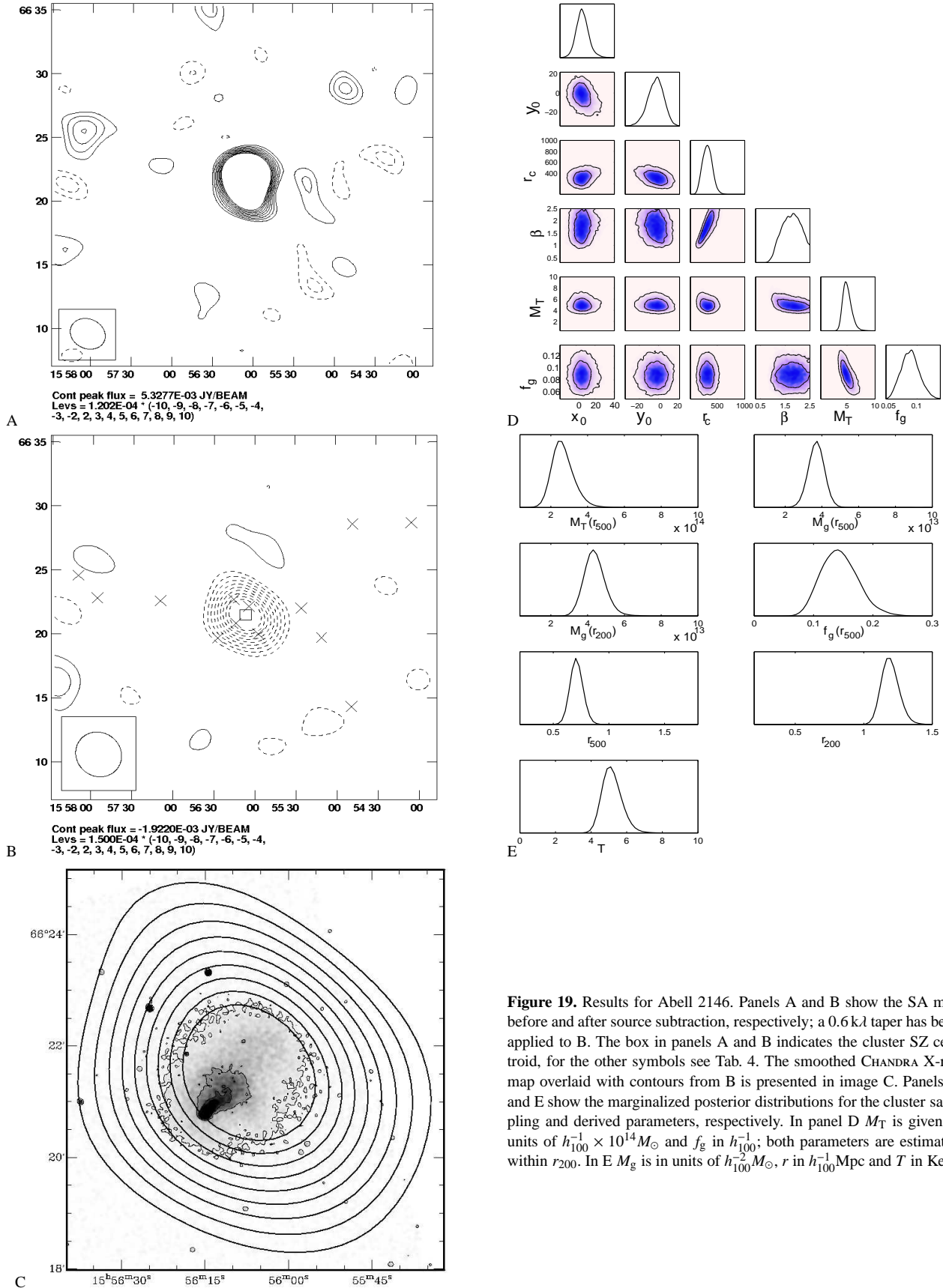


**Figure 19.** Results for Abell 2146. Panels A and B show the SA map before and after source subtraction, respectively; a  $0.6\text{ k}\lambda$  taper has been applied to B. The box in panels A and B indicates the cluster SZ centroid, for the other symbols see Tab. 4. The smoothed CHANDRA X-ray map overlaid with contours from B is presented in image C. Panels D and E show the marginalized posterior distributions for the cluster sampling and derived parameters, respectively. In panel D  $M_T$  is given in units of  $h_{100}^{-1} \times 10^{14} M_\odot$  and  $f_g$  in  $h_{100}^{-1}$ ; both parameters are estimated within  $r_{200}$ . In E  $M_g$  is in units of  $h_{100}^{-2} M_\odot$ ,  $r$  in  $h_{100}^{-1}$  Mpc and  $T$  in KeV.



West of the decrement, which could be extended emission. Rudnick et al. detect diffuse emission from a radio halo with a flux of 0.05 Jy within a 500 kpc radius at 327 MHz, from which one might expect a  $\leq 200 \mu\text{Jy}$  signal at 16 GHz (for a typical halo spectral index, see e.g., Hanisch (1980)).

Several observations in the X-ray (e.g., Markevitch 1997; Govoni et al. 2004; Machacek et al. 2002), optical (e.g., Giradi & Mezzetti 2001), SZ (e.g., Jones et al. 2005) and lensing (e.g., Squires et al. 1996 and Smith et al. 2004) have suggested that Abell 2218 is a complex, disturbed system. High-resolution *ROSAT* (Markevitch 1997) and *CHANDRA* (Govoni et al. 2004; Machacek et al. 2002) data show signs of substructure, particularly on small scales. Moreover, lensing studies by Squires et al. (1996) and Smith et al. (2004) have revealed a bi-modal mass distribution and associated elongated structures in the mass distribution. Abell 2218 also shows signs of strong temperature variations (Govoni et al. 2004 and Pratt et al. 2004). All of these results are indicative that the cluster is not relaxed.

SZ observations towards Abell 2218 have been made with the Ryle Telescope (Jones et al. 2005) at 15 GHz, at 36 GHz using the Nobeyama Telescope (Tsuboi et al. 1998) and with OCRA-p at 30 GHz (Lancaster 2007). Earlier SZ observations towards this cluster include Birkinshaw et al. (1981), Birkinshaw et al. (1984), Partridge et al. (1987), Klein et al. (1991), Jones et al. (1993) and Birkinshaw (1994).

Pratt et al. find from XMM-Newton data that  $T(r)$  falls from 8 keV near the centre to 6.6 keV at 700 kpc. Zhang et al. (2008) calculate a cluster mass estimate from the XMM-Newton data; using  $h_{70} = 1.0$ , they obtain  $M_{\text{T}}(r_{500}) = 4.2 \pm 1.3 \times 10^{14} M_{\odot}$  and  $f_{\text{g}}(r_{500}) = 0.15 \pm 0.09$ . We find  $M_{\text{T}}(r_{500}) = 2.7 \pm 0.6 \times 10^{14} h_{100}^{-1} M_{\odot}$ .

The *CHANDRA* X-ray image shown in Fig. 21 C appears to be extended along the N–S direction on arcminute scales and along the  $\approx$ SE–NW direction on scales  $\approx 2'$ . On the other hand, the distribution of the X-ray signal on larger scales,  $\approx 3'$ , tends to be more circular. On the untapered, source-subtracted SA map, Fig. 21 F, the SZ signal towards Abell 2218 is clearly extended. There is no significant degeneracy between the cluster mass and the source flux densities, as seen from Fig. 22.

### 6.16 Abell 2409

We detect a  $12\sigma_{\text{SA}}$  SZ effect towards Abell 2409 in the tapered, source-subtracted SA maps, Fig. 23 B. Despite the high SNR we are not able to obtain sensible parameter estimates for this cluster. As shown in Fig. 23 A, the effect of some emission close to the pointing centre is to give the decrement a shape that cannot be well approximated by a spherical  $\beta$ -profile with free shape parameters. The parameter estimates from McADAM are thus not reliable and we present only the AMI SA map. Fixing the shape of the profile can improve the fit to this cluster. Cluster parameters for Abell 2409 from AMI data have been obtained using a gNFW parameterization – see Planck and AMI Collaborations et al. (2012).

The nature of the residual emission around the cluster is uncertain. Pointed LA observations towards the location of these sources of positive flux were made in an attempt to detect possible sources lying just below our detection threshold. Despite the noise at these locations on the LA map reaching  $\approx 50 \mu\text{Jy beam}^{-1}$ , no additional sources were detected; it seems likely that this is (at this resolution) extended emission with relatively low surface brightness. However, no evidence for extended emission was found in either the NVSS 1.4 GHz or in the VLSS 74 MHz maps.

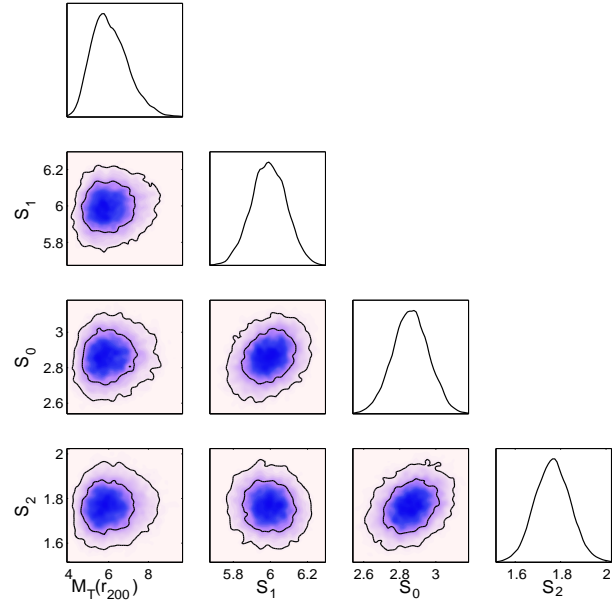


**Figure 22.** 2-D and 1-D marginalized posterior distributions for  $M_{\text{T}}(r_{200})$  (in  $h_{100}^{-1} \times 10^{14} M_{\odot}$ ) and source flux densities (in Jys) within  $5'$  from the cluster X-ray centroid for Abell 2218 (Tab. 5).

### 6.17 RXJ0142+2131

The maps and parameters for RXJ0142+2131 are presented in Fig. 24. The source environment is not expected to contaminate our SZ detection, with the brightest source having a flux density of  $\approx 2$  mJy and lying several arcminutes away from the cluster centroid; residual emission after source subtraction is seen on the SA maps at the  $1\sigma$  level. The composite image of the SZ and X-ray data reveals good agreement between the emission peaks of these two datasets.

A photometric and spectroscopic study of RXJ0142+2131 by Baars et al. (2005) finds the velocity dispersion of this cluster ( $\sigma_x = 1278 \pm 134 \text{ km s}^{-1}$ ) to be surprisingly large, given its X-ray luminosity (Tab. 1). This study indicates that galaxies in this cluster have older luminosity-weighted mean ages than expected, which could be explained by a short increase in the star formation rate, possibly due to a cluster-cluster merger. Moreover, RXJ0142+2131 shows signs of not being fully virialized since the brightest cluster galaxy was found to be displaced by  $1000 \text{ km s}^{-1}$  from the systemic cluster redshift. Okabe et al. (2010) fitted an NFW profile for the mass density to *Subaru/Suprime-Cam* data and assumed a spherical geometry for the cluster to derive  $M_{\text{T}}(r_{500}) = 2.85^{+0.60}_{-0.53} \times 10^{14} h_{72}^{-1} M_{\odot}$  and  $M_{\text{T}}(r_{200}) = 3.86^{+0.98}_{-0.82} \times 10^{14} h_{72}^{-1} M_{\odot}$  (using  $h_{72} = 1.0$ ). From our analysis, we find  $M_{\text{T}}(r_{500}) = 1.7 \pm 0.6 \times 10^{14} h_{100}^{-1} M_{\odot}$  and  $M_{\text{T}}(r_{200}) = 3.7^{+1.1}_{-1.2} \times 10^{14} h_{100}^{-1} M_{\odot}$ .

### 6.18 RXJ1720.1+2638

Results for RXJ1720.1+2638 are given in Fig. 25. At 16 GHz the source environment around the cluster is challenging: in our LA data we detect a 3.9 mJy source at the same position as the cluster, and several other sources with comparable flux densities within  $4'$  from the cluster centre. The difficulty of modelling this system is clear from the degeneracies between some of the source flux densities and the cluster mass (Fig. 25 F). However, we always recover a similarly asymmetric SZ decrement.

## Abell 2218

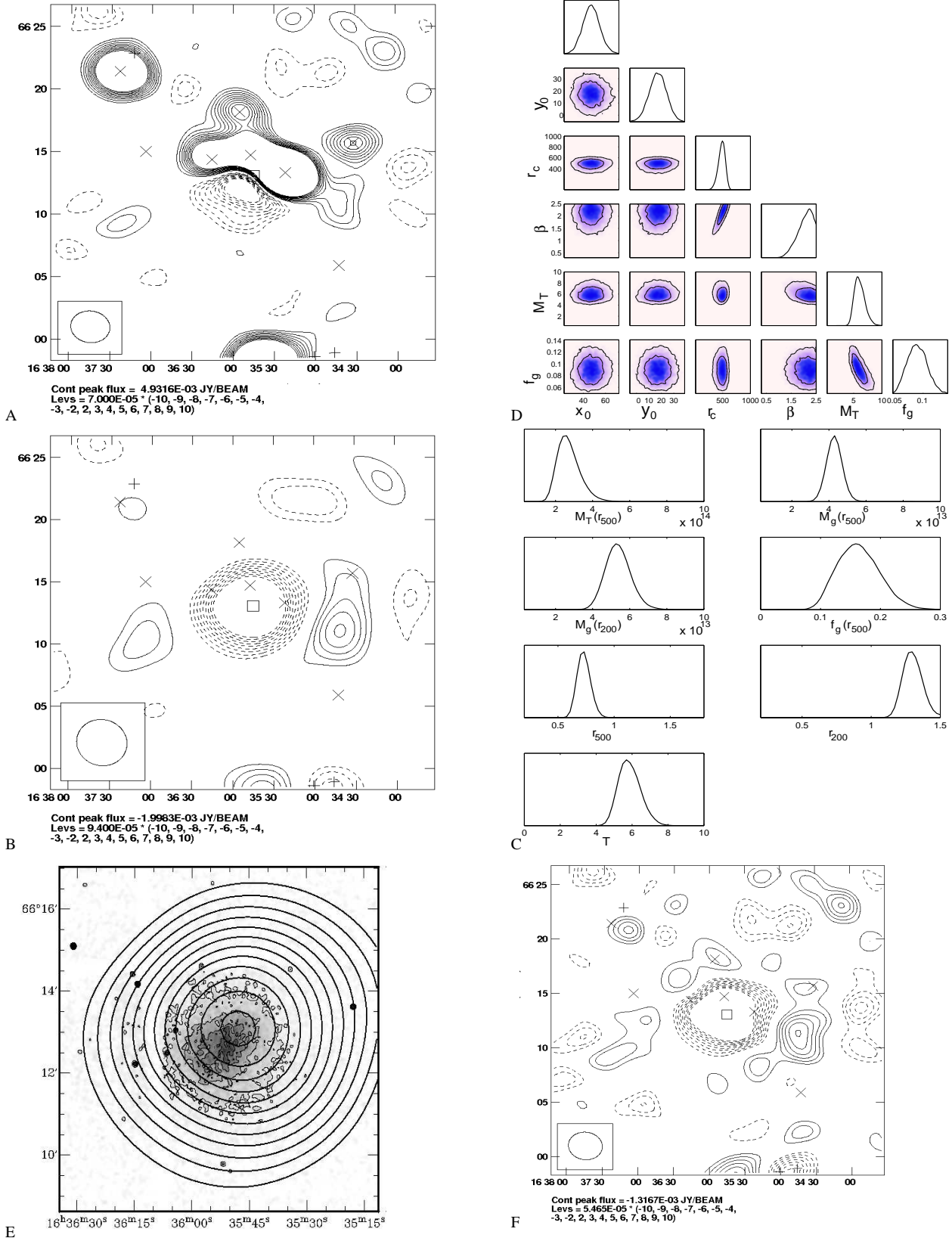


**Figure 21.** Results for Abell 2218. Panels A and B show the SA map before and after source subtraction, respectively; a  $0.6\text{ k}\lambda$  taper has been applied to B. The box in panels A and B indicates the cluster SZ centroid, for the other symbols see Tab. 4. The smoothed CHANDRA X-ray map overlaid with contours from B is presented in image C. Panels D and E show the marginalized posterior distributions for the cluster sampling and derived parameters, respectively. In panel D  $M_T$  is given in units of  $h_{100}^{-1} \times 10^{14} M_\odot$  and  $f_g$  in  $h_{100}^{-1}$ ; both parameters are estimated within  $r_{200}$ . In E  $M_g$  is in units of  $h_{100}^{-2} M_\odot$ ,  $r$  in  $h_{100}^{-1} \text{ Mpc}$  and  $T$  in KeV. F shows the higher-resolution source-subtracted map (no taper). Contours of the map in panel C are not the same as in panel B.; they range from  $-1.388$  to  $-0.188 \text{ mJy beam}^{-1}$  in steps of  $+0.15 \text{ mJy beam}^{-1}$ .

## Abell 2409

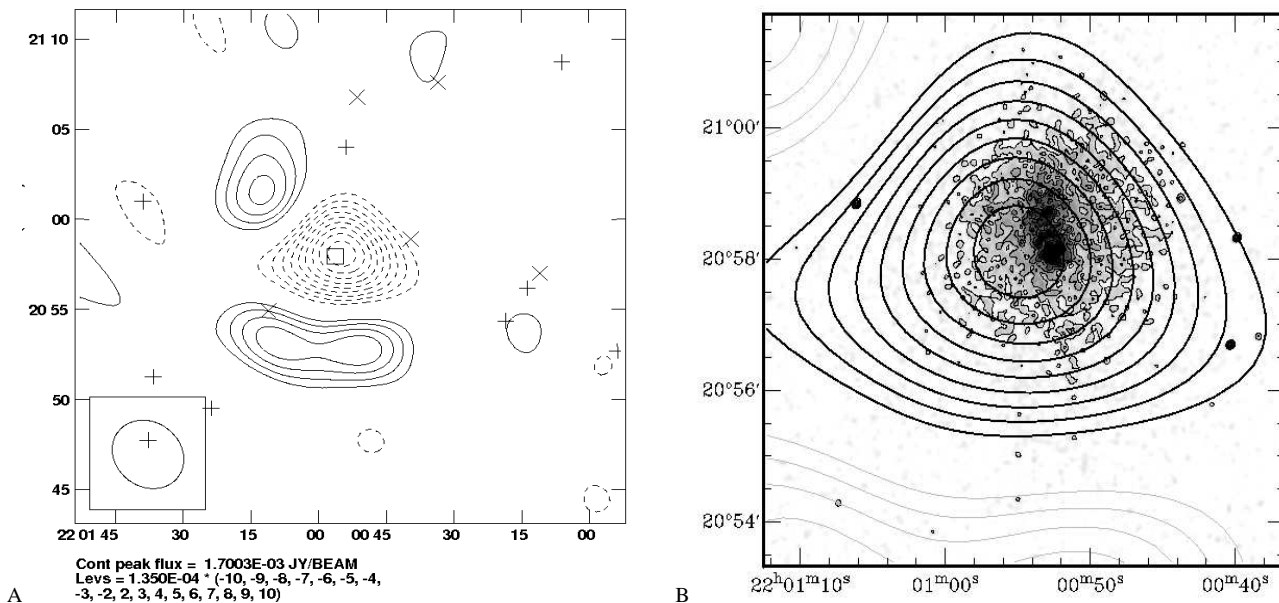


**Figure 23.** Results for Abell 2409. A: Source-subtracted SA map produced using a 0.6-k $\lambda$  taper. B: SA map from A. overlaid onto CHANDRA X-ray image. Contours increase linearly in units of  $\sigma_{SA}$ .

RXJ1720.1+2638 has been studied by Mazzotta et al. (2001) and Mazzotta & Giacintucci (2008) through CHANDRA observations. This cool-core cluster has two cold fronts within 100'' of the X-ray centroid and a regular morphology away from the core region; the authors attribute the dynamics of this cluster to the sloshing scenario, in agreement with later work by Owers, Nulsen, & Couch (2011) using optical spectroscopy. Merger activity has also been suggested by Okabe et al. whose weak lensing data reveal a second mass concentration to the North of the main cluster, while the analysis of SDSS data by Miller et al. (2005) finds no evidence of substructure. Our data reveal a strong abundance of radio emission towards this cluster, including some extended emission, which might support the suggestion in Mazzotta et al. (2001) that this cluster contains a low-frequency radio halo that did not disappear after the merger event.

Mazzotta et al. 2001 determined the mass profile for the cluster assuming hydrostatic equilibrium to be  $M_T(< r = 1000\text{kpc}) = 5_{-2}^{+3} \times 10^{14} h_{50}^{-1} M_{\odot}$ . We find  $M_T(r_{500}) = 1.2 \pm 0.2 \times 10^{14} h_{100}^{-1} M_{\odot}$ .

### 6.19 Zw0857.9+2107

We report a null detection of an SZ signal towards this cluster, despite the low noise levels on our SA maps and a seemingly benign source environment. We reached a noise level ( $1\sigma$ ) of  $97 \mu\text{Jy beam}^{-1}$  on the LA map (Fig. 26, middle panel) and found no evidence for sources below our  $4\sigma_{LA}$  detection threshold. We detect a 1.4 mJy radio source at the location of the peak X-ray signal (see the electronic version in the ACCEPT CHANDRA data archive for a higher resolution X-ray image) but we seem to be able to subtract it well from the SA maps.

Zw0857.9+2107 is not a well-studied cluster. There are two temperature measurements for the cluster gas in Zw0857.9+2107 from the ACCEPT CHANDRA data archive (Cavagnolo et al. 2000):  $T \approx 3 \pm 4$  keV between  $\approx 10 < r < 100$  kpc and  $T \approx 4.2 \pm 2.2$  keV between  $\approx 100 < r < 600$  kpc. One might expect the average tem-

perature for the cluster to be even lower at larger radii, such that  $T(r_{200}) < 3$  keV. The absence of an SZ signal could be explained by a sharp radial drop in  $T$  or, perhaps, this cluster is particularly dense and compact such that it is X-ray bright but does not produce a strong SZ signal on the scales AMI is sensitive to (Alastair Edge, private communication). Fig. 27 illustrates what the marginalized parameter distributions look like for non-detections such as this.

### 6.20 Zw1454.8+2233

We detect no SZ effect in the AMI data towards Zw1454.8+2233, despite the low noise levels of our SA maps. We detect several sources close to the cluster centre, including ones with a flux density of 1.64 mJy, 1.55 mJy and 8.4 mJy (at 13'', 1.8' and 4.3' away from the pointing centre, respectively). The SA maps and derived parameters are shown in Fig. 27. The derived parameters for this non-detection are as expected: we find that  $M_T(r_{200})$  approaches our lower prior limit and that  $M_g$  shows similar behaviour (see e.g., Fig. 27).

Zhang et al. found  $M_T(r_{500}) = 2.4 \pm 0.7 \times 10^{14} M_{\odot}$  using XMM-Newton, assuming isothermality, spherical symmetry and  $h_{70} = 1$ . CHANDRA X-ray observations by Bauer et al. (2005) suggest the cluster has a cooling flow and Venturi et al (2008) find from 610-MHz GMRT observations that the cluster has a core-halo radio source.

## 7 SOURCE-SUBTRACTION SIMULATION

Extracting robust cluster parameters for a system like Abell 2146 with bright sources lying at or very close to the cluster is extremely challenging. Many factors can affect the reliability of the detection and of the recovered parameters. Aside from model assumptions, other important factors are: the SNR of the decrement in our maps, the  $uv$ -coverage, the size of the cluster and the distance

## RXJ0142+2131

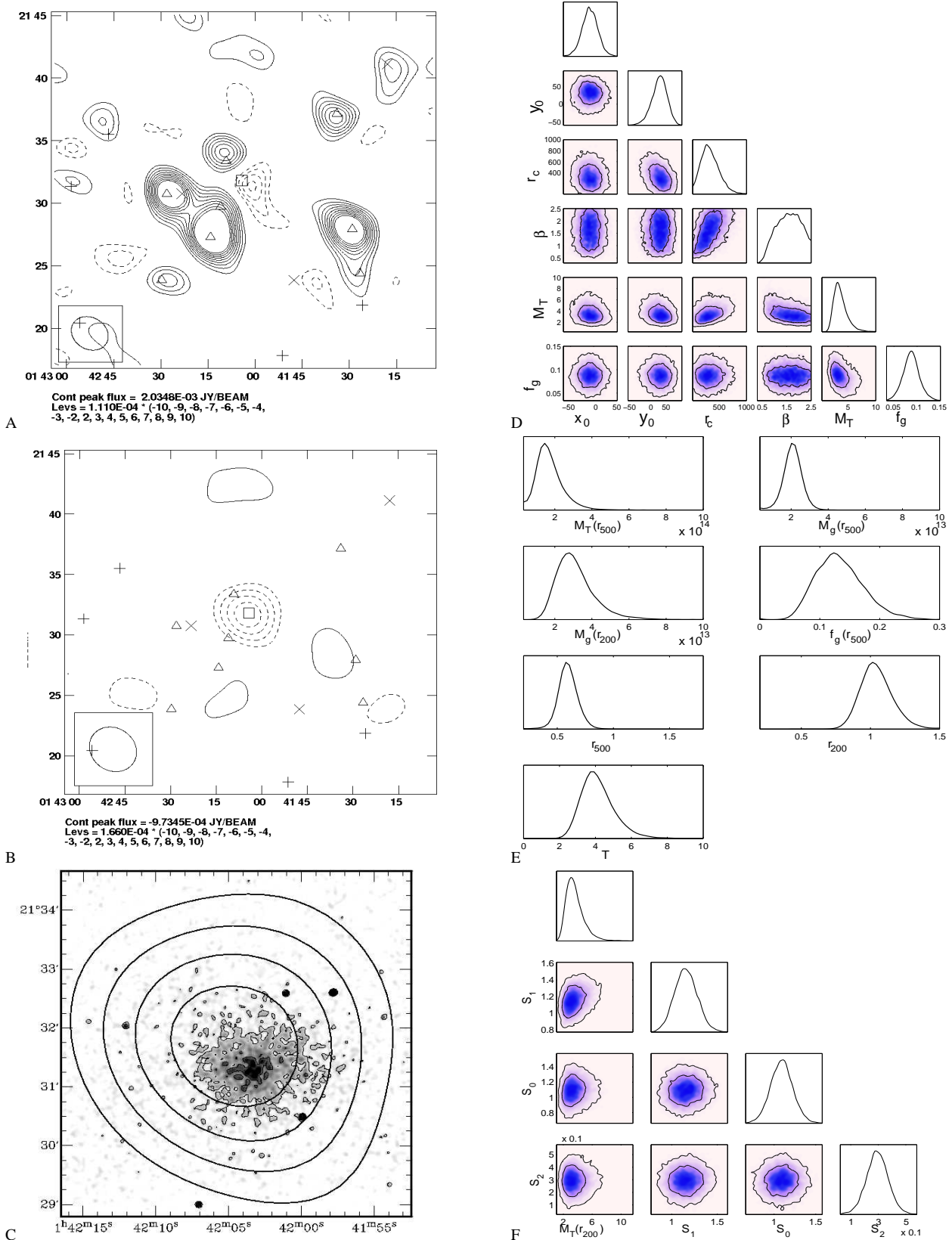


**Figure 24.** Results for RXJ0142+2131. Panels A and B show the SA map before and after source subtraction, respectively; a  $0.6\text{ k}\lambda$  taper has been applied to B. The box in panels A and B indicates the cluster SZ centroid, for the other symbols see Tab. 4. The smoothed CHANDRA X-ray map overlaid with contours from B is shown in image C. Panels D and E show the marginalized posterior distributions for the cluster sampling and derived parameters, respectively. F shows the 1 and 2-D marginalized posterior distributions for source flux densities (in Jys) within  $5'$  of the cluster SZ centroid (see Tab. 5) and  $M_T(r_{200})$  (in  $h_{100}^{-1} \times 10^{14} M_\odot$ ). In panel D  $M_T$  is given in units of  $h_{100}^{-1} \times 10^{14}$  and  $f_g$  in  $h_{100}^{-1}$ ; both parameters are estimated within  $r_{200}$ . In E  $M_g$  is in units of  $h_{100}^{-2} M_\odot$ ,  $r$  in  $h_{100}^{-1} \text{ Mpc}$  and  $T$  in KeV.

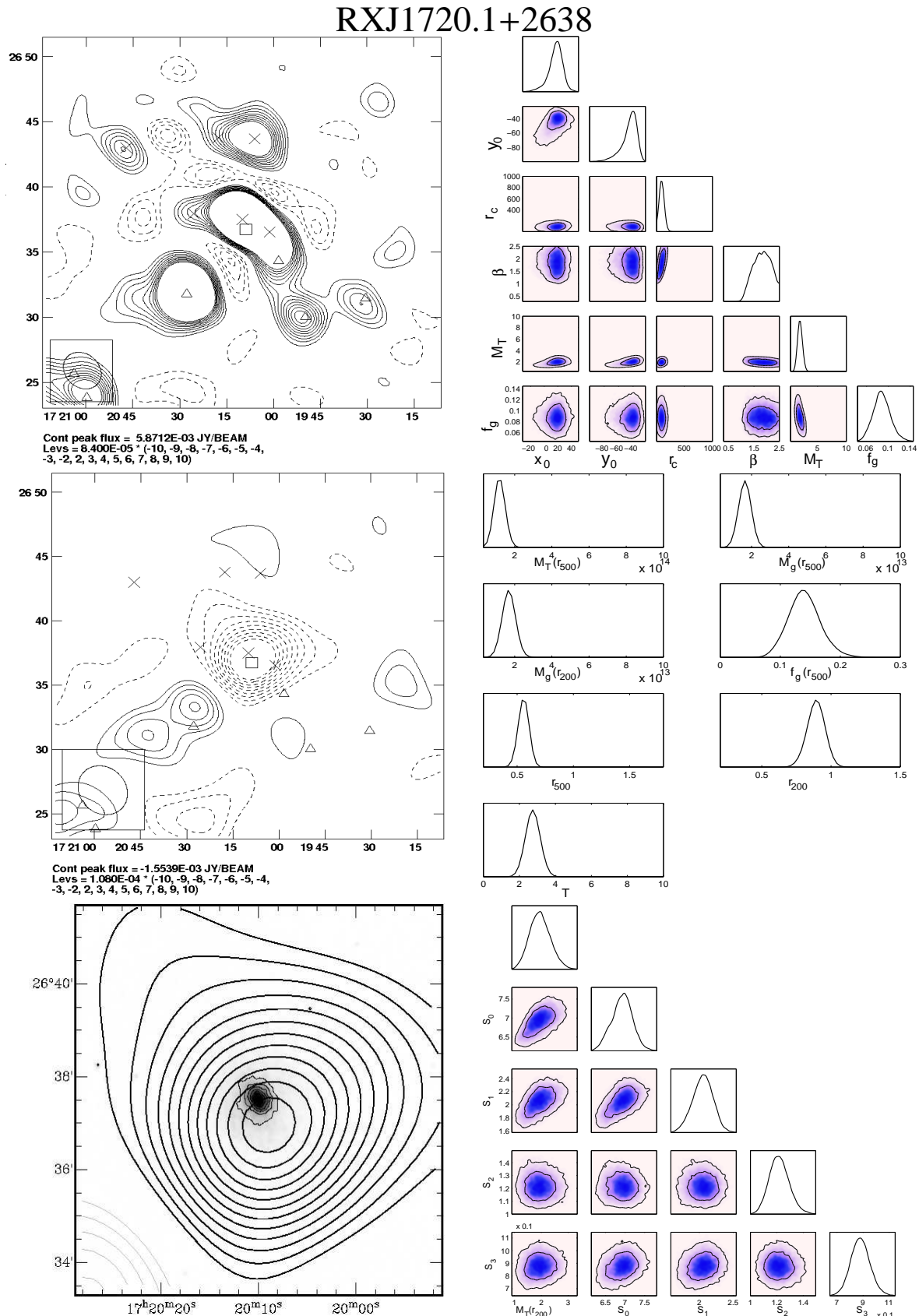


**Figure 25.** Results for RXJ1720.1+2638. Panels A and B show the SA map before and after source subtraction, respectively; a  $0.6\text{ k}\lambda$  taper has been applied to B. The box in panels A and B indicates the cluster SZ centroid, for the other symbols see Tab. 4. The smoothed CHANDRA X-ray map overlaid with contours from B is shown in image C. Panels D and E show the marginalized posterior distributions for the cluster sampling and derived parameters, respectively. F shows the 1- and 2-D marginalized posterior distributions for source flux densities (in Jys) given in Tab. 5 and  $M_T(r_{200})$  (in  $h_{100}^{-1} \times 10^{14} M_\odot$ ). In panel D  $M_T$  is given in units of  $h_{100}^{-1} \times 10^{14} M_\odot$  and  $f_g$  in  $h_{100}^{-1}$ ; both parameters are estimated within  $r_{200}$ . In E  $M_g$  is in units of  $h_{100}^{-2} M_\odot$ ,  $r$  in  $h_{100}^{-1} \text{ Mpc}$  and  $T$  in KeV.



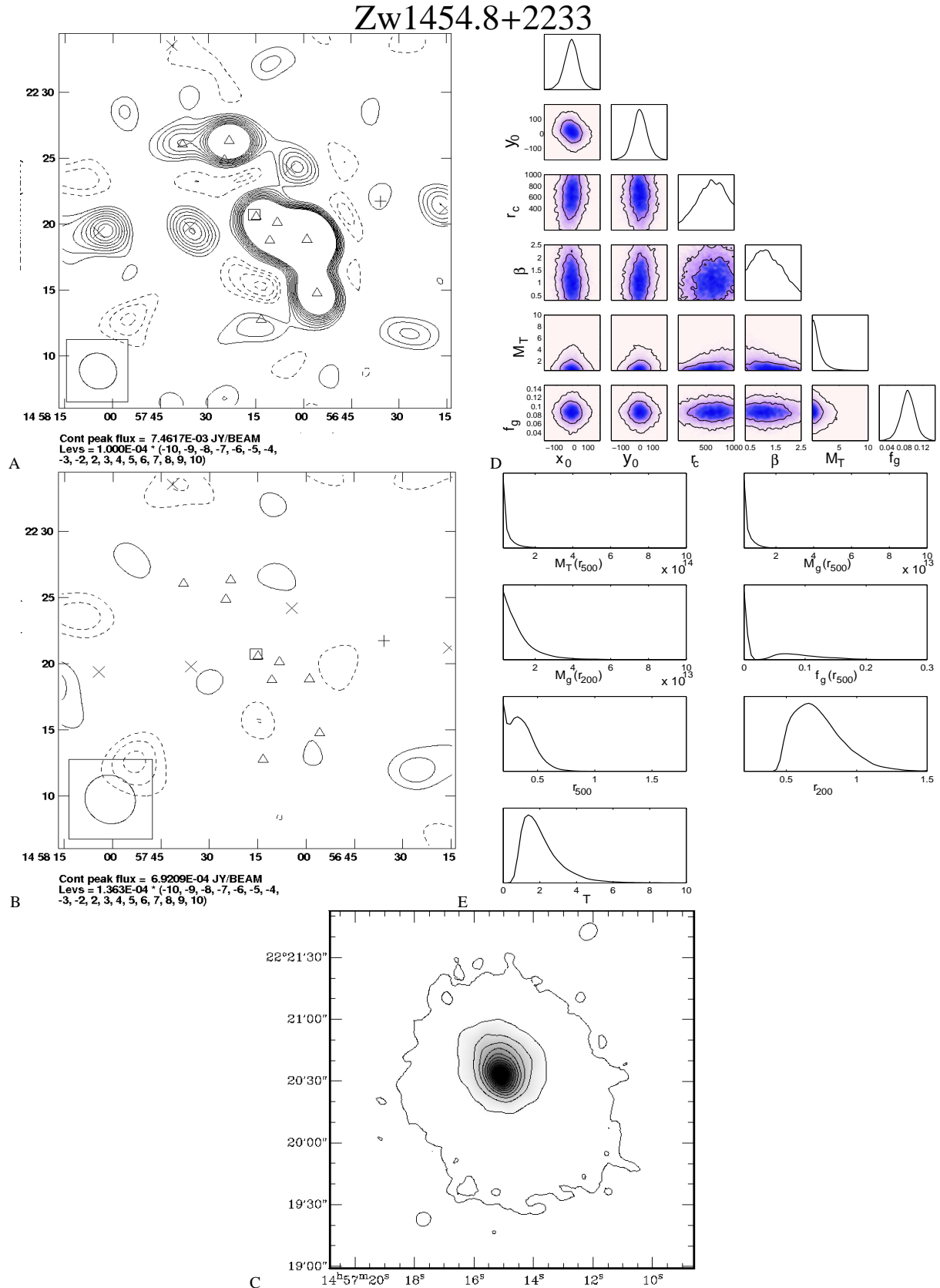


**Figure 27.** The null detection of Zw1454.8+2233 in SZ. Panel A shows the SA map before subtraction, which reveals the challenging source environment towards this cluster. The SA map after source subtraction is shown in panel B; no convincing SZ decrement is visible. Image C shows the CHANDRA X-ray map overlaid with SA contours from panel B. Panels D and E show the distributions for the sampling and derived parameters respectively; such distributions are consistent with a null detection. In panel D  $M_T$  is given in units of  $h_{100}^{-1} \times 10^{14} M_{\odot}$  and  $f_g$  in  $h_{100}^{-1}$ ; both parameters are estimated within  $r_{200}$ . In E  $M_g$  is in units of  $h_{100}^{-2} M_{\odot}$ ,  $r$  in  $h_{100}^{-1}$  Mpc and  $T$  in KeV.

## Zw0857.9+2107

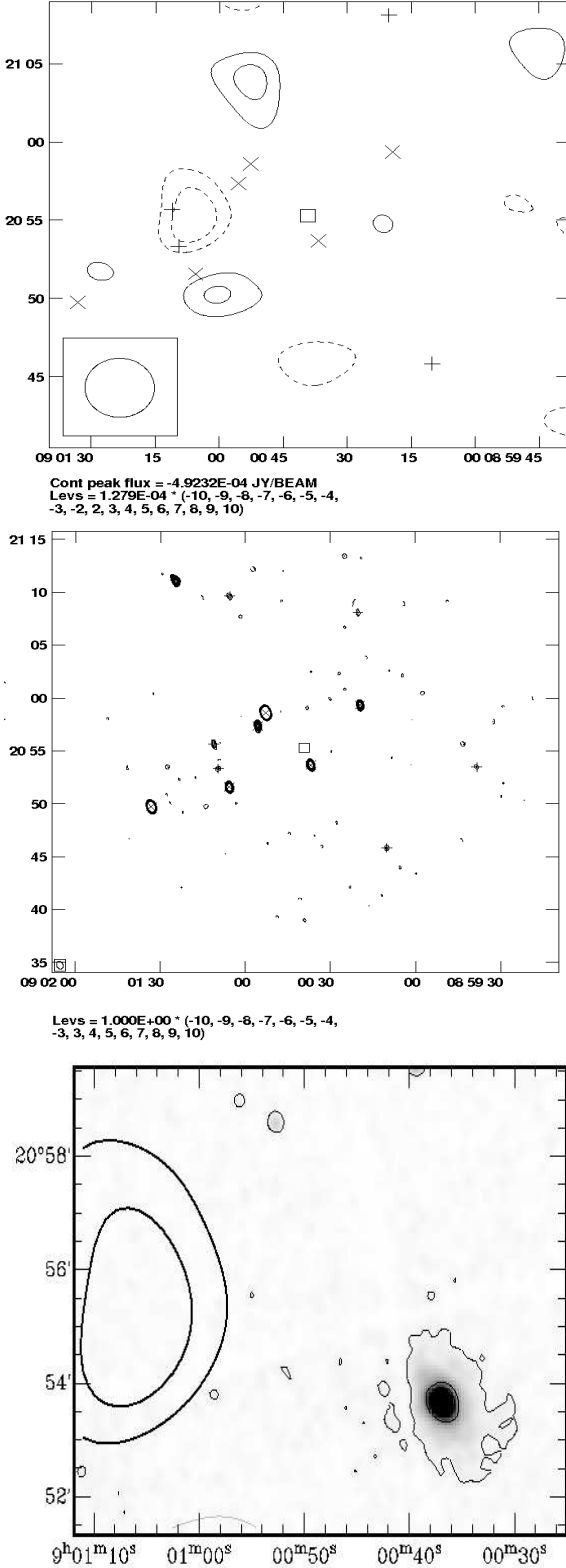


**Figure 26.** Top panel: Source-subtracted SA map for Zw0857.9+2107 produced using a 0.6-k $\lambda$  taper. The contours increase linearly in units of  $\sigma_{SA}$ . Middle panel: LA signal-to-noise map. Contours start at  $3\sigma$  and increase linearly to  $10\sigma$ , where  $\sigma = 97\mu\text{Jy Beam}^{-1}$ . Bottom panel: SA contours overlaid onto the Chandra X-ray image. The SA contours are the same as in the upper panel.

**Table 9.** Source parameters for the three simulated sources.

Source	RA (h m s)	Dec ( $^{\circ}$ ' '')	$S_{16}$ (Jy)	Spectral index
1	15 56 04.23	66 22 12.94	5.92	0.6
2	15 56 14.30	66 20 53.45	1.83	0.1
3	15 55 57.42	66 20 03.11	1.65	-0.2

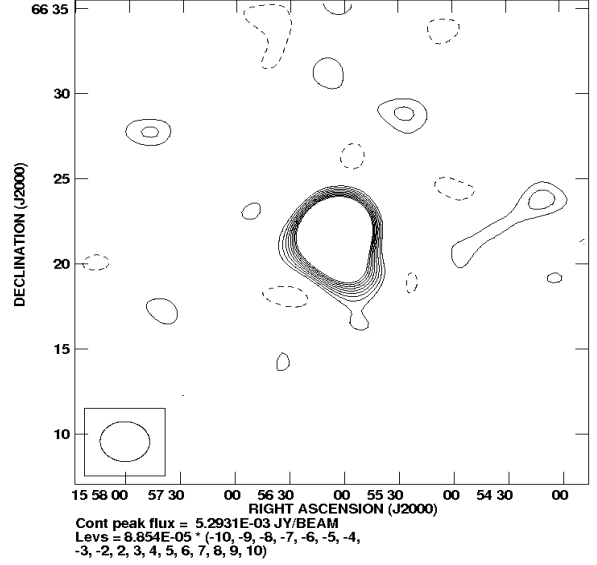


**Figure 28.** SA contour map of simulated data containing thermal noise + confusion noise + CMB + cluster + resolved point sources. Contours increase linearly in units of  $\sigma_{SA}$ .

of the sources from the cluster, their flux-densities and their morphologies. From Sec. 6, one can appreciate that at 16 GHz the SZ signal is potentially strongly contaminated by radio sources. We have examined some of the effects of these sources in a controlled environment through simulations. For this purpose, we generated mock visibilities between hour angles  $-4.0$  to  $4.0$ , with an RMS noise per channel per baseline per second of  $0.54$  Jy. Noise contributions from a CMB realisation and from confusion from faint sources lying below our subtraction limit were included; for the former we used a  $\Lambda$ CDM model and for the latter we integrated the 10C LA source counts from  $10\mu\text{Jy}$  to  $300\mu\text{Jy}$ . A cluster at  $z = 0.23$  was simulated using an isothermal  $\beta$ -profile to model the gas distribution, with a central electron density of  $9 \times 10^3 \text{ m}^{-3}$ ,  $\beta = 1.85$ ,  $r_c = 440h_{70}^{-1} \text{ kpc}$  and  $T = 4.8 \text{ keV}$ . Integrating the density profile out to  $r_{200}$  (Eq. 1) assuming a spherical cluster geometry yields  $M_g(r_{200}) = 6.25 \times 10^{13} h_{70}^{-2} M_{\odot}$ . From the virial  $M-T$  relation given in Eq. 4  $M_T(r_{200}) = 5.70 \times 10^{14} h_{70}^{-1} M_{\odot}$  and using these two estimates and Eq. 5, we find  $f_g(r_{200}) = 0.11 h_{70}^{-1}$ .

Three point sources were included into the simulation. Their positions, flux-densities and spectral indices are given in Tab. 9. The map of the data is shown in Fig. 28.

The data for the simulation were run through the same analysis as described in Sec. 5. In this case the source priors were centred on the simulated values (Tab. 9) and the cluster priors were the same of those in Tab. 3, with the delta-prior on  $z$  set to 0.23. The 1-D and 2-D marginalized posterior distributions for the sampling parameters are presented in Fig. 29. It can be seen that the cluster position and gas fraction are recovered well by the sampler; the core radius and  $\beta$  cannot be constrained by AMI data alone, thus, as expected,

**Table 10.** Median, mean and standard deviation for  $M_{SZ,sph}/M_{SZ,ellip}$  within  $r_{200}$  and  $r_{500}$  and  $T_{AMI,sph}/T_{AMI,ellip}$ . Data for all clusters in Tab. 15 were included, except for Abell 1758a and b. Ratios for each cluster at these two overdensities are given in Tab. 15.

	Median	Mean	Standard deviation
$M_{SZ,sph}/M_{SZ,ellip}$ within $r_{500}$	0.96	0.96	0.16
$M_{SZ,sph}/M_{SZ,ellip}$ within $r_{200}$	0.97	0.99	0.16
$T_{AMI,sph}/T_{AMI,ellip}$	0.98	0.98	0.10

the agreement between the input and output mean values for these parameters is poor; the total cluster mass, on the other hand, is very well-constrained and the recovered value is consistent with the input value. Hence, despite the challenging source environment, and the degeneracies between the cluster mass and the source flux densities, our analysis is able to provide robust cluster mass estimates.

## 8 DISCUSSION

Of the 20 target clusters, we have detected SZ towards 17, all of which are resolved, and with “peak” detections between  $5\sigma_{SA}$  and  $23\sigma_{SA}$ . The analysis has produced robust parameter extraction for 16 of the 17 – this was not possible for Abell 2409 because of nearby extended radio emission that distorts the SZ signal and gives an unacceptable fit for a spherical  $\beta$ -model. The three null detections are of Abell 1704 (difficult source environment), Zw0857.9+2107 (it is unclear to us why we have not detected this), and Zw1458.8+2233 (difficult source environment).

### 8.1 Cluster morphology and dynamics

The images frequently show significant differences in position of the SZ peak (and of the SZ centroid) and the X-ray peak, indicating that the densest part of a cluster is not at the centre of the large-scale gas distribution. In Abell 773 and Abell 2146, both mergers, there is evidence of SZ extension perpendicular to the X-ray emission. Abell 1758a and Abell A1758b are both major mergers and there is a hint of an SZ signal between a & b. Unlike what one might naively expect, there are cases of SZ extensions in non-mergers and cases of near-circular SZ map structures in mergers.

To attempt to quantify the cluster morphology from the AMI data, we ran our analysis with an ellipsoidal model for the cluster geometry. This model simply fits for two additional parameters: an ellipticity parameter,  $\eta$ , which is the ratio between the semi major and semi minor axes and an angle  $\theta$  measured anticlockwise from the West; these values are given in Tab. 11. For further details on this model see e.g., AMI Consortium: Hurley-Walker et al. (2011).

As a check that switching from spherical to ellipsoidal SZ analysis does not itself introduce significant bias in mass, we give in Tab. 10 the ratios  $M_{SZ,sph}/M_{SZ,ellip}$  within  $r_{200}$  and  $r_{500}$  and  $T_{AMI,sph}/T_{AMI,ellip}$ : no significant bias is evident. Of course, elsewhere in this paper we use spherical SZ estimates because the X-ray and almost all the optical total cluster mass estimates also assume spherical symmetry.

Tab. 11 also includes other possible indicators of dynamical state. The presence of cooling cores (CC) is associated with relaxed clusters since it is widely accepted that merger events tend to disrupt cooling flows, e.g., McGlynn & Fabian (1984). We have used CHANDRA data from the ACCEPT database, where available, to compute three CC indicators described in Hudson et al. (2010): the central entropy, the central cooling time and the ratio of (approximately) the central cluster temperature to the virial temperature;

Tab. 11 also includes other assessments of dynamical state that we have found in the literature.

The projected separation of the brightest cluster galaxy (BCG) and the peak of the X-ray emission has been shown to correlate with the dynamical equilibrium state of the the host cluster (Katayama et al. 2003 and Sanderson et al. 2009). Similarly, the offset between the SZ centroid and the X-ray peak can also be a diagnostic for cluster disturbance. For this purpose, the separation between the AMI SZ centroid, X-ray peak cluster position and the position of the BCG are given in Tab. 12; in Tab. 13 some sample statistics are provided. Large offsets between these measurements have been reported in observations (e.g., Massardi et al. 2010, Menanteau et al. 2011, and Korngut et al. 2011) and in simulations (e.g., (Molnar, Hearn, & Stadel 2012)).

Examination of Tabs. 11-13 indicates that even for well-studied clusters there are conflicting indications as to whether the cluster is a merger or not, e.g., Abell 773 does not appear to have a CC, has high degree of ellipticity, the X-ray and SZ signals appear to be oriented quasi-perpendicularly to each other and yet the relatively small position offsets in Tab. 12 might suggest the cluster is relaxed.

### 8.2 SZ temperature, large-radius X-ray temperature, and dynamics

In Fig. 30 we compare the AMI SA observed cluster temperatures within  $r_{200}$  ( $T_{AMI}$ ) with large-radius X-ray values ( $T_X$ ) from CHANDRA or SUZAKU that we have been able to find in the literature. We use *large-radius* ( $\approx 500$  kpc) X-ray temperature values to be consistent with the angular scales measured by AMI. (For Abell 611 we have plotted two X-ray values from CHANDRA data – one from the ACCEPT archive (Cavagnolo et al. 2000), which is higher than our AMI SA measurement, and a second X-ray measurement from CHANDRA (Donnarumma et al.), which is consistent with our measurement).

There is reasonable correspondence between SZ and X-ray temperatures at lower X-ray luminosity, with excess (over SZ) X-ray temperatures at higher X-ray luminosity. The mean, median and standard deviation for the ratio of  $T_{AMI}/T_X$  were found to be 0.7, 0.8 and 0.2, respectively, when considering all the cluster in Fig. 30 (except for Abell 1758a, due to it being a complex double-merger). The numbers are obviously small, but the two systems that are strong mergers by clear historical consensus – Abell 773 and Abell 1758a – are unambiguously clear outliers with much higher large-radius X-ray temperatures than SZ temperatures. Smith et al. (2004) investigate the scatter between lensing masses within  $\leq 500$  kpc with CHANDRA X-ray temperatures averaged over 0.1–2 Mpc for ten clusters and also find that disturbed systems have higher temperatures. However, Marrone et al. (2009) measure the relationship between SZ- $Y_{sph}$  and lensing masses within 350 kpc for 14 clusters and find no segregation between disturbed and relaxed systems. Kravtsov, Vikhlinin, & Nagai (2006) analysed a cluster sample extracted from cosmological simulations and noticed that X-ray temperatures of disturbed clusters were biased high, while the X-ray analogue of SZ- $Y_{sph}$ , did not depend strongly on cluster structure. Taken together, these results suggest that, even at small distances from the core, SZ-based mass (or temperature) is a less sensitive indicator of disturbance than is X-ray-based mass.

Major mergers in our sample have large-radius X-ray temperatures (at  $\approx 500$  kpc) *higher* than the SZ temperatures (averaged over the whole cluster). This suggests that the mergers affect the



**Table 11.** Dynamical indicators:  $\theta$ , the angle measured anticlockwise from the West,  $\eta$  the ratio between the semi major and semi minor axes (these values arise from fitting the SZ data with an elliptical geometry (see text)). Cooling core information: CC denotes the presence of a cooling core and NCC the lack of ('-' means this information is not clear or not known); Core<sub>1</sub> is a result from this study obtained by using three CC indicators described in Hudson et al. 2010 – the central entropy, the central cooling time and the ratio of approximately the central cluster temperature to the virial temperature,  $T_0/T_{\text{vir}}$ , where all the data have been taken from the CHANDRA ACCEPT database; Core<sub>2</sub> is cooling core information on the cluster available from other studies. †: the core type of Abell 1423 is unclear; the ratio of  $T_0/T_{\text{vir}}$  taken from ACCEPT suggests it is not a cool-core cluster but, a CC cannot be ruled out due to the large uncertainty in the X-ray temperature measurements; the central entropy and cooling time are unclear.

Cluster Name	$\theta$	$\eta$	Core <sub>1</sub>	Core <sub>2</sub>
Abell 586	136 ± 33	0.73 ± 0.13	NCC	CC Allen (2000), NCC Marrone et al. (2011)
Abell 611	79 ± 39	0.80 ± 0.12	NCC	NCC Marrone et al. (2011)
Abell 621	64 ± 61	0.73 ± 0.13	-	-
Abell 773	41 ± 12	0.59 ± 0.10	NCC	NCC Allen (2000)
Abell 781	132 ± 32	0.70 ± 0.13	-	-
Abell 990	109 ± 40	0.78 ± 0.13	-	-
Abell 1413	101 ± 21	0.75 ± 0.12	CC	CC Allen (2000), Richard et al. (2010)
Abell 1423(†)	66 ± 28	0.70 ± 0.14	NCC?	& CC? Sanderson et al. (2009)
Abell 1704	-	-	-	CC Allen (2000)
Abell 1758a	72 ± 31	0.73 ± 0.14	NCC	-
Abell 1758b	85 ± 49	0.77 ± 0.13	-	-
Abell 2009	88 ± 49	0.78 ± 0.12	-	-
Abell 2111	90 ± 29	0.77 ± 0.12	NCC	-
Abell 2146	126 ± 4	0.56 ± 0.05	-	'Bullet-like merger' Russell et al. (2010)
Abell 2218	107 ± 80	0.87 ± 0.07	NCC	NCC Richard et al. (2010)
Abell 2409	-	-	-	-
RXJ0142+2131	87 ± 41	0.77 ± 0.13	-	-
RXJ1720.1+263	26 ± 12	0.58 ± 0.07	CC	CC Richard et al. (2010)
Zw0857.9+2107	-	-	-	-
Zw1454.8+2233	-	-	-	CC Bauer et al. (2005)

**Table 12.** X-ray cluster position; SZ centroids from our analysis; position of the BCG from SDSS (the BCG was identified as the brightest galaxy in the central few hundred kpc from the cluster X-ray position. For clusters labelled with (\*) the BCG could not be identified unambiguously. Entries filled with a '-' indicate there is no available information.

Cluster Name	BCG		X-ray		SZ		Position offsets (")		
	RA (Deg)	Dec (Deg)	RA (Deg)	Dec (Deg)	RA (Deg)	Dec (Deg)	SZ-X-ray	SZ-SDSS	X-ray-SDSS
Abell 586	113.0844	31.6334	113.0833	31.6328	113.0833	31.6264	23.0	25.7	4.5
Abell 611	120.2367	36.0563	120.2458	36.0503	120.7958	36.0531	10.1	34.9	39.4
Abell 621	-	-	122.8000	70.0408	122.7875	70.0458	48.5	-	-
Abell 773	139.4724	51.7270	139.4666	51.7319	139.4667	51.7331	4.0	29.9	27.3
Abell 781(*)	140.1073	30.4941	140.1083	30.5147	140.1000	30.5314	67.0	136.7	74.2
Abell 990	155.9161	49.1438	155.9208	49.1439	155.9125	49.1369	39.0	27.9	16.9
Abell 1413	178.8250	23.4050	178.8250	23.4078	178.8250	23.3894	66.0	55.8	10.2
Abell 1423	179.3222	33.6110	179.3416	33.6319	179.3375	33.6189	49.2	62.2	103.0
Abell 1704	198.6025	64.5753	198.5917	64.5750	-	-	-	-	39.0
Abell 1758a(*)	203.1189	50.4697	203.1500	50.4806	179.3375	50.5264	209.3	209.3	118.6
Abell 1758b	-	-	-	-	203.1250	50.4003	209.3	209.3	-
Abell 2009	225.0833	21.3678	225.0811	21.3692	225.0875	21.3553	55.2	47.5	9.5
Abell 2111	234.9333	34.4156	234.9187	34.4240	234.9125	34.4331	39.4	97.9	60.8
Abell 2146	-	-	239.0291	66.3597	239.0250	66.3589	15.1	-	-
Abell 2218	-	-	248.9666	66.2139	248.9375	66.2186	106.1	-	-
Abell 2409	330.2189	20.9683	330.2208	20.9606	-	-	-	-	28.5
RXJ0142+2131	-	-	25.51250	21.5219	25.51667	21.5303	33.6	-	-
RXJ1720.1+2638	260.0418	26.6256	260.0416	26.6250	260.0333	26.6125	54.0	56.0	2.1
Zw0857.9+2107	135.1536	20.8943	135.1583	20.9158	-	-	-	-	79.5
Zw1454.8+2233	224.3130	22.3428	224.3125	22.3417	-	-	-	-	4.3

**Table 13.** Mean, standard deviation and median for the differences in X-ray and SZ cluster centroids and the position of the BCG from SDSS maps. Abell 1758 (a and b) has been excluded from this analysis due to its exceptionally disturbed state.

	Mean (")	Standard Deviation (")	Median (")
SZ - Xray	43.9	26.8	43.6
SZ - SDSS	51.6	35.3	43.6
Xray - SDSS	27.9	32.2	35.7

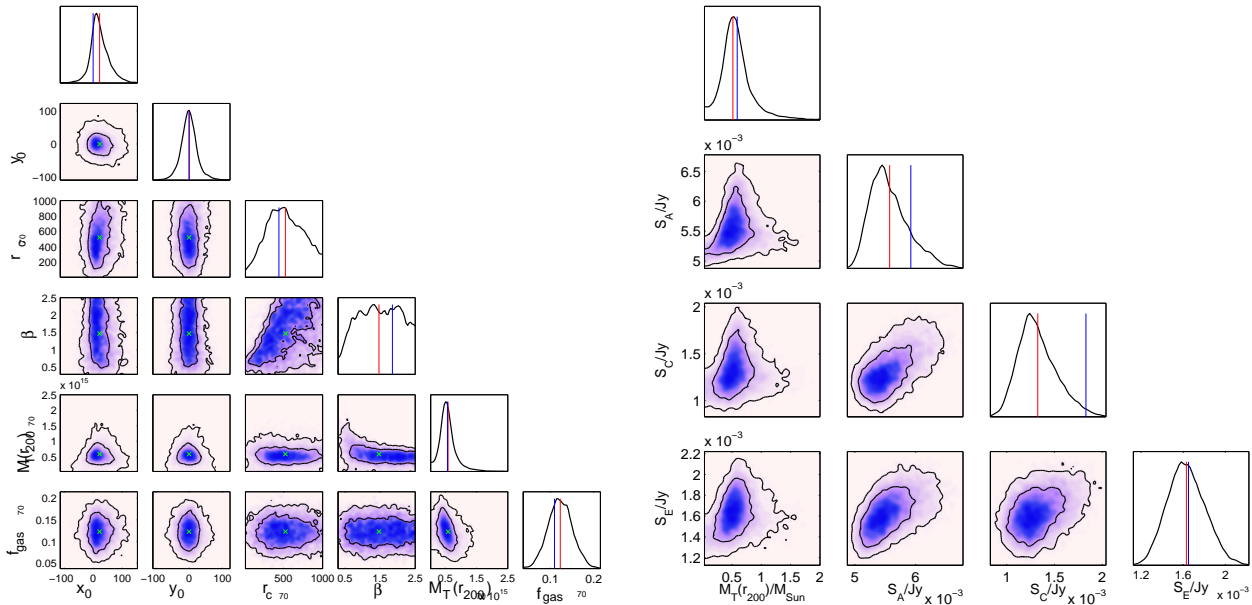


**Figure 29.** Left: One and two-dimensional marginalized posterior distributions for the cluster sampling parameters from our simulation.  $M_T$  and  $f_g$  are estimated within  $r_{200}$  and  $M_T$  is given in units of  $\times 10^{14}$ . The green crosses in the 2-D marginals denote the mean of the distribution. Right: One and two-dimensional marginalized posterior distributions for the source flux densities and  $M_T(r_{200})$  for our simulation. Red lines indicate the mean of the marginalized distribution and the blue lines represent the input value.

$n^2$ -weighted X-ray temperatures more than the  $n$ -weighted SZ temperatures and do so out to large radius. This is evidence for shocking or clumping or both *at large radius* in mergers. Indications that clumping at large  $r$  might have a significant impact on X-ray results have been found by e.g., Kawaharada et al. (2010), who find a flattening of the entropy profile around the virial radius, contrary to the theoretical predictions (e.g., Voit, Kay, & Bryan 2005). Hydrodynamical simulations by Nagai & Lau (2011) have shown that gas clumping can indeed introduce a large bias in large- $r$  X-ray measurements and could help explain the results by e.g., Kawaharada et al. It should be noted, however, that Mazzotta et al. (2004) expect X-ray temperatures to be lower than mass-weighted temperatures for clusters with temperature structure since the detectors of CHANDRA and XMM-NEWTON are more efficient on the soft bands, which leads to an upweighting of the cold gas. However, in simulations by Rasia et al. (2012) mass-weighted temperatures were shown to be larger than X-ray temperatures for the vast majority of their clusters, particularly for very the most disturbed clusters in their sample.

Examination of Fig. 30 given Tab. 11 is suggestive of another relation, again with obviously small numbers. Fig. 31, shows AMI cluster temperature versus large-scale X-ray temperature but with each cluster X-ray luminosity replaced by AMI ellipticity,  $\eta$ , and its error (note that we have removed the two Abell 611 points because of their apparently discrepant X-ray values). With one exception (Abell 2146), the clusters with large-radius X-ray temperature  $\geq 6$  keV have  $\eta$  values  $\leq 0.70$ , whereas the first two outliers to the right (RXJ1720.1+2638 and Abell 773) have significantly smaller values of AMI ellipticity. The rightmost outlier (Abell 1758a) itself has the ellipticity value  $0.73 \pm 0.14$  but this will be misleadingly high if we should instead be considering the ellipticity of the Abell 1758a+b taken as a merging pair. The true relationship between SZ ellipticity and merger state is bound to be influenced by the collision geometry, the time since the start of the merger (Fig. 1 in Nelson et al. 2011 illustrates how SZ  $\eta$  and  $\theta$  can vary with

merger evolution), the mass ratio, and so on. Far more data, including data on clusters not selected by X-ray luminosity, are essential.

### 8.3 Comparison of masses within $r_{500}$ and within the virial radius ( $\approx r_{200}$ )

The classical virial radius,  $\approx r_{200}$ , found is typically  $1.2 \pm 0.1$  Mpc. Values for  $M_T(r_{200})$  range from  $2.0^{+0.4}_{-0.1} \times 10^{14} h_{70}^{-1} M_\odot$  to  $6.1 \pm 0.9 \times 10^{14} h_{70}^{-1} M_\odot$  and are typically 2.0-2.5 $\times$  larger than  $M_T(r_{500})$ . In Fig. 32 and 33 AMI mass estimates at two overdensity radii are compared with other published mass estimates. The scarcity of mass measurements at large  $r$  is apparent from these figures.

- For  $M_T(r_{500})$ , there is good agreement between optical and AMI (HSE) mass estimates. In contrast, the X-ray (HSE) estimates tend to be higher, sometimes substantially so.

- For  $M_T(r_{200})$ , there is very good agreement between optical estimates, the SUZAKU X-ray (HSE) estimate, and the AMI ( $M-T$ ) estimates. Good agreement between AMI and optical masses has previously been reported by AMI Consortium: Hurley-Walker et al. (2011).

- From our sample we cannot determine whether the disagreement of masses is a function of radius.

- The discrepancy between the X-ray and AMI masses for Abell 1413 is reduced at  $r_{200}$ , with the X-ray mass being larger than the AMI mass by  $\approx 50\%$  at  $r_{500}$  and smaller than the AMI mass by  $\approx 10\%$  at  $r_{200}$ .

- The largest discrepancies between mass measurements in SZ, optical and X-ray correspond to the strongest mergers within our sample but the X-ray masses are always higher than our SZ masses, even for the few relaxed clusters in our sample. Given that the lensing masses agree well with our SZ estimates, this might be an indication of a stronger bias in masses estimated from X-ray data than from SZ or lensing data, especially for disturbed systems. However, most recent simulations and analyses indicate that X-ray HSE

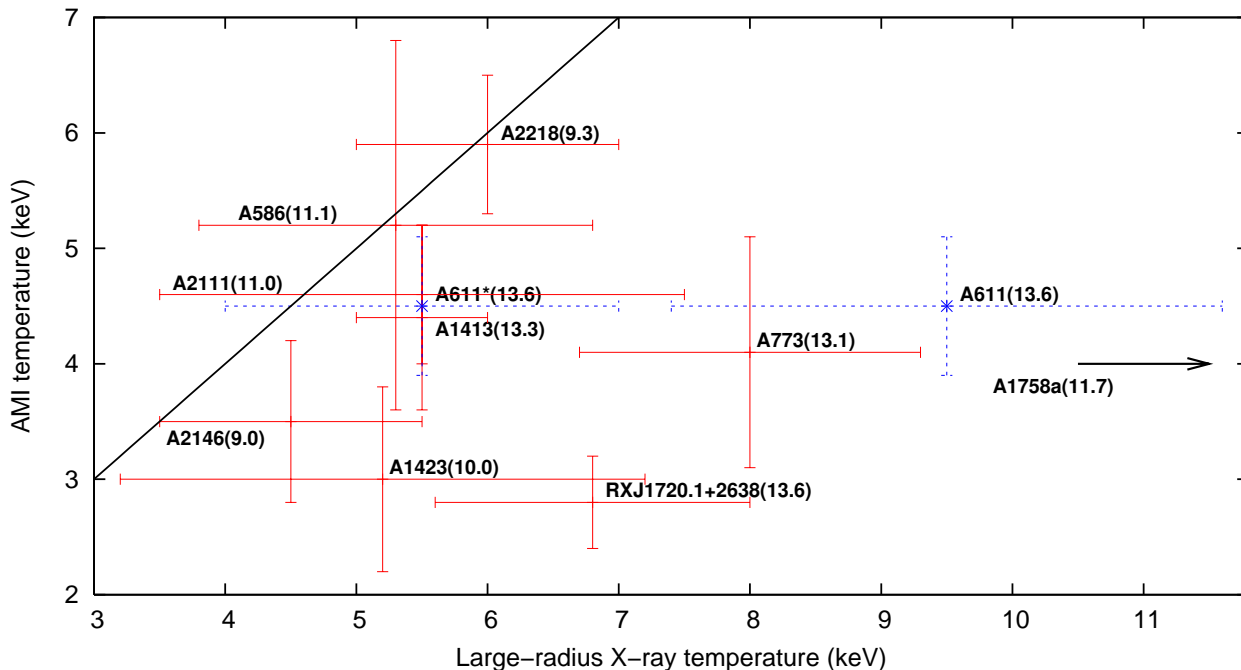


**Figure 30.** The AMI mean temperature within  $r_{200}$  versus the X-ray temperature. Each point is labelled with the cluster name and X-ray luminosity. Most of the X-ray measurements are large-radius temperatures from the ACCEPT archive (Cavagnolo et al. 2000) with 90% confidence bars. The radius of the measurements taken from the ACCEPT archive are 400-600 kpc for Abell 586, 300-700 kpc for Abell 611, 300-600 kpc for Abell 773, 450-700 kpc for Abell 1423, 500-1000 kpc for Abell 2111, 450-550 for Abell 2218 and for RXJ1720.1+2638  $r = 550$ -700 kpc. The Abell 611\* temperature is the 450-750 kpc value with 68% confidence bars (Donnarumma et al. 2010). The Abell 2146 temperature measurement is from Russell et al. 2010 with 68% confidence bars. The Abell 1413 X-ray temperature is estimated from the 700-1200 kpc measurements made with the *SUZAKU* satellite (Hoshino et al. 2010), this value is consistent with Vikhlinin et al. 2005 and Snowden et al. 2008. The ACCEPT archive temperature for Abell 1758A is  $16 \pm 7$  keV at  $r = 475$ -550 kpc, and with SZ temperature  $4.5 \pm 0.5$ , is off the right-hand edge of this plot. Abell 611 has been plotted using dashed blue lines to emphasize that this cluster has two X-ray-derived large- $r$  temperatures. The black diagonal solid line is the 1:1 line.

masses are underestimated with respect to lensing masses (e.g., Nagai et al. 2007, Meneghetti et al. 2010, Rasia et al. 2012).

### 8.3.1 Related results from the literature

To illustrate some of the issues in mass estimation, we bring together some of the other results in the literature.

#### • X-ray and weak-lensing masses

Observational studies by Mahdavi et al. (2008), Zhang et al. (2008) and Zhang et al. (2010) find systematic differences between X-ray HSE-derived and weak-lensing masses, with the lensing masses typically exceeding the X-ray masses. Mahdavi et al. report a strong radial dependence for this difference, with weak-lensing masses being  $\approx 3\%$  smaller within  $r_{2500}$  but  $\approx 20\%$  larger within  $r_{500}$  than the X-ray masses, yet find no correlation between the difference level and the presence of cool cores. Zhang et al. (2010) find that X-ray masses seem underestimated by  $\approx 10\%$  for undisturbed systems and overestimated by  $\approx 6\%$  for disturbed clusters within  $r_{500}$ . For relaxed clusters, they find the discrepancy is reduced at larger overdensities. The underestimate of HSE X-ray masses with respect

to lensing masses has been widely produced in simulations (e.g., Nagai et al. 2007, Meneghetti et al. 2010) and Rasia et al. 2012.

In Tab. 14 we follow Mahdavi et al. to calculate a weighted best-fit ratio of two mass estimates at different overdensities for different data. The simulations by Rasia et al. and Meneghetti et al. yield significantly lower  $M_X/M_{WL}$  at  $r_{500}$  than the observational data. Sijacki et al. (2007) suggest that a higher incidence of temperature substructure in the simulations might be responsible for this effect. It is interesting to see how the mass agreement for the study by Zhang et al. seems to weaken when excluding disturbed systems. What is very different from the literature is that we find HSE X-ray masses to be consistently higher than our HSE SZ masses within  $r_{500}$ . Modelling our clusters with an elliptical model for the cluster geometry does not substantially improve the agreement.

#### • SZ Y with X-ray and lensing masses

Bonamente et al. (2012) find good agreement between  $Y_{\text{sph}}(r_{500})$  estimated from a joint SZ and X-ray analysis and from SZ data alone, in support of results by Planck Collaboration et al. (2011). For their sample of massive, relaxed clusters there appears to be no significant systematics affecting the ICM pressure measurements from

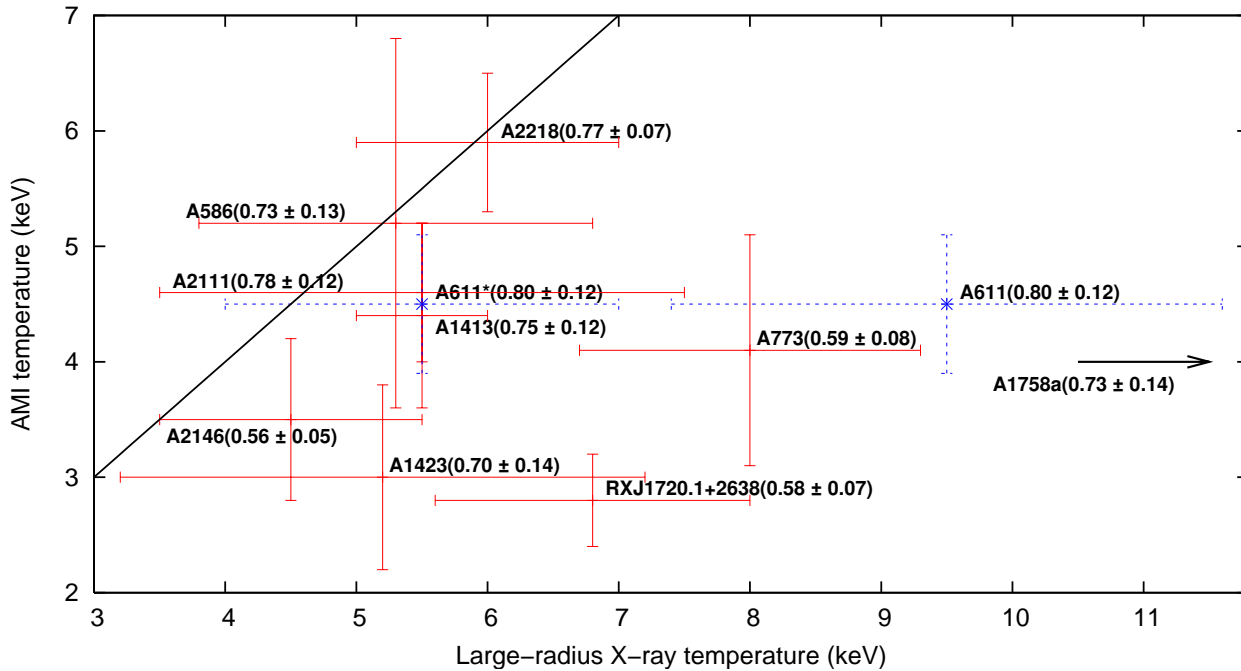


**Figure 31.** Plot analogous to Fig. 30 but with the X-ray luminosity values replaced by SZ  $\eta$  (ellipticity).

X-ray or SZ data. But, of course, this result might not be reproduced for a sample of disturbed clusters.

Marrone et al. (2009) measure the scaling between  $Y_{\text{SZ}}$  and weak lensing mass measurements within 350 kpc ( $\approx r_{4000-8000}$ ) for 14 LoCuSS clusters. They find it behaves consistently with the self-similar predictions, has considerably less scatter than the relation between lensing mass and  $T_X$  and does not depend strongly on the dynamical state of the cluster. They suggest SZ parameters derived from observations near the cluster cores may be less sensitive to the complicated physics of these regions than those in X-ray. A later study by Marrone et al. (2011) comparing two  $Y_{\text{SZ}} - M$  scaling relations using weak-lensing masses and X-ray (HSE) masses at  $r_{2500}$ ,  $r_{1000}$  and  $r_{500}$  indicates the latter has more scatter and is more sensitive to cluster morphology, with the mass estimates of undisturbed clusters exceeding those of disturbed clusters at fixed  $Y_{\text{sph}}$  by  $\approx 40\%$  at large overdensities. However, this division is not predicted by comparing SZ and true masses from simulations and is could due to the use of a simple spherical lens model. Moreover, recently, Rasia et al. (2012) have shown through simulations that selecting relaxed clusters for weak-lensing studies based on X-ray morphology is not optimal since there can be mass from, e.g., filaments not associated to X-ray counterparts biasing the lensing mass estimates even for systems which appear to be regular in X-rays.

#### • Simulations

Simulations of cluster mergers have shown these events generate turbulence, bulk flows and complex temperature structure, all of which can result in cluster mass biases (e.g., Poole et al. 2007).

Predominantly, simulations indicate that X-ray HSE masses tend to be underestimated (e.g., Krause et al. 2012) particularly in disturbed clusters, though the amount of the bias varies depending on the the simulation details, particularly on the physical processes taken into consideration. Projections effects, model assumptions and the dynamical state of the cluster are some of the factors affecting how well the true cluster mass can be measured. As shown by e.g., Takizawa, Nagino, & Matsushita (2010), even mass estimates for spherical X-ray systems are not always recovered well. Recent simulations by Nelson et al. (2011) have investigated in detail the evolution of the non-thermal support bias as function of radius and of the merger stage. They reveal a very complex picture: the HSE bias appears to vary in amplitude and direction radially and as the merger evolves (and the shocks propagate through); for the most part, the HSE bias leads to an underestimate for the mass, there are times when it has the opposite effect.

From simulations there appear to be two main, competing effects that can lead to a mass bias from the effects of a merger. Firstly, the merger event can boost the X-ray luminosity and temperature (e.g., Ricker & Sarazin 2001) such that if the cluster is observed during this period its X-ray mass will be overestimated. Secondly, the increase in non-thermal pressure support during the merger can lead to X-ray (HSE) cluster masses being underestimated (e.g., Lau, Kravtsov, & Nagai 2009). The cluster sample derived from simulations studied by Kravtsov, Vikhlinin, & Nagai (2006) showed that the X-ray temperatures were biased high for disturbed clusters, unlike  $Y_X$ , the product of the gas mass and tem-

**Table 14.** Best-fit mass ratios calculated following Mahdavi et al. 2008. R12 are the results from simulations by Rasia et al. 2012, ME10 are the simulations from Meneghetti et al. 2010, Z10 from Zhang et al. 2010 and MA10 from Mahdavi et al. 2008. For our results we have used for simplicity *sph* to denote our SZ masses derived using a spherical geometry and *ellip* when assuming an elliptical model. We have excluded Abell 1758 (A and B) from the analysis, given its abnormally disturbed and complex nature.

	$r_{500}$	$r_{200}$
$M_X/M_{WL}$		
R12- full sample	$0.75 \pm 0.02$	-
R12- regular clusters	$0.75 \pm 0.04$	-
ME10- full sample	$0.88 \pm 0.02$	-
Z10- full sample	$0.99 \pm 0.07$	-
Z10- relaxed	$0.91 \pm 0.06$	-
MA10- all	$0.78 \pm 0.09$	-
This work		
$M_X/M_{SZ,sph}$	$1.7 \pm 0.2$	-
$M_X/M_{SZ,ellip}$	$1.6 \pm 0.3$	-
$M_{SZ,sph}/M_{WL}$	$1.2^{+0.2}_{-0.3}$	$1.0 \pm 0.1$
$M_{SZ,ellip}/M_{WL}$	$1.2^{+0.2}_{-0.3}$	$0.9 \pm 0.1$

perature as deduced from X-ray observations (the X-ray analogue of the SZ  $Y$ ) which did not appear to depend strongly on cluster structure.

## 9 CONCLUSIONS

We observe 19 LoCuSS clusters with  $L_X > 7 \times 10^{37}$  W ( $h_{50} = 1.0$ ) and present SZ images before and after source subtraction for 16 of them (and for Abell 1758b, which was found within the FoV of Abell 1758a). We do not detect SZ effects towards Zw1458.8+2233 and Abell 1704, due to difficult source environments, nor towards Zw0857.9+2107, for reasons unclear to us. We have produced marginalized posterior distributions at  $r_{500}$  and  $r_{200}$  for 16 clusters (since Abell 2409 can not be fitted adequately by our model).

- Measurements of  $M_T(r_{200})$  are not common in the literature but are very important for testing large-radius scaling relations and understanding the physics in the outskirts of clusters. Consequently, the 16 measurements presented here, from a sample with narrow redshift-range, represent a significant increment to what already exists.

- For the clusters studied, we find values for  $M_T(r_{200})$  span  $2.0 - 6.1 \pm 0.9 \times 10^{14} h_{70}^{-1} M_\odot$  and are typically 2-2.5 times larger than  $M_T(r_{500})$ ; we find  $r_{200}$  is typically  $1.1 \pm 0.1 h_{70}^{-1}$  Mpc.

- AMI measurements of  $M_T(r_{500})$  are consistent with published optical results for 3 out of 4 clusters in our sample, with the weighted best-fit ratio<sup>9</sup> between AMI SZ masses and lensing masses being  $1.2^{+0.2}_{-0.3}$  within  $r_{500}$  and  $1.0 \pm 0.1$  within  $r_{200}$ . They are systematically lower than existing X-ray measurements of  $M_T(r_{500})$  for 6 clusters with available X-ray estimates and are only consistent with one of these measurements. The more discrepant masses correspond to the stronger mergers of the sample. The ratio of the X-ray masses to the AMI SZ masses is  $1.7 \pm 0.2$  for the sample. The agreement with optical measurements improves for  $M_T(r_{200})$ , though there are few data. We have investigated the AMI vs X-ray discrepancy by comparing  $T_{AMI}$  estimates with  $T_X$  estimates, when available, at  $r \approx 500$  kpc. There tends to be good agreement

in less X-ray luminous clusters and in non-mergers but large-radius  $T_X$  can be substantially larger than  $T_{AMI}$  in mergers. This explains why some X-ray mass estimates are significantly higher than the AMI estimates: the use of a higher temperature will give a consequently higher mass in the hydrostatic equilibrium model used. Another implication of a higher large-radius  $T_X$  than  $T_{AMI}$  (given the respective  $n^2$  and  $n$  emission weightings) is that, even at around  $r_{500}$ , the gas is clumped or shocked or both. There is a clear need for more large-scale measurements.

- We have investigated the effects of our main contaminant, radio sources, by searching for degeneracies in the posterior distributions of source flux densities for sources within  $5'$  of the cluster SZ centroids. We find small or negligible degeneracies between source flux densities and cluster mass for all clusters, with the exceptions of Abell 781, Abell 1758a and RXJ1720.1+2638, which have sources with flux densities of 9, 7 and 7 mJy at  $\lesssim 2'$  from the cluster SZ centroids. By simulating a cluster with a challenging source environment, we have shown that our AMI analysis can approximately recover the true mass, even in a degenerate scenario.

- We often find differences in the position of SZ and X-ray peaks, with an average offset of  $35''$ , a median of  $34''$  and a sample standard deviation of  $24''$  for the entire sample (excluding Abell 1758a+b), confirming what has been seen in previous observational studies and in simulations. We emphasize that our sample size is small, but we find no clear relation (except for Abell 1758) between position difference and merger activity. There is however an indication of a relation between merger activity and SZ ellipticity.

- We have analysed the AMI data for two clusters: Abell 611 and Abell 2111, with a  $\beta$  parameterization and with five gNFW parameterizations, including the widely used Arnaud et al. (2010) “universal” and the Nagai et al. (2007) ones. This has revealed very different degeneracies in  $Y_{sph}(r_{500}) - r_{500}$  for the two types of cluster parameterization. For both clusters, the  $\beta$  parameterization, which allows the shape parameters to be fitted, yielded stronger constraints on  $r_{500}$  than any of the gNFW parameterizations. The Nagai et al. and Arnaud et al. gNFW parameters produced consistent results, with the latter giving slightly better constraints. Setting the gNFW parameters to different, but reasonable, values altered the degeneracies significantly. This illustrates the risks of using a single set of fixed, averaged profile shape parameters to model all clusters.

## ACKNOWLEDGMENTS

We thank an anonymous referee for very quick and helpful comments and suggestions, and Alastair Edge for helpful discussion. We are grateful to the staff of the Cavendish Laboratory and the Mullard Radio Astronomy Observatory for the maintenance and operation of AMI. We acknowledge support from Cambridge University and STFC for funding and supporting AMI. MLD, TMOF, MO, CRG, MPS and TWS are grateful for support from STFC studentships. This work was carried out using the Darwin Supercomputer of Cambridge University High Performance Computing Service (<http://www.hpc.cam.ac.uk/>), provided by Dell Inc. using Strategic Research Infrastructure Funding from the Higher Education Funding Council for England and the Altix 3700 supercomputer at DAMTP, Cambridge University, supported by HEFCE and STFC. We thank Stuart Rankin and Andrey Kalizhin for their computing support. This research has made use of data from the CHANDRA Data Archive (ACCEPT) (Cavagnolo et al.

<sup>9</sup> With the exception of Abell 1758a+b

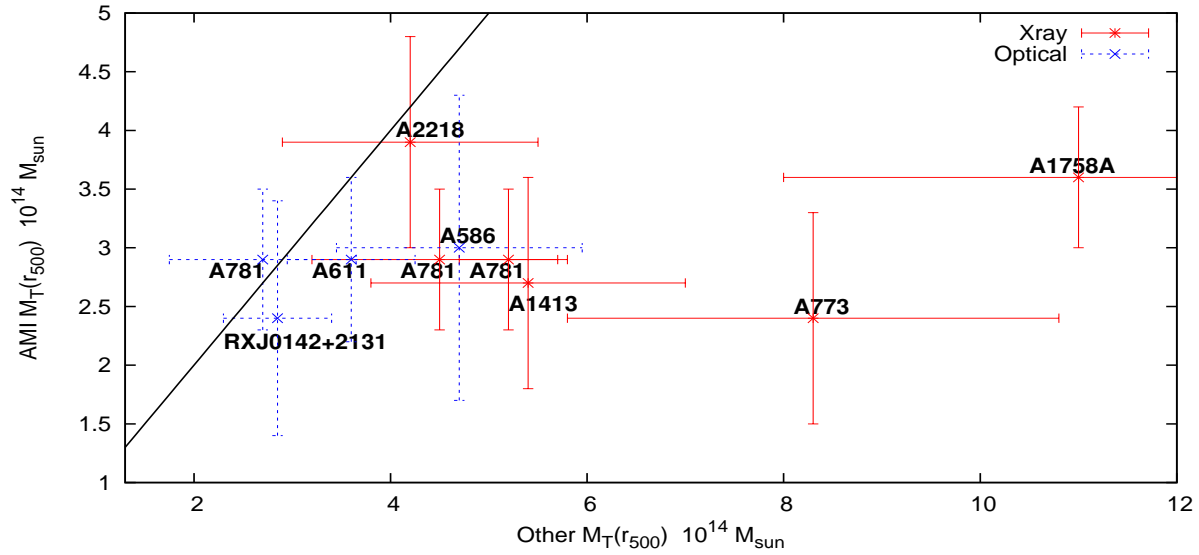


**Figure 32.** Comparison of AMI  $M_T(r_{500})$  measurements with others. Methods used for estimating  $M_T(r_{500})$  are given in the legend. The line of gradient one has been included to aid the comparison. The references are as follows: Abell 586 (Okabe et al. 2010); Abell 611 (Okabe et al. 2010); Abell 773 (Zhang et al. 2010); Abell 781 (Sehgal et al. 2008 and Zhang et al. 2010); Abell 1413 (Zhang et al. 2010), Abell 1758A (Zhang et al. 2010), Abell 2218 (Zhang et al. 2010) and RXJ0142+2131 (Okabe et al. 2010). AMI values are given in Tab. 6. These were the  $M(r_{500})$  from X-ray and weak lensing data that we found in the literature.

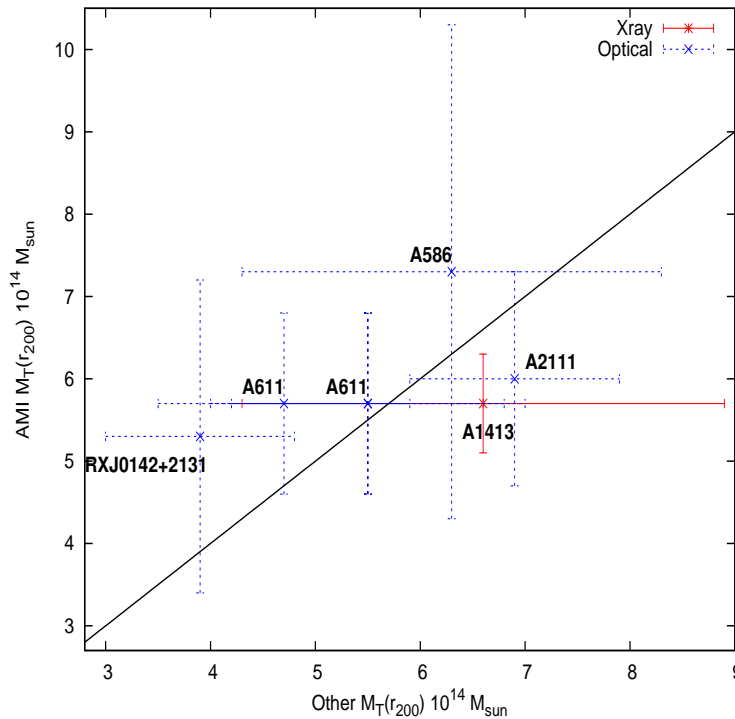


**Figure 33.** Comparison of AMI  $M_T(r_{200})$  measurements with others. Methods used for estimating  $M_T(r_{500})$  are given in the legend. Mass is given in units of  $\times 10^{14} M_\odot$ . The line of gradient one has been included to aid comparison. The references are as follows: Abell 586 (Okabe et al. 2010); Abell 611 (Okabe et al. 2010, Romano et al. 2010 and AMI Consortium: Hurley-Walker et al. 2011); Abell 1413 (Hoshino et al. 2010); Abell 2111 (AMI Consortium: Hurley-Walker et al. 2011) and RXJ0142+2131 (Okabe et al. 2010). AMI values are given in Tab. 6.

**Table 15.** Comparison of cluster masses at  $r_{500}$  and  $r_{200}$  for a spherical and an elliptical model for the cluster geometry. Ratio refers to the ratio between spherical and elliptical  $M_T$ 

Cluster Name	$M_T(r_{200})/\times 10^{14}M_\odot$			$M_T(r_{500})/\times 10^{13}M_\odot$		
	Spherical	Elliptical	Ratio	Spherical	Elliptical	Ratio
A586	$7.3 \pm 3.0$	$7.5^{+3.0}_{-3.1}$	$0.97 \pm 0.59$	$3.0 \pm 1.3$	$3.1 \pm 1.4$	$0.97 \pm 0.65$
A611	$5.7 \pm 1.1$	$5.8 \pm 1.2$	$0.98 \pm 0.30$	$2.9 \pm 0.7$	$2.9 \pm 0.7$	$1.00 \pm 0.34$
A621	$6.8^{+2.4}_{-2.5}$	$7.2^{+2.3}_{-2.4}$	$0.94 \pm 0.53$	$2.0 \pm 1.3$	$2.2^{+1.3}_{-1.4}$	$0.91^{+0.97}_{-1.00}$
A773	$5.1 \pm 1.7$	$7.4 \pm 2.3$	$0.69 \pm 0.66$	$2.4 \pm 0.9$	$3.1^{+1.4}_{-1.3}$	$0.77^{+0.76}_{-0.73}$
A781	$5.9 \pm 1.1$	$7.2 \pm 1.8$	$0.82 \pm 0.38$	$2.9 \pm 0.6$	$3.2 \pm 1.0$	$0.91 \pm 0.41$
A990	$2.9^{+0.6}_{-0.1}$	$2.9 \pm 0.6$	$1.00^{+0.29}_{-0.21}$	$1.6 \pm 0.3$	$1.6 \pm 0.3$	$1.00 \pm 0.27$
A1413	$5.7 \pm 1.4$	$5.8 \pm 1.5$	$0.98 \pm 0.36$	$2.7 \pm 0.9$	$2.8 \pm 0.8$	$0.96 \pm 0.46$
A1423	$3.1 \pm 1.1$	$4.3 \pm 1.8$	$0.72 \pm 0.76$	$1.6 \pm 0.6$	$2.0 \pm 0.9$	$0.80 \pm 0.73$
A1758a	$5.9^{+1.0}_{-1.1}$	$6.2 \pm 1.2$	$0.95^{+0.27}_{-0.28}$	$3.6 \pm 0.6$	$3.7 \pm 0.7$	$0.97 \pm 0.26$
A1758b	$6.3 \pm 2.7$	$5.8 \pm 2.5$	$1.09 \pm 0.56$	$3.1 \pm 1.4$	$2.8 \pm 1.2$	$1.11 \pm 0.56$
A2009	$6.6 \pm 2.1$	$5.7^{+2.6}_{-2.9}$	$1.16^{+0.48}_{-0.52}$	$2.9^{+0.3}_{-0.9}$	$2.0^{+1.2}_{-1.4}$	$1.45^{+0.42}_{-0.53}$
A2111	$6.0 \pm 1.3$	$6.0 \pm 1.4$	$1.00 \pm 0.32$	$2.6 \pm 0.7$	$2.7 \pm 0.9$	$0.96 \pm 0.44$
A2146	$7.1 \pm 1.0$	$7.5 \pm 1.5$	$0.95 \pm 0.26$	$3.9 \pm 0.7$	$3.8 \pm 0.8$	$1.03 \pm 0.27$
A2218	$8.7 \pm 1.3$	$9.0^{+1.6}_{-1.5}$	$0.97^{+0.24}_{-0.23}$	$3.9 \pm 0.9$	$4.0^{+1.0}_{-0.9}$	$0.97^{+0.35}_{-0.33}$
RXJ0142+2131	$5.3^{+1.6}_{-1.7}$	$5.4^{+1.8}_{-1.9}$	$0.98^{+0.46}_{-0.49}$	$2.4 \pm 1.0$	$2.5 \pm 1.0$	$0.96 \pm 0.6$
RXJ1720+2638	$2.9 \pm 0.6$	$3.6 \pm 0.7$	$0.81 \pm 0.35$	$1.7 \pm 0.3$	$2.1 \pm 0.4$	$0.81 \pm 0.32$

2000). We acknowledge the use of NASA's SkyView facility (<http://skyview.gsfc.nasa.gov>) located at NASA Goddard Space Flight Center.

## REFERENCES

- Allen S. W., Fabian A. C., 1998, MNRAS, 297, L63  
 Allen S. W., 2000, MNRAS, 315, 269  
 Allen S. W., Evrard A. E., Mantz A. B., 2011, ARA&A, 49, 409  
 Allison J. R., Taylor A. C., Jones M. E., Rawlings S., Kay S. T., 2011, MNRAS, 410, 341  
 AMI Consortium, et al., 2011, MNRAS, 415, 2708  
 AMI Consortium, et al., 2011, MNRAS, 415, 2699  
 AMI Consortium, et al., 2012, MNRAS, 419, 2921  
 AMI Consortium: Olamaie M. et al., 2012, MNRAS, 421, 1136  
 AMI Consortium: Rodríguez-González C et al., 2011, MNRAS, 414, 3751  
 AMI Consortium: Shimwell. T. W., et al., 2010, arXiv:1012.4441  
 AMI Consortium: Zwart J. T. L. et al., 2008, MNRAS, 391, 1545  
 AMI Consortium: Zwart J. T. L., et al., 2011, MNRAS, 418, 2754  
 Arnaud M., Pratt G. W., Piffaretti R., Böhringer H., Croston J. H., Pointecouteau E., 2010, A&A, 517, A92  
 Baars J., Davies R., Jorgensen I., Bergmann M., Crampton D., AJ, 130, 445  
 Barrena R., Boschin W., Girardi M., Spolaor M., 2007, A&A, 467, 37  
 Bauer, F. E., et al., 2005, MNRAS, 359, 1481  
 Bautz M. W., et al., 2009, PASJ, 61, 1117  
 Birkinshaw M., 1999, Physics Reports, 310, 97  
 Birkinshaw M., Gull S. F. & Northover K., 1981, MNRAS, 197, 571  
 Birkinshaw M., Gull S. F., 1984, MNRAS, 206, 359  
 Birkinshaw M., Hughes J. P., 1994, ApJ, 420, 33  
 Böhringer H., Schuecker P., Guzzo L. et al., 2004, A&A, 469, 363  
 Bonamente M., et al., 2005, ApJ, 614, 56-63  
 Bonamente M., Joy M. K., LaRoque S. J., Carlstrom J. E., Reese E. D., Dawson K. S., 2006, ApJ, 647, 25  
 Bonamente M., et al., 2012, NJPh, 14, 025010  
 Browne I. W. A., Wilkinson P. N., Patnaik A. R., Wrobel J. M., 1998, MNRAS, 293, 257  
 Browne I. W., Mao S., Wilkinson P. N., Kus A. J., Marecki A., Birkinshaw M., 2000, SPIE, 4015, 299  
 Buote D. A., 2001, ApJ, 553, L15  
 Carlstrom J. E., Joy M., Grego L., 1996, ApJ, 456, 75-78  
 Carlstrom J. E., Holder G. P., & Reese E. D. 2002, ARA&A, 40, 643  
 Carlstrom J. E., et al., 2011, PASP, 123, 568  
 Cavagnolo K. W., Donahue M., Voit G. M. et al., 2009, ApJS, 182, 12  
 Cavaliere A. & Fusco-Fermiano R., 1978, A & A, 70, 677  
 Corless V. L., King L. J., Clowe D., 2009, MNRAS, 393, 1235  
 Cypriano E. S., Sodr e Jr., Kneib L. et al, 2005, ApJ, 630, 38-49  
 Donnarumma A., et al., 2010, arXiv:1002.1625  
 David L. P., Kempner J., 2004, ApJ, 613, 831  
 Ebeling H., Edge A. C., Bohringer H. et al., 1998, MNRAS, 301, 881  
 Ebeling H., Edge A. C., Allen S. W. et al., 2000, MNRAS, 318, 333  
 Eke V. R., Cole S., Frenk C. S., 1996, MNRAS, 282, 263  
 Evrard A. E., 1997, MNRAS, 292, 289  
 Fabjan D., Borgani S., Rasia E., Bonafede A., Dolag K., Murante G., Tornatore L., 2011, MNRAS, 416, 801  
 Feroz F., Hobson M. P., 2008, MNRAS, 384, 449  
 Feroz F., Hobson M. P., Bridges M., 2009, MNRAS, 398, 1601  
 Feroz F., Hobson M. P., Zwart T. L. et al., 2009, MNRAS, 398, 2049  
 George M. R., Fabian A. C., Sanders J. S., Young A. J., Russell H. R., 2009, MNRAS, 395, 657  
 Giovannini G., Tordi M., Feretti L., 1999, NewA, 4, 141  
 Girardi M., Mezzetti M., 2001, ApJ, 548, 79  
 Govoni F., Feretti L., Giovannini G., Böhringer H., Reiprich T. H., Murgia M., 2001, A&A, 376, 803  
 Govoni F., Markevitch M., Vikhlinin A., VanSpeybroeck L., Feretti L., Giovannini G., 2004, ApJ, 605, 695  
 Govoni F., Murgia M., Markevitch M., Feretti L., Giovannini G., Taylor G. B., Carretti E., 2009, A&A, 499, 371  
 Grainge K., Jones M., Pooley G., Saunders R., Edge A., 1993, MNRAS, 265, L57  
 Grainge K.G.B., et al., 1996, MNRAS, 228, 17  
 Grainger W.F., et al., 2002, MNRAS, 337, 1207  
 Haines C. P., Smith G. P., Egami E., Okabe N., Takada M., Ellis R.

- S., Moran S. M., Umetsu K., 2009, MNRAS, 396, 1297
- Hanisch R. J., 1980, AJ, 85, 1565
- Henriksen M., Wnag Q. D. & Ulmer M.P., 1998, AJ, 116, 1529
- Herbig T., Lawrence C. R., Readhead A. C. S., Gulkis S., 1995, ApJ, 449, L5
- Hincks A. D., et al., 2010, ApJS, 191, 423
- Hoshino A., et al., 2010, PASJ, 62, 371
- Hudson D. S., Mittal R., Reiprich T. H., Nulsen P. E. J., Andernach H., Sarazin C. L., 2010, A&A, 513, A37
- Jones M. E., Saunders R., Alexander P. et al., 1993, Nature, 365, 320
- Jones M. E. et al., 2005, MNRAS, 357, 518
- Joy M., et al., 2001, ApJ, 551, L1
- Kaiser N., 1986, MNRAS, 222, 323
- Katayama H., Hayashida K., Takahara F., Fujita Y., 2003, ApJ, 585, 687
- Kawaharada M., et al., 2010, ApJ, 714, 423
- Klein U., Rephaeli Y., Schlickeiser R. et al., 1991, A & A, 244, 43
- Kornigut P., Dicker S., Reese E. D., Mason B. S., Devlin M. J., Mroczkowski T., Sarazin C. L., Sun M., 2011, AAS, 43, #227.05
- Kornigut P. M., et al., 2011, ApJ, 734, 10
- Kotov O., Vikhlinin A., 2005, ApJ, 633, 781
- Krause E., Pierpaoli E., Dolag K., Borgani S., 2012, MNRAS, 419, 1766
- Kravtsov A. V., Vikhlinin A., Nagai D., 2006, ApJ, 650, 128
- Lancaster K., Birkinshaw M., Gawroński, Browne I, Feiler R. et al., 2007, MNRAS, 378, 673
- Lancaster K., et al., 2011, MNRAS, 418, 1441
- LaRoque S. A., Bonamente M., Carlstrom J. E., Marshall K. J. et al., 2006, ApJ, 652, 917-936
- Larson D., Dunkley J., Hinshaw G., Komatsu E. et al., 2011, ApJS, 192, 16
- Lo K., Martin R., Chiueh T., 2001, aprs.conf, 235
- Partridge R. B., Perley R. A., Mandolezi N., 1987, ApJ, 317, 112
- Pratt G. W., Böhringer H. & Finoguenov A, 2004, A & A, 429, 791-806
- Machacek M. E., Bautz M. W., Canizares C. et al., 2002, ApJ, 567, 188
- Mahdavi A., Hoekstra H., Babul A., Henry J. P., 2008, MNRAS, 384, 1567
- Mandelbaum R., Seljak U., 2007, JCAP, 6, 24
- Markevitch M., 1997, ApJ, 483, L17
- Markevitch M., Gonzalez A. H., David L., Vikhlinin A., Murray S., Forman W., Jones C. & Tucker W., 2002, ApJ, 567, L27
- Marriage T. A., et al., 2011, ApJ, 737, 61
- Marrone D. P., et al., 2009, ApJ, 701, L114
- Marrone D. P., et al., 2011, arXiv, arXiv:1107.5115
- Marshall P. J., Hobson M. P. & Slozar A., 2003, MNRAS, 346, 489
- Massardi M., Ekers R. D., Ellis S. C., Maughan B., 2010, ApJ, 718, L23
- Maughan B. J., Jones C., Forman W., Van Speybroeck L., 2008, ApJS
- Mazzotta P., Markevitch M., Vikhlinin A., Forman W. R., David L. P., van Speybroeck L., 2001, ApJ, 555, 205
- Mazzotta P., Rasia E., Moscardini L., Tormen G., 2004, MNRAS, 354, 10
- Mazzotta P., Giacintucci S., 2008, ApJ, 675, L9
- McGlynn T. A., Fabian A. C., 1984, MNRAS, 208, 709
- Menanteau F., et al., 2011, arXiv, arXiv:1109.0953
- Meneghetti M., Rasia E., Merten J., Bellagamba F., Ettori S., Mazzotta P., Dolag K., Marri S., 2010, A&A, 514, A93
- Miller C. J., et al., 2005, AJ, 130, 968
- Molnar S. M., Hearn N. C., Stadel J. G., 2012, arXiv, arXiv:1201.1533
- Morandi, A., Ettori, S., Moscardini, L. 2007, MNRAS, 379, 518
- Morandi, A., Ettori, S., 2007, MNRAS, 708
- Motl P. M., Hallman E. J., Burns J. O., Norman M. L., 2005, ApJ, 623, L63
- Mroczkowski T., et al., 2009, ApJ, 694, 1034
- Mroczkowski T., et al., 2011, MmSAI, 82, 485
- Mroczkowski T., 2011, ApJ, 728, L35
- Muchovej S., et al., 2011, ApJ, 732, 28
- Nagai D., Vikhlin A & Kravtsov A., 2007, ApJ, 655, 98
- Nagai D., Lau E. T., 2011, ApJ, 731, L10
- Navarro J. F., Frenk C. S., White S. D. M., 1996, ApJ, 462, 563
- Nelson K., Rudd D. H., Shaw L., Nagai D., 2011, arXiv, arXiv:1112.3659
- Okabe N., Umetsu K., 2008, PASJ, 60, 345
- Okabe N., Takada M., Umetsu K., Futamase T., Smith G. P., 2010, PASJ, 62, 811
- Olamaie M., Hobson M. P., Grainge K. J. B., 2011, arXiv, arXiv:1109.2834
- Owers M. S., Nulsen P. E. J., Couch W. J., 2011, ApJ, 741, 122
- Patnaik A. R., Browne I. W. A., Wilkinson P. N., Wrobel J. M., 1992, MNRAS, 254, 655
- Planck Collaboration, et al., 2011, A&A, 536, A8
- Planck Collaboration, et al., 2011, A&A, 536, A10
- Planck and AMI collaborations et al., 2012, in preparation
- Poole G. B., Babul A., McCarthy I. G., Fardal M. A., Bildfell C. J., Quinn T., Mahdavi A., 2007, MNRAS, 380, 437
- Pratt G.W., Arnaud M., 2005, A&A, 429, 791-806
- Lau E. T., Kravtsov A. V., Nagai D., 2009, ApJ, 705, 1129
- Rasia E., Tormen G., Moscardini L., 2004, MNRAS, 351, 237
- Rasia E., et al., 2012, arXiv, arXiv:1201.1569
- Richard J., et al., 2010, MNRAS, 404, 325
- Ricker P. M., Sarazin C. L., 2001, ApJ, 561, 621
- Rines K., Geller M. J., Diaferio A., 2010, The Astrophysical Journal Letters, 715, 180
- Rizza E., Burns J. O., Ledlow M. J. et al., 1998, MNRAS, 301, 328
- Romano A., et al., 2010, A&A, 514, A88
- Rossetti M., Eckert D., Cavalleri B. M., Molendi S., Gastaldello F., Ghizzardi S., 2011, A&A, 532, A123
- Rozo E., Wu H.-Y., Schmidt F., 2011, ApJ, 735, 118
- Rudnick L., Lemmerman J. A., 2009, ApJ, 697, 1341
- Russell, H.R. and Sanders, J. S. and Fabian, A. C. and Baum, S. A. and Donahue, M. and Edge, A. C. and McNamara, B. R. and O’Dea, C. P., 2010, MNRAS
- Sanderson, A. J. R., Edge, A. C., Smith, G. P., 2009, MNRAS, 398, 1698
- Saunders R., et al., 2003, MNRAS, 341, 937
- Schmidt R. W., Allen S. W., 2007, MNRAS, 379, 209
- Sehgal N., Hughes J. P., Wittman D., Margoniner V., Tyson J. A., Gee P., dell’Antonio I., 2008, ApJ, 673, 163
- Sifon C., et al., 2012, arXiv, arXiv:1201.0991
- Sijacki D., Springel V., Di Matteo T., Hernquist L., 2007, MNRAS, 380, 877
- Squires G., Kaiser N., Babul A, Fahlman G, Woods D, Neumann D. M., Böhringer H., 1996, ApJ, 461, 572
- Smith G. P., Edge A. C., Eke V. R., Nichol R. C., Smail I., Kneib J. P., 2003, ApJ, 590, L79
- Smith G. P., Kneib J. P., Smail I, Mazzotta P., Ebeling H., 2005, MNRAS, 359, 417
- Snowden, S. L., Mushotzky, R. F., Kuntz, K. D., Davis, D. S., 2008, A&A, 478, 615



- Sunyaev R. A., & Zel'dovich Y. B., 1970, *Comments on Astrophysics and Space*, 2, 66
- Takizawa M., Nagino R., Matsushita K., 2010, arXiv, arXiv:1004.3322
- Tauber J. A., et al., 2010, *A&A*, 520, A1
- Tsuboi M., Miyazaki A., Kasuga T. et al., 2004, *PASJ*, 56, 711
- Venture, T., et al., 2008, *A&A* 484, 327-340
- Venturi et al., 2008, *A&A*, 484, 327
- Vikhlinin A., et al., 2005, *ApJ*, 628, 655-672
- Voit G. M., 2005, *RvMP*, 77, 207
- Wang Q. D., Ulmer M. P. & L'Avary R. J., 1997, *MNRAS*, 288, 702
- White S. D. M., Navarro J. F., Evrard A. E., Frenk C. S., 1993, *Natur*, 366, 429
- White D. A., 2000, *MNRAS*, 312, 663
- Wilkinson P. N., Browne I. W. A., Patnaik A. R., Wrobel J. M., Sorathia B., 1998, *MNRAS*, 300, 790
- Williamson R., et al., 2011, *ApJ*, 738, 139
- Wu J.-H. P., et al., 2008, *MPLA*, 23, 1675
- Vikhlinin A., Kravtsov A., Forman W., Jones C., Markevitch M., Murray S. S., Van Speybroeck L., 2006, *ApJ*, 640, 691
- Voit G. M., Kay S. T., Bryan G. L., 2005, *MNRAS*, 364, 909
- Zhang Y. Y., Okabe N., Finoguenov A. et al., 2008, *A & A*, 482, 451
- Zhang Y. Y., Okabe N., Finoguenov A. et al., 2010, *ApJ*, 711, 1033-1043